UNIVERISTY OF CALIFORNIA
RIVERSIDE

Time-Domain Terahertz Spectroscopy of Water

A Dissertation submitted in partial satisfaction
of the requirements for the degree of

Doctor of Philosophy

in

Physics

by

Jojit Camama Torcedo

March 2010

Dissertation Committee:
Professor Harry Tom, Chairperson
Professor Ward Beyermann
Professor Umar Mohideen

The Dissertation of Jojit Camama Torcedo is approved:

_____

_____

_____

Committee Chairperson

University of California, Riverside

ACKNOWLEDGEMENTS

I would like to thank Professor Tom for affording me the opportunity to work on this important topic. I am also grateful for the advice and support of my committee members, Professor Beyermann and Professor Mohideen.

My sincerest thanks to Jason McNary for his invaluable knowledge, wisdom, and advice that got me through all the struggles I encountered in this work. Not only do I consider him a great mentor, but also a great friend. I would also like to thank Paul Glancy, for his help in the terahertz lab, and Koji Yokoyama for his MD simulation work on water presented in this dissertation. Thanks to Peng Wan, and Xiao Jing Tan for their help and support as well.

I have enjoyed my graduate school experience due in large part to my great group of friends: Tim Hester, Peter Hunana, Ken James, and Kaoru Kamiya. I thank them for all their support.

I express my deep gratitude to my wonderful family. I thank my sister, Abigail who has always believed in me and encouraged me to do my best. Of course, I thank my parents, Alfredo and Neriza Torcedo, for their unending love and support. They have taught me that the virtues of honesty, hard work, and determination can truly pay off.

DEDICATION

To my wife, Cherryl. She has been my inspiration through this arduous journey.

ABSTRACT OF THE DISSERTATION

Time Domain Terahertz Spectroscopy of Water

by

Jojit Camama Torcedo

Doctor of Philosophy, Graduate Program in Physics
University of California, Riverside, March 2010
Dr. Harry Tom, Chairperson

The dielectric spectrum of D_2O between 15 GHz and 2 THz was measured using Terahertz Time-Domain Spectroscopy. The motivation of this work is to gain an understanding of liquid water dynamics on a molecular level. To achieve this, we use a correction to the dielectric response of polar molecules known as the reduced polarization. This correction allows us to relate the macroscopic quantity of the permittivity to the microscopic correlation function in a manner appropriate for polar liquids. Similar to previous studies on H_2O, evidence is shown of correlated and anti-correlated dipole-dipole interactions in liquid D_2O. More interestingly, the spectra also reveal dynamics that could be intimately related to the density anomaly of water.

TABLE OF CONTENTS

LIST OF TABLES

LIST OF FIGURES

Chapter 1 Water and its Dielectric Response

1.1 Properties and Structure of Liquid Water

Water is the only inorganic substance to naturally occur in all three states: solid, liquid, and gas. Not surprisingly, there is a near infinite amount of science about the most ubiquitous substance on earth, and because of this, some of the most basic units of measurement – temperature, mass, and volume – are calibrated to water. These extensive investigations of water have revealed how strange it is in comparison to other liquids, and as many as forty so-called "anomalous" properties of water have been observed [1]. Some of the most notable are: an unusually high melting and boiling point (273.15 K and 373.15 K), a maximum density at 3.984 ^{o}C, and a high static dielectric constant (80.1 at 20 ^{o}C). More recently, it was observed that the vibrational relaxation of the OH-stretching mode was found to slow down with increasing temperature [2].

It is somewhat remarkable that for the many peculiar properties water possesses, they are just the consequences of two things: high polarizability and hydrogen bonding. For instance, water's relatively large static dielectric constant is a result of its high polarizability, which in turn is due to a large dipole moment. In the vapor phase, the static dipole moment of a single water molecule has been measured to be 1.84 Debyes, which is a similar result to experiments with solutions of dilute H_2O in benzene [3]. The dipole moment increases and lies between 2.4 and 2.6 D when in the liquid phase [4] and some report that it may even be as high as 2.9 D. However, when attempting to describe

the “structure” of liquid water, both the competing effects of the hydrogen bond and the high polarizability must be taken into account. Although a myriad of models have been proposed to describe the structure of water, they generally can be divided into three categories: uniform models, interstitial models, and mixture models.

The cornerstone notion of the uniform model is that hydrogen bonds are able to bend, but not brake. In this model, when ice melts, the positions of neighboring molecules deform, and the level of bond bending, position, and orientation depend on temperature and pressure [5]. X-ray measurements have shown good agreement with this model as the data reveals an ice-like structure, though not as defined, for liquid water. In addition, the radial distribution functions from these measurements give the average oxygen-oxygen distance for nearest neighbors to be around 2.88 Å, the second nearest at 4.5 Å, and third nearest located 6.75 Å away [6]. On the other hand, measurements from Raman and IR spectra show a great deal of evidence for the breaking of hydrogen bonds in liquid water [5, 7].

Interstitial, or “water hydrate”, models take on the idea that when ice begins to melt, a small number of the water molecules are broken off from the structure to freely move about in the interstitial spaces between the water “cage”. From the now vacant locations on the lattice, random irregularities arise, and cause complete disorder on the order of 10 Å. These types of models, however, rely on a large degree of cooperation in the hydrogen bond network which has yet to be observed by experiment [5]. The upshot is that they, like the uniform model, agree with radial distribution function measurements.

The mixture model, as the name suggests, is a mixture of water molecules that exhibit ice-like or fluid-like qualities, or more precisely, hydrogen bonded or unbonded. Bonded molecules only remain so for a finite amount of time and subsequently, an unbound molecule can then become bonded. This is similar to the interstitial model, except for the irregularities that arise from vacant lattice locations. Since the inception of this idea, the model has evolved to allow for as many as five different species of water, running from unbound and singly bonded types all the way up to completely bound molecules with 4 neighbors. For a complete description, these models must make some statement about the cluster size and the relative number of molecules of different bondedness [5].

The water pentamer is the most energetically favorable configuration for a single water molecule. Depicted in figure 1.1, a central water molecule is hydrogen bonded to four nearest neighbors. As a side note, the tetrahedral angle shown in figure 1.1 of 109.47^{o} is different than the 104.5^{o} of liquid water [3]. However, recent x-ray spectroscopy and x-ray Raman scattering experiments that have interrogated the first coordination shell of water have suggested that most water molecules are in a two hydrogen bonded configuration with a strong donor bond and one strong acceptor bond. These measurements have estimated that around 80% of water assume a doubly bonded structure while only 20% are tetrahedrally coordinated, thus hinting towards a mixture model type of structure. Additionally, planar rings and long chains are not excluded from forming [7].

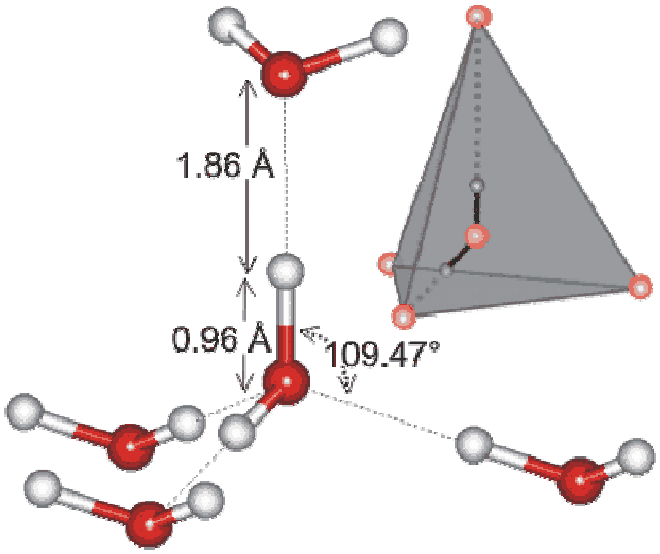

Figure 1.1 The water pentamer. A central water molecule is hydrogen bonded to 4 nearest neighbors [8].

To achieve an understanding of water, an important second system to study is heavy water, also known as D_2O. The difference molecularly to H_2O is the substitution of the hydrogen atoms with deuterium. This addition of the two neutrons results in a mass increase of 11% and has somewhat of a profound effect in that heavy water is generally regarded as being more structured than water under similar conditions. Although the potential energy of interaction with other water molecules or solutes is the same as light water, the amplitudes for librational oscillations are smaller, thus resulting in less kinetic energy for D_2O [9]. Due to this, the deuterium bond is considered to be stronger than the hydrogen bond, giving D_2O its higher melting and boiling points than H_2O [10].

1.2 The Dielectric Response of Water

1.2.1 General Dielectric Theory

Debye's pioneering theory for the dielectric response of polar molecules in 1929 has undergone much refinement over the years. Despite these numerous efforts, an accurate understanding of the dielectric response of water on a molecular level still proves to be a challenge in spectroscopy. The major motivation of this work is to address this problem by correctly relating the macroscopic quantity of the dielectric permittivity to the microscopic correlation function of dipolar water molecules.

One can derive the relationship between the dielectric response and the autocorrelation function by starting with a polarizable medium with macroscopic moment **M** and polarization **P**. The autocorrelation function for **M** at zero frequency $\mathbf{M}^0$ is defined as:

$$\phi_{sph}(t) = \frac{\langle M^0(0) \bullet M^0(t) \rangle}{\langle M^0 \bullet M^0 \rangle} \tag{1.1}$$

The dielectric permittivity has been shown to be related to the Laplace transform of the time derivative of the autocorrelation function:

$$\frac{\hat{\varepsilon}(\omega) - \varepsilon_\infty}{\hat{\varepsilon}(\omega) + 2} = \frac{\varepsilon_0 - \varepsilon_\infty}{\varepsilon_0 + 2} \mathscr{L}\left[-\dot{\phi}_{sph}\right] \tag{1.2}$$

For a gas at normal pressure, the molecular orientations are independent of each other and the autocorrelation function becomes:

$$\phi_{sph}(t) = \frac{1}{\mu^2} \langle \mu(0) \bullet \mu(t) \rangle \tag{1.3}$$

This expression is the dipole correlation function, and is referred to as *C(t)*. For a dilute gas, the ratio $(\varepsilon_0 + 2)/(\hat{\varepsilon}(\omega) + 2) \approx 1$ and equation 1.2 becomes:

$$\varepsilon(\omega) - \varepsilon_\infty = (\varepsilon_0 - \varepsilon_\infty)\mathcal{L}\left[-\dot{C}(t)\right] \tag{1.4}$$

This is the solution to the step response function for orientational polarization [11]. However, for polar liquids, this model is inaccurate since it includes long-range dipole-dipole interactions. These interactions must be eliminated to obtain a relationship between the dielectric constant and the molecular relaxation.

The microscopic correlation function is defined as

$$\gamma(t) = \frac{\left\langle \mu_i(0) \bullet \sum_{j=1}^{N} \mu_j(t) \right\rangle}{\left\langle \mu_i(0) \bullet \sum_{j=1}^{N} \mu_j(0) \right\rangle} \tag{1.5}$$

To only include short-range interactions, the summation is over permanent dipole moments in a small sphere around a central dipole, μ_i. Also known as the Onsager approximation, the size of the sphere is approximately the size of the dipole [12]. Calculations by Fatuzzo and Mason, then furthered by D.D. Klug use this approximation to determine a relation between the dielectric constant to the microscopic correlation function to be

$$\frac{\left(\hat{\varepsilon}(\omega) - \varepsilon_\infty\right)\left(2\hat{\varepsilon}(\omega) + \varepsilon_\infty\right)\varepsilon_0}{\left(\varepsilon_0 - \varepsilon_\infty\right)\left(2\varepsilon_0 + \varepsilon_\infty\right)\hat{\varepsilon}(\omega)} = \mathcal{L}_{i\omega}\left[-\dot{\gamma}(t)\right] = 1 - i\omega\mathcal{L}_{i\omega}\left[\gamma(t)\right] \tag{1.6}$$

The Laplace transform of the microscopic correlation function is directly related to the frequency-dependent complex dielectric permittivity. The left side of this equation is known as the reduced polarization.

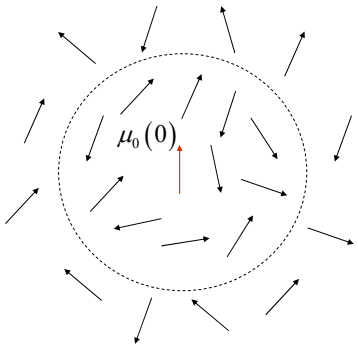

Figure 1.2 Depiction of the Onsager sphere. Only dipoles that are within the dotted sphere are included in the summation of the microscopic correlation function of equation 1.5.

Several approximations can be made to this equation. In the limit where $\varepsilon_0 / \varepsilon_\infty \gg 1$ or where $(\varepsilon_0 / \varepsilon_\infty - 1) \ll 1$, the can be approximated as

$$\frac{(2\hat{\varepsilon}(\omega) + \varepsilon_\infty)\varepsilon_0}{(2\varepsilon_0 + \varepsilon_\infty)\hat{\varepsilon}(\omega)} \approx 1 \tag{1.7}$$

and thusly, equation 1.6 reduces to

$$\hat{\varepsilon}(\omega) = \varepsilon_\infty + (\varepsilon_0 - \varepsilon_\infty)\mathscr{L}[-\dot{\gamma}(t)] \tag{1.8}$$

If we then approximate the Onsager sphere to only encompass the central dipole, the microscopic correlation function, $\gamma(t)$, of equation 1.5 reduces to the dipole correlation function *C(t)* from equation 1.3. This results in equation 1.8 being identical to equation 1.4, the step response function for the orientational polarization and has become the standard equation for modeling water in the terahertz range. However, it has been shown

that in the high frequency regime where $\varepsilon_0 / \varepsilon_\infty \gg 1$, this approximation fails [11] . It is also unrealistic to only assume that only the central dipole contributes to the microscopic correlation function, and therefore for a more accurate physical representation of water, spectroscopic data must be fit to the complete reduced polarization.

1.2.2 Debye Relaxation

In 1929, Debye had one of the earliest attempts at relating the complex permittivity to the microscopic correlation function. Despite the age of his formalism, it is still widely accepted and used in the spectroscopic community. He proposed that the polarization of a medium within an alternating external electric field relaxes in a characteristic time when the field is turned off [13]. This is expressed as

$$P(t) = P_0 e^{-t/\tau_D} \tag{1.9}$$

From an exponential decay of polarization, one can show the expression for the complex dielectric permittivity to be

$$\hat{\varepsilon}(\omega) = \varepsilon_\infty + \frac{\varepsilon_0 - \varepsilon_\infty}{1 + i\omega\tau_D} \tag{1.10}$$

However, subsequent experiments have often shown evidence of two or more relaxation processes [14-18, 19], and the above equation can be generalized to

$$\frac{\hat{\varepsilon}(\omega) - \varepsilon_\infty}{\varepsilon_0 - \varepsilon_\infty} = \sum_i \frac{f_i}{1 + i\omega\tau_i} \tag{1.11}$$

where $\sum_i f_i$. Shown in figure 1.4 are several relaxation times.

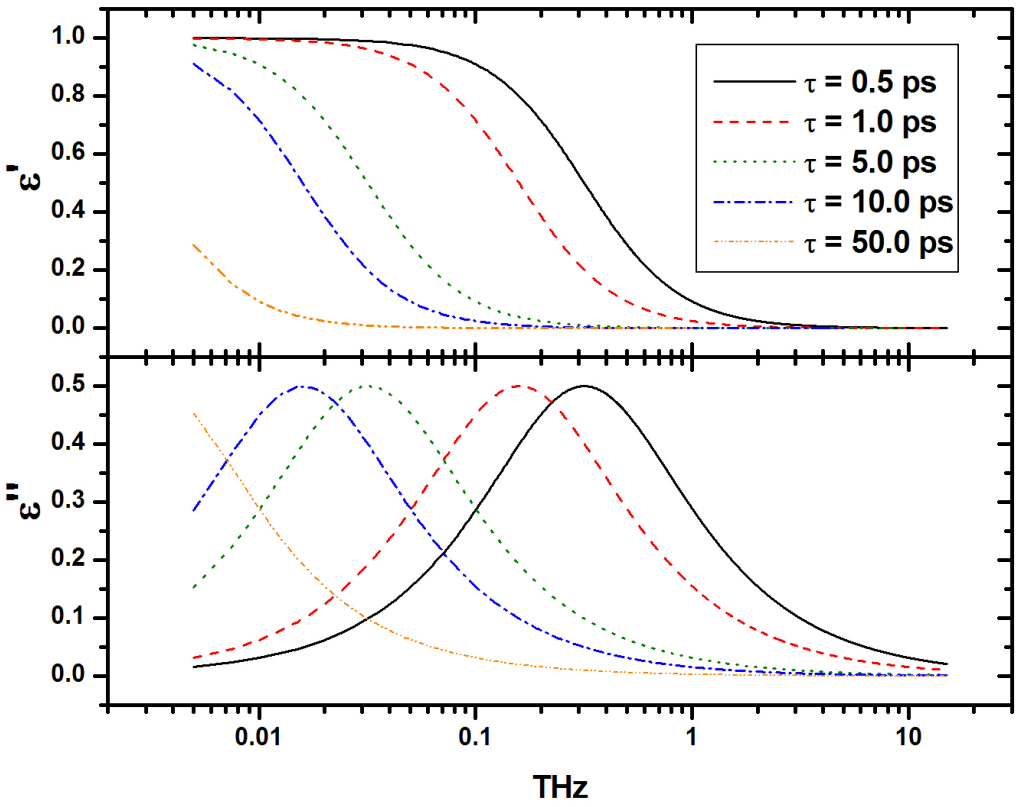

Figure 1.3 Simulated Debye relaxations for different decay times.

The measurements of multiple relaxation times have led to modifications of equation 1.10, namely the Havriliak-Negami relationship:

$$\hat{\varepsilon}(\omega) = \varepsilon_\infty + \frac{\varepsilon_0 - \varepsilon_\infty}{\left[1 + (i\omega\tau_D)^{1-\alpha}\right]^\beta} \tag{1.12}$$

where $0 \le \alpha, \beta \le 1$ [12]. This relation reduces to a single Debye relaxation for the case $\alpha = 0, \beta = 1$. When $\alpha > 0, \beta = 1$ it is known as the Cole-Cole equation and for $\alpha = 0, \beta < 1$ gives the Cole-Davidson equation [19]. Both are solutions to continuous distributions of relaxation times.

1.2.3 Lorentzians

The Debye and related equations give a good description of dynamics whose decay times are short compared to the driving frequency of the electric fields. However, at higher frequencies, resonant restoring forces can overcome the damping steric forces in the liquid. The equation of motion for this case is just one of a driven and damped harmonic oscillator:

$$\mu\left[\ddot{x}+\Gamma\dot{x}+\omega_0^2 x\right]=-e^*\mathbf{E}\left(x,t\right) \tag{1.13}$$

where Γ is the damping force, μ is the reduced mass, and e^* is the effective charge [20]. For an electric field proportional to $e^{-i\omega t}$, the time-varying dipole moment is then

$$\mathbf{p}\left(t\right)=-e^* x\left(t\right)=\frac{e^{*2}}{\mu}\frac{\mathbf{E}}{\left(\omega_o^2-\omega^2-i\omega\Gamma\right)} \tag{1.14}$$

This in turn leads to a resonant term in the macroscopic polarization expressed as

$$\mathbf{P}_{resonant}=N\mathbf{p}\left(t\right)=\frac{Ne^{*2}}{\mu}\frac{\mathbf{E}}{\left(\omega_o^2-\omega^2-i\omega\Gamma\right)} \tag{1.15}$$

with *N* being the number of dipoles per unit volume [21].

The displacement field **D** is expressed in Gaussian units as

$$\mathbf{D}=\hat{\varepsilon}\mathbf{E}=\mathbf{E}+4\pi\mathbf{P} \tag{1.16}$$

Where $\mathbf{P}=\mathbf{P}_{resonant}+\mathbf{P}_{background}$. The background term is due to the static polarization defined by the electric susceptibility tensor χ and is given as $\mathbf{P}_{background}=\chi\mathbf{E}$. Taking this into account, the full expression of the displacement field becomes

$$\mathbf{D} = \left(1 + 4\pi\chi + \frac{4\pi N e^{*2}}{\mu} \frac{1}{\left(\omega_o^2 - \omega^2 - i\omega\Gamma\right)}\right)\mathbf{E} \tag{1.17}$$

The complex permittivity is solved for and given as

$$\hat{\varepsilon}(\omega) = 1 + 4\pi\chi + \frac{4\pi N e^{*2}}{\mu} \frac{1}{\left(\omega_o^2 - \omega^2 + i\omega\Gamma\right)} \tag{1.18}$$

It is important to note the sign change in the term that contains the damping parameter Γ is due to the fact that the complex permittivity is defined as $\hat{\varepsilon} = \varepsilon' + i\varepsilon''$. Taking the high frequency limit of the permittivity yields

$$\hat{\varepsilon}(\infty) = 1 + 4\pi\chi = \varepsilon_\infty \tag{1.19}$$

while the static limit is

$$\hat{\varepsilon}(0) = \varepsilon_0 = 1 + 4\pi\chi + \frac{4\pi N e^{*2}}{\mu\omega_o^2} \tag{1.20}$$

Oscillator strength is the third term in equation 1.20

$$\varepsilon_0 - \varepsilon_\infty = \frac{4\pi N e^{*2}}{\mu\omega_o^2} \tag{1.21}$$

In the case of a liquid with a large ensemble of molecules and a distribution of discrete binding frequencies ω_i and damping constants Γ_i, the frequency dependent permittivity of equation 1.18 becomes

$$\hat{\varepsilon}(\omega) = \varepsilon_\infty + (\varepsilon_0 - \varepsilon_\infty)\sum_i \frac{\omega_i^2 f_i}{\left(\omega_i^2 - \omega^2 + i\omega\Gamma_i\right)} \tag{1.22}$$

where the discrete oscillator amplitudes f_i are such that $\sum_i f_i = 1$. Figure 1.4 shows simulated Lorentzian oscillators with different degrees of damping: underdamped,

critically damped, and overdamped. It is important to note that the peak of the Lorentzian in the imaginary part redshifts as the damping constant increases. It is important to note that the Debye relaxation is just a special case of a single oscillator in the low frequency regime of $\omega \ll \omega_i$. In this limit, the resonant polarization defined in equation 1.15 reduces to that of a Debye relaxation with characteristic time $\tau_D = \Gamma_i / \omega_i^2$ as seen in equation 1.9. For this special case, damping and restoring forces are large enough to neglect the inertial term $\ddot{x}$ in equation 1.13 [22].

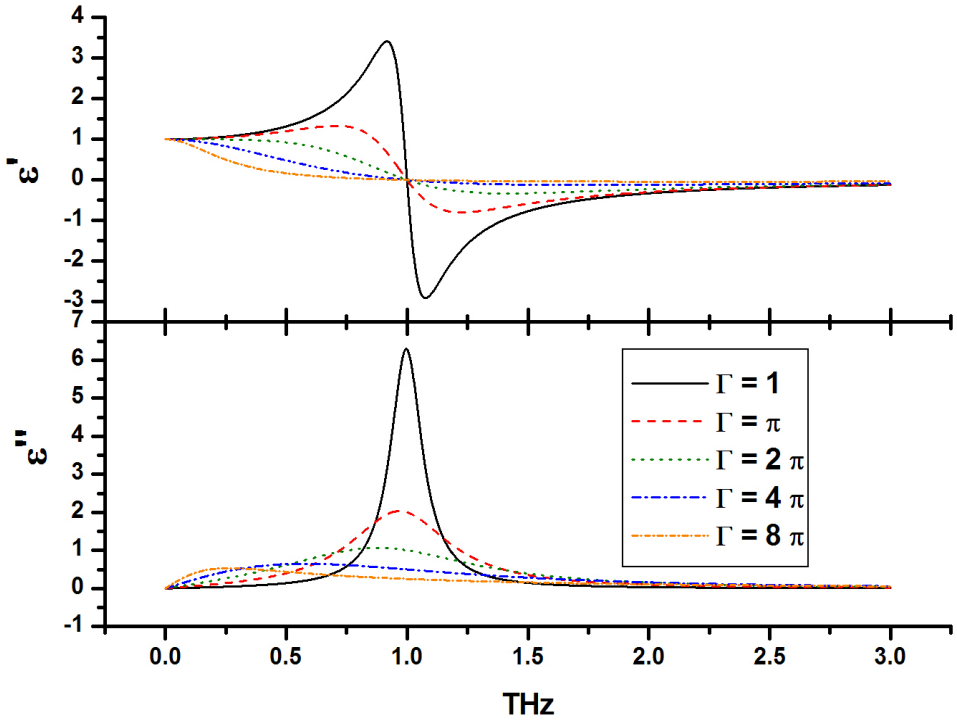

Figure 1.4 Simulated Lorentzians centered at 1 THz. The varying values of the damping term, Γ, have units of ps^{-1}. The last two are examples of critically and overdamped oscillators, respectively.

The dipole correlation function *C(t)* can be calculated for a Lorentzian oscillatory response to yield three solutions corresponding to underdamped, critically damped, and overdamped motions. The underdamped solution is given by

$$C(t) = \frac{\cos(\Omega t - \phi)}{\cos(\phi)} e^{-\frac{1}{2}\Gamma t} \tag{1.23}$$

where $\phi = \tan^{-1}\left(\frac{\Gamma}{2\Omega}\right)$ and $\Omega = \sqrt{\omega_o^2 - (\Gamma/2)^2}$. The exponential decay from equation 1.9 is the critically damped solution. The overdamped solution is a hyperbolic function that can be written as a difference of two exponential decays [11] and is expressed as

$$C(t) = \frac{\tau_1}{\tau_1 - \tau_2} e^{-t/\tau_1} - \frac{\tau_2}{\tau_1 - \tau_2} e^{-t/\tau_2} \tag{1.22}$$

and

$$\tau_{1,2} = \frac{\Gamma \pm \sqrt{\Gamma^2 - 4\omega_o^2}}{2\omega_o^2}, \tag{1.23}$$

where τ_1 corresponds to the longer time.

It is reasonable to expect to observe one or more oscillations or relaxations when measuring the dielectric response over a broad band of frequencies. For these types of measurements equations 1.12 and 1.22 can be combined to yield

$$\frac{\hat{\varepsilon}(\omega) - \varepsilon_\infty}{\varepsilon_0 - \varepsilon_\infty} = \sum_j \frac{f_j}{\left[1 + (i\omega\tau_j)^{1-\alpha_j}\right]^{\beta_j}} + \sum_k \frac{{\omega_k}^2 f_k}{{\omega_k}^2 - \omega^2 + i\omega\Gamma_k} \tag{1.24}$$

It has been stated earlier that the right side of this equation is not an accurate for water, as it is an approximation for strongly polar liquids. Therefore, it must be corrected with the reduced polarization given in equation 1.6:

$$\frac{\left(\hat{\varepsilon}(\omega)-\varepsilon_{\infty}\right)\left(2\hat{\varepsilon}(\omega)+\varepsilon_{\infty}\right)\varepsilon_{0}}{\left(\varepsilon_{0}-\varepsilon_{\infty}\right)\left(2\varepsilon_{0}+\varepsilon_{\infty}\right)\hat{\varepsilon}(\omega)}=\sum_{j}\frac{f_{j}}{\left[1+\left(i\omega\tau_{j}\right)^{1-\alpha_{j}}\right]^{\beta_{j}}}+\sum_{k}\frac{{\omega_{k}}^{2}f_{k}}{{\omega_{k}}^{2}-\omega^{2}+i\omega\Gamma_{k}}. \quad (1.25)$$

Chapter 2 THz Time Domain Spectroscopy

2.1 The THz Spectrum

Existing between the microwave and far infra-red frequency ranges, terahertz (THz) radiation has frequencies around 10^{12} hertz, as its name suggests. Spectroscopy is the study of the interaction between matter and light, and depending on the frequency range of light used, one can observe various physical phenomena. For instance, radiation from the visible spectrum induces electron orbital transitions while the infra-red spectrum is used to probe vibrational motions of compact molecules or the sub-structures of larger molecules. The energy of the THz frequencies can be employed to investigate intermolecular interactions and intramolecular oscillatory modes for larger molecules and polymer chains.

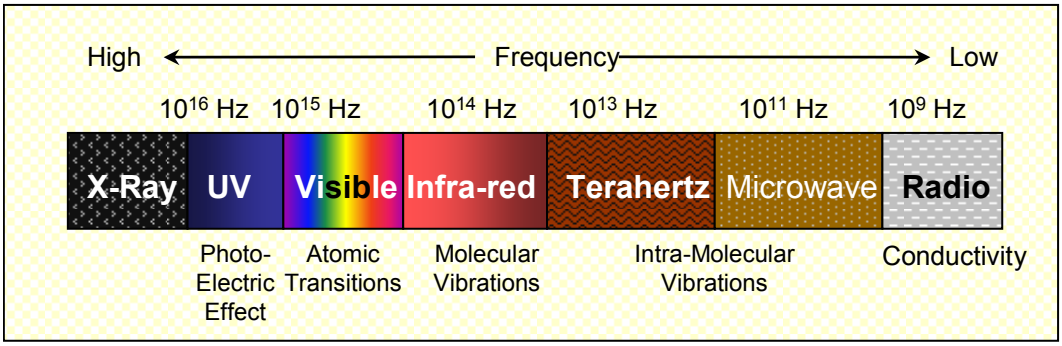

Figure 2.1 The electromagnetic spectrum and the phenomena associated with its frequency ranges.

Historically, measurements in the THz range have involved developing microwave cavities to generate higher THz frequencies [23-24], or FTIR techniques

approaching the THz spectrum from the infrared end [25-27]. The efforts to meet in the middle have pushed the equipment capabilities for these respective measurement ranges, and have thus left gaps in the THz spectra. THz technology, a relatively new technique, began its development in the early 1980's. D.H. Auston showed the capability of semiconductors to radiate pulses of THz that can be detected by a phase-coherent method [28-29]. This phase coherence allows the Terahertz Time-Domain Spectroscopy (THz-TDS) technique to measure both the real and imaginary part of the complex permittivity simultaneously where microwave and FTIR spectrometers cannot.

2.2 THz, Microwave, and Far IR Studies of Water and Heavy Water

The literature results on the THz spectroscopy of water have concentrated on two Debye relaxation processes and the determination of their parameters. For liquid H_2O and D_2O, a slow primary relaxation of around 10 ps and a smaller, fast relaxation in the range of 200 fs [14-18, 30, 31]. A few microwave measurements have agreed with this [23, 24], or at least have determined a primary relaxation [32, 33-39, 40-41].

Interestingly enough, many of the IR and Raman H_2O spectra do not report any relaxation times, but instead show an oscillation in the low THz range. Both Hasted [25-27] and Zelsmann's IR data [42] report 50 cm^{-1} resonance. For the case of D_2O, Zelsmann reports a similar feature around the same location and the measurements of Afsar and Hasted agree with this using the DFTS technique.

These high frequency oscillations from the far IR spectra must be accounted for when attempting to measure spectral features that occur at lower frequencies, such as the measurements made in this work. Specifically, Zelsmann's data can be examined to illustrate this point. He obtained the complex index spectra for ordinary and heavy water at various temperatures in the frequency range between 0.5 THz and 18 THz. Although he does not provide any fit functions for the features that he observed, his data is described well by fitting a single Debye relaxation and 4 Lorentzians to his data in the reduced polarization form. In figure 2.2, the imaginary portion of Zelsmann's data in reduced polarization form is shown along with the fit function constituents. From here it is quite apparent that there is a significant contribution of the 5 THz band, and to a lesser extent the 13 and 16 THz bands, to the total dielectric spectrum between 0.5 and 2 THz. Figure 2.3 quantifies these contributions for the three highest frequency Lorentzians.

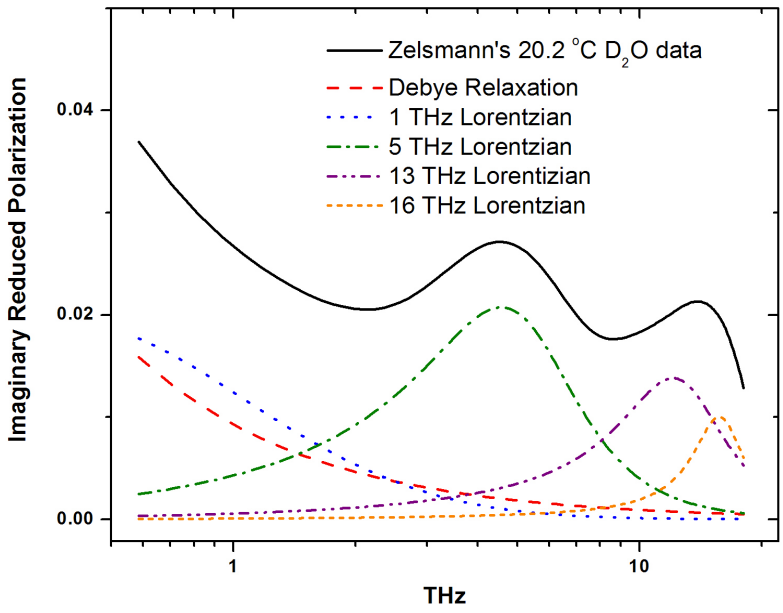

Figure 2.2 Imaginary portion of Zelsmann's D_2O Far IR data at 20.2 °C in reduced polarization form. 2 Debye and 4 Lorentzian fit constituents also shown.

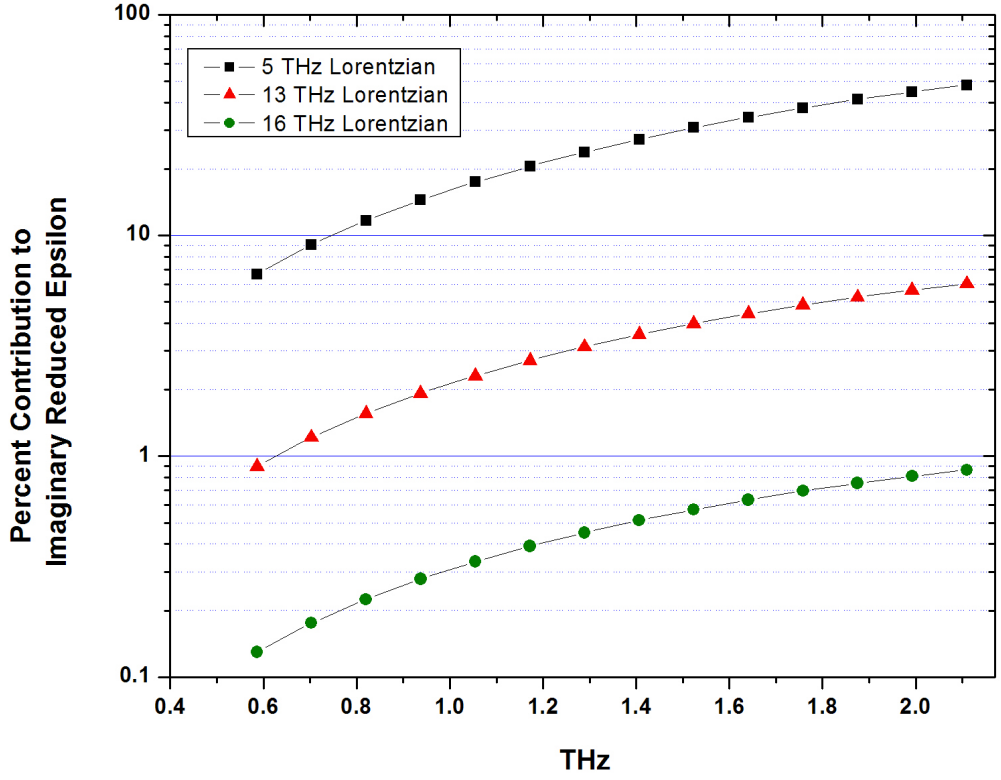

Figure 2.3 Contributions of highest frequency features to the imaginary reduced polarization of Zelsmann's 20.2 ^{o}C D_2O data.

In the past, neglecting to consider these high frequency features for measurements in the range between 100 GHz and 2 THz has resulted in abnormally high values for ε_∞ in H_2O [27]. Additionally, the disagreement of reported values for a secondary relaxation time, τ_2, is most likely a consequence of this as well.

Chapter 3 Experimental Setup

3.1 THz Spectrometer Design

The THz Spectrometer employs a Spectra-Physics Tsunami Ti:Sapphire laser pumped by a Y:VO4 Spectra-Physics Millennia V laser. The Millennia V is centered at 532 nm with 5 W of power. Its output beam is then fed into the Tsunami laser system to generate 100 fs pulses at an 82 MHz repetition rate. These pulses are centered at 780 nm with approximately 600 mW of average power.

As shown in figure 3.1, once the 780nm pulsed beam has left the laser, it is split by a 90/10 beamsplitter to create two beams: pump and probe. Receiving most of the laser power, the pump beam then goes to a Klinger delay stage with 0.1 micron resolution. The beam is passed twice over the stage to allow for a maximum time delay scan of 1.3 ns. After passing through the stage, the pump beam is then incident on the THz emitter.

When the pulsed pump beam is incident on the THz emitter, a coherent THz pulsed beam is generated. The THz radiation is collected by a 4 inch diameter 3.5 inch effective focal length off-axis parabolic (OAP) mirror. This collimates the THz beam and directs it to the sample. The transmitted radiation is then collected by second OAP that refocuses the beam back to the same size on the ZnTe detector crystal. The sample is mounted on an actuator system to allow it to slide in and out of the 4 in diameter THz beam path.

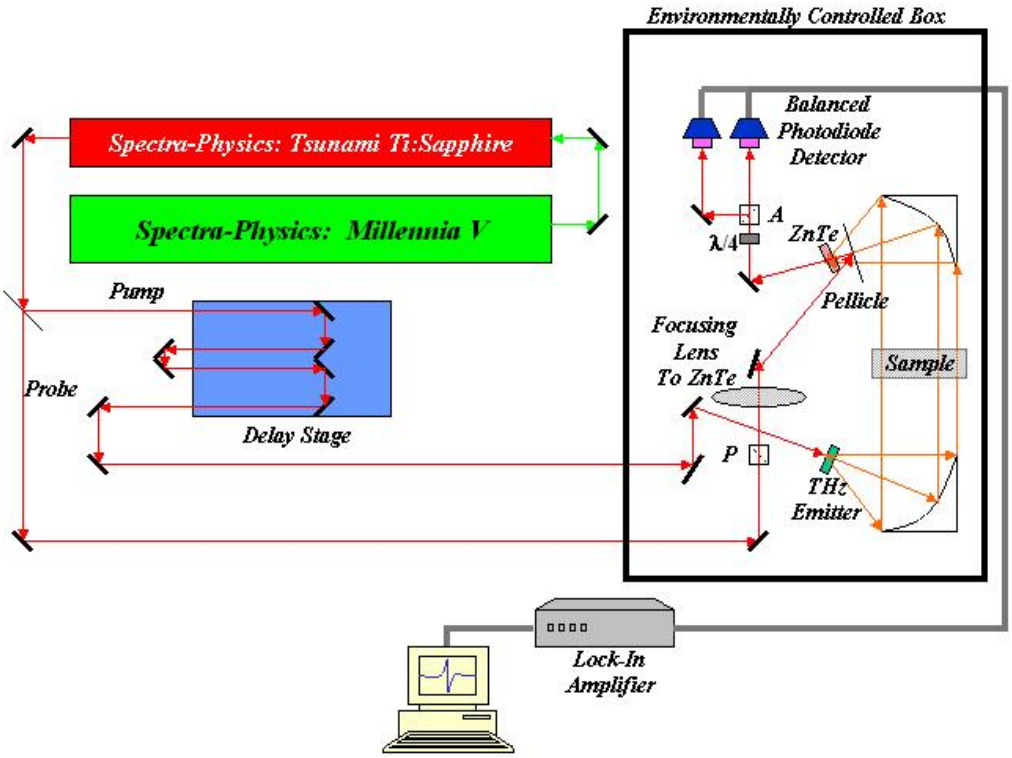

Figure 3.1 The THz Spectrometer

The probe beam passes through a Glan-Laser polarizer, P, then is reflected off a pellicle membrane and focused on the ZnTe crystal. The pellicle is transparent to the THz pump beam, but reflective for the 780 nm probe. The probe beam is then circulary polarized by a quarter-wave plate. The probe is then split by an analyzer, A, and detected by a pair of balanced photodiodes. The signal is recovered by an EG&G 7260 DSP digital lock-in amplifier and recorded on the computer. The THz system is built inside a temperature controlled and nitrogen purged box.

3.2 THz Generation, Collection, & Detection

Photoconductive antennas and optical rectification in nonlinear media are the two standard methods of generating THz pulses. In the former, high performing antennas are constructed with photoconductive substrate materials of short carrier lifetime, high mobility and high breakdown voltage [43]. To achieve this, specific substrate growing techniques and conditions are required. The latter method relies on the nonlinear properties of the emitter crystal and, in contrast to photoconductive antennas, require little device manufacturing. Although much more simple to implement, optical rectification has generally lower THz emission power between the two methods.

For the THz spectrometer used in this work, the photoconductive antenna was chosen. GaAs cut along the <100> direction obtained from the MTI corporation provides the photoconductive substrate. Two square pads of AuPd are deposited on the GaAs to form the antenna structure. The gap between the pads is chosen based on the desired bandwidth for the emitted THz pulse. Studies have shown that antenna geometry plays a big part in the performance of a photoconductive antenna [44-47]. Wires are then bonded to the pads and a voltage bias is applied. When the 780 nm pump beam is incident in the gap between the pads, valence electrons in the GaAs substrate are excited into the conduction band and THz radiation is emitted as they accelerate in the electric field caused by the bias of the AuPd pads. The polarization of the THz radiation is in the direction of the electron flow.

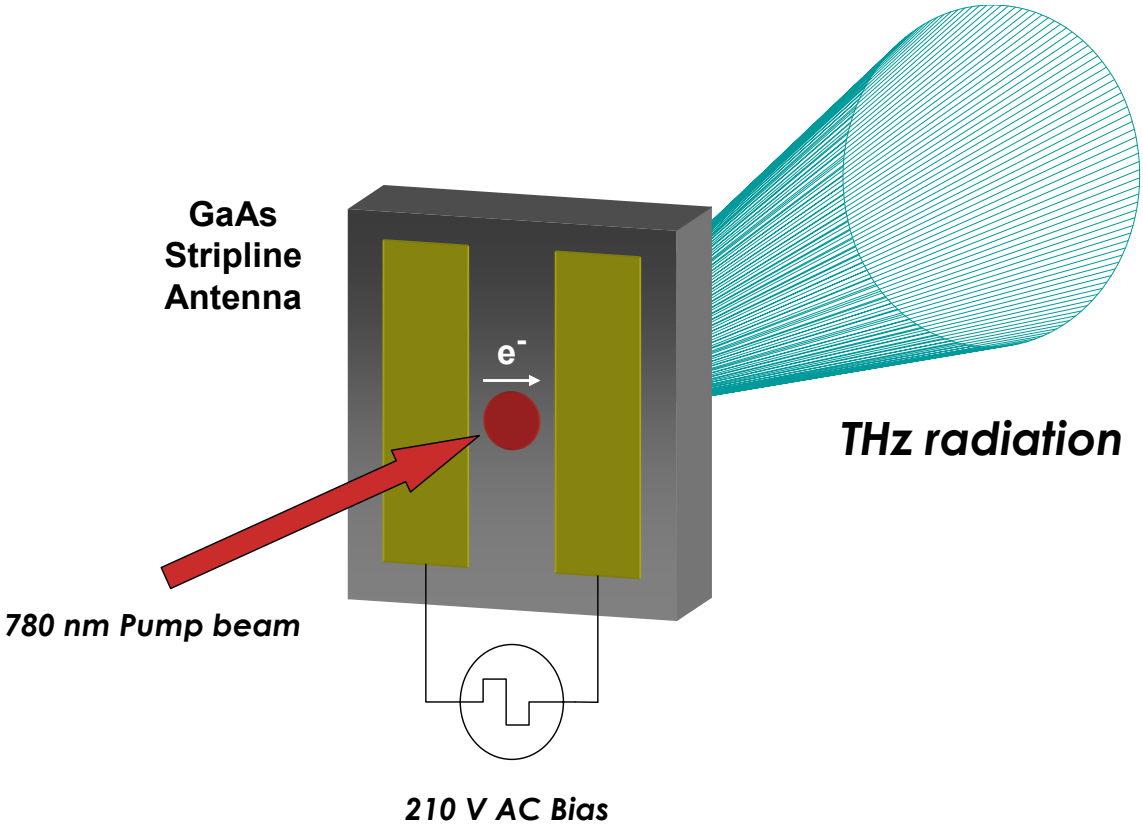

Figure 3.2 GaAs stripline photoconductive antenna

A 210 V square wave at 10 kHz is applied to the AuPd contacts generated from an FLC electronics A400 Voltage Amplifier. This causes the polarization of the THz radiation to alternate at the same frequency and allows the synchronous lock-in amplifier to detect (Background + Signal) – (Background-Signal). This technique is advantageous over mechanical chopping of the beam in that it improves the signal detection by a factor of two as well as achieving a sampling frequency at an order of magnitude higher than choppers.

Photoconductive antennas have been shown to generate extremely broadbanded THz radiation ranging between 0.3 to 30 THz [48]. These emitters require extremely

short laser pulses of 12 fs or less and specially grown LT-GaAs crystals with electrodes of very specific geometry. However, the equipment needed to fabricate these relatively exotic types of emitters is not readily available in many labs.

It has been shown that a simple solution for improving THz bandwidth at both THz and sub-THz frequencies is using a GaAs photoconductive and a ZnTe optical rectification emitter in series [49]. Another solution is to take measurements with a wide gap photoconductive antenna for sub-THz frequencies, then use a smaller gap for measurements in the higher THz range. For emitters with a large aperture of 2 mm, the 4 inch diameter OAP mirrors allow for 100% collection of frequencies above 81 GHz and 61% collection of 20 GHz frequency. The ability of these mirrors to achieve this is due to a large diameter and short effective focal length (EFL) of 2.5 inches. This short focal length bypasses the need to attach a silicon lens to the emitter to improve THz radiation collection. In addition, long time delay scans aid the in recovery of sub-THz frequencies, and will be discussed later in this chapter. A smaller aperture GaAs emitter is more suitable for recovering higher frequency THz, as shown in Figure 3.3. The overall integrated THz signal is greater but weighted towards the higher frequencies in the THz band. This is due to the smaller emitter aperture causing the THz beam to be diffracted at larger angles and thus the OAP mirror collects a smaller percentage of the sub-THz frequencies.

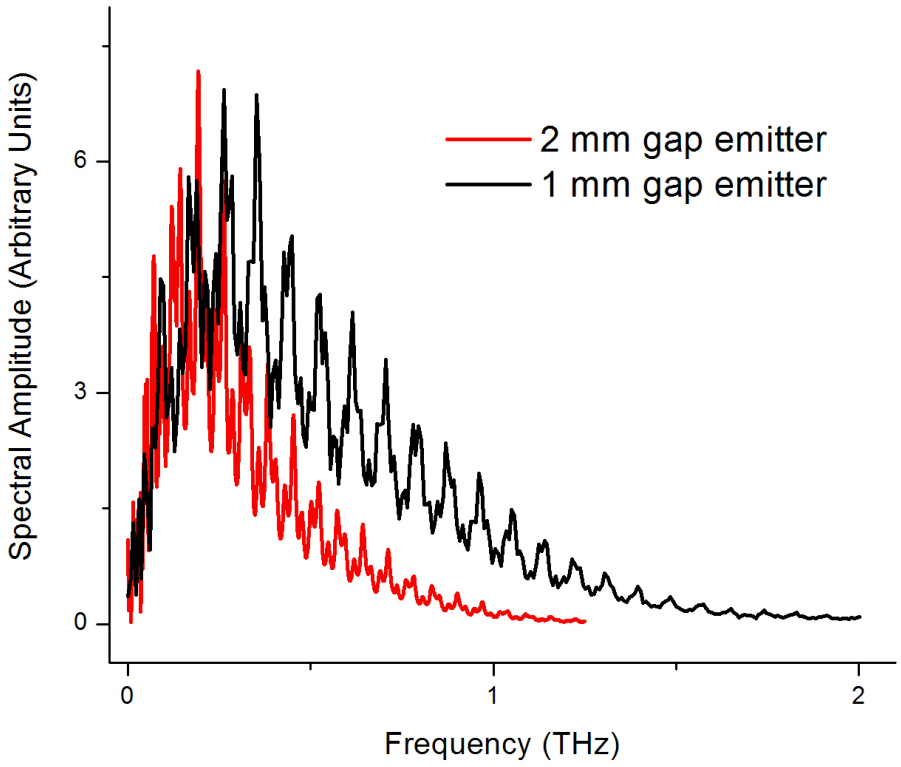

Figure 3.3 Comparison of GaAs photoconductive emitters.

The 90° OAPs manufactured from Janos Technology are essential part to the recovery of broadbanded THz radiation. They are gold coated aluminum mirrors with an effective focal length (EFL) of 2.5 inches and are 4 inches in diameter, as stated above. In contrast to this unique design, the standard 1 inch diameter 1 inch EFL mirror only allows 100% collection of frequencies above 167 GHz and 26% collection of 20 GHz.

To maximize the performance of these mirrors, they are used at an angle of 17.74° off of 90°. At this angle, the focused beam of the parabola is bisected to so that both the left and right halves of the mirror collect the same THz spectrum. In addition the

focusing and collimating mirrors are placed 5 inches apart. This is just wide enough to allow the sample cell to slide in and out of the THz beam path while short enough to prevent signal loss due to diffraction.

Similar to the generation of THz, photoconductive antennas or non-linear crystals can be used to detect freely propagating THz waves. The use of non-linear crystals for electro-optic detection [50-52] has proven to be advantageous over photoconductive antenna detection due to the larger bandwidth and superior signal to noise [53-54].

Electro-optic (EO) detection is based on the Pockel's effect. When a THz pulse beam is incident on an EO crystal, the strain of the applied field induces a modification of the index ellipsoid, namely birefringence. This change causes the linearly polarized probe beam copropagating with the THz to undergo phase retardation. For small applied fields, the amount of phase retardation is linearly proportional to the strength of the applied field [55]. This phenomenon is discussed in further detail in Appendix A and depicted in figure 3.4.

When the probe beam passes through the EO crystal, in this case ZnTe, without any THz field present, the phase of the probe beam does not undergo any retardation. The linearly polarized probe beam then becomes circularly polarized when passed through a quarter-wave plate and subsequently evenly split into constituent S and P polarizations after passing an analyzer. Equal amounts of light are sent to two separate photodiodes that independently measure (background + signal) or (background – signal). The diodes are subtracted before the reaching the lock-in amplifier resulting in zero

signal. The balancing of the diodes in this manner has the effect of removing nearly all background laser noise from the signal as it is coherently subtracted out.

Once the photodiodes have been balanced, the THz signal is measured. When a THz field is present in the ZnTe crystal, the now rotated probe beam becomes elliptically polarized when passed through the quarter-wave plate. Then when passed through the analyzer, the probe beam will be unevenly split due to more light being polarized in either the S or P direction. Thus when the balanced diodes are coherently subtracted in this case, the difference is recorded as signal by the lock-in amplifier.

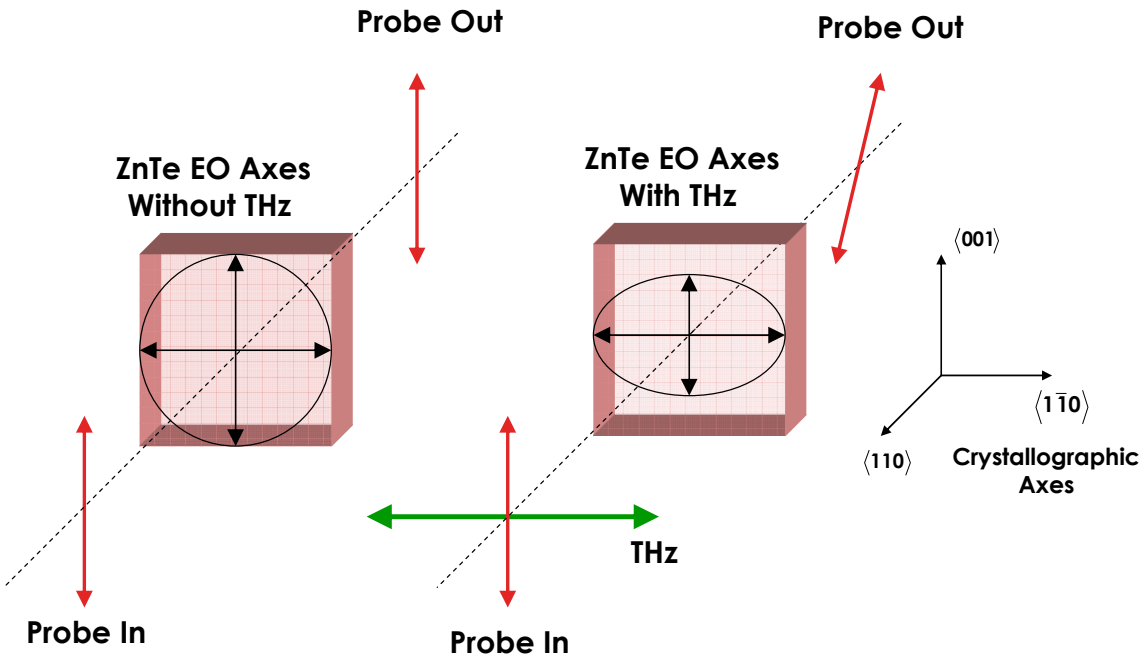

Figure 3.4 Electro-optic detection of THz in ZnTe

3.3 Temperature Control

Due to the highly temperature dependent properties of liquid water, temperature stability is of extreme importance. Not only is the control of the sample temperature necessary, but purging the space where the THz beam propagates must be done as well. This is to ensure that the absorption of water vapor will not affect the measurement of the THz radiation transmitted through the sample.

A thermally insulated box surrounds the portion of the spectrometer that involves the THz generation and detection, and the sample. It is constructed out of 1/8 inch acrylic and is double walled with a ¾ inch air gap for thermal insulation. To further insulate the environment inside the box, 1/8 inch foam padding is used to cover the table where the system is mounted. The 780 nm pulsed pump and probe input beam holes are sealed with glass cover slides. The blow-off gas from a liquid nitrogen tank is fed into the box to create a constant overpressure to purge, and keep out, water vapor. This type of nitrogen is extremely dry when compared to compressed nitrogen gas.

The primary level of sample temperature control is the temperature regulation of the brass sample cell holder. The brass holder frames the sample cell and is hollowed out to allow chilled or heated propylene glycol solution (antifreeze) to circulate within the frame. The coolant temperature is set with a Neslab RTE-7 recirculating chiller bath and maintains an accuracy of 0.1 ^{o}C.

The second level is regulating the temperature of the nitrogen purge gas. Before the nitrogen is fed into the insulated box, it first flows through a copper coil, which is

submerged inside a bath of antifreeze. The temperature of the bath is regulated by a Neslab RTE-17 recirculating chiller bath, with an accuracy of 0.1 ^{o}C as well.

The third and final level is to use the antifreeze from the Neslab RTE-17 to circulate within copper tubing coils placed throughout the insulating box. This is done to further regulate the nitrogen gas temperature and to remove thermal gradients within the entire box. With the three levels of temperature control working in concert, the thermal stability of the sample is maintained to within 0.1 ^{o}C. This is illustrated in figure 3.5.

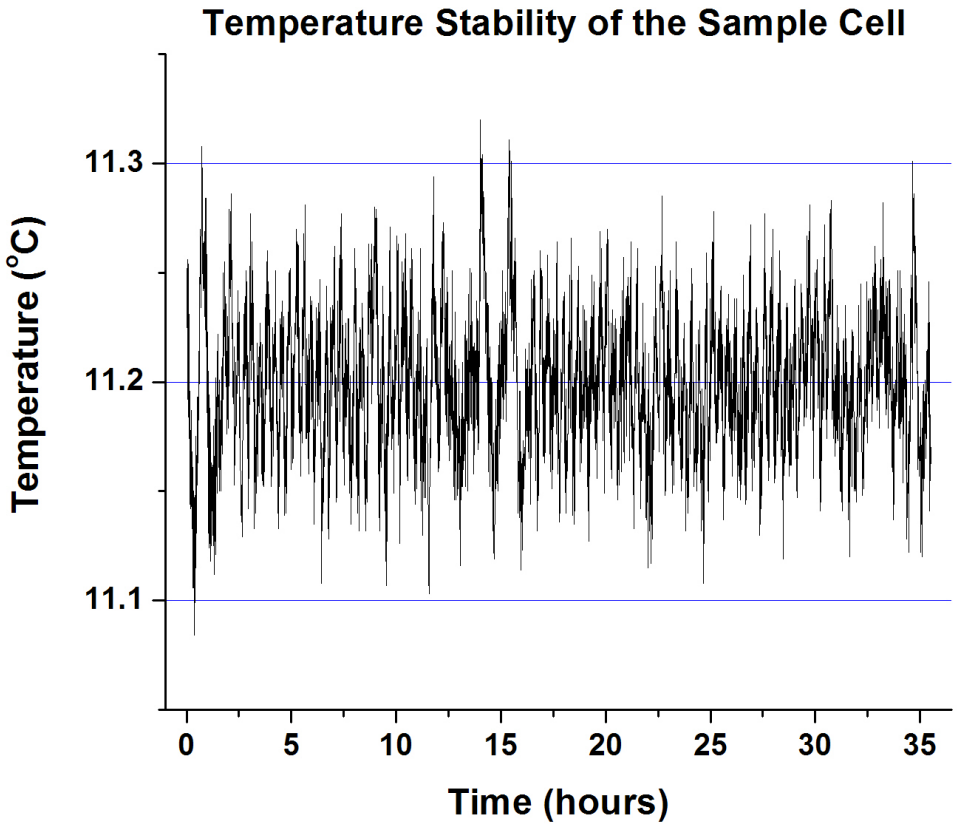

Figure 3.5 Temperature Stability of the Sample Cell

3.4 Sample Preparation

The D_2O was obtained from Cambridge Isotope and is 99.9% pure. It is kept sealed and refrigerated until ready for use. The fused silica windows and the Teflon spacer of the sample cell are cleaned using a solution that is one part hydrogen peroxide to three parts sulfuric acid, then rinsed thoroughly with HPLC (High Purity, Low Conductivity) water. Upon drying, the Teflon gasket is sandwiched between the fused silica windows creating a volume for the sample to be injected in. The cell is held together by the brass frame and sealed to prevent leaks. D_2O is then injected into the cell, taking care that bubbles are avoided. Once injected, the D_2O only comes in contact with the fused silica windows and the Teflon spacer.

The windows of the sample cell are 6-inch square plates of GE-124 fused silica with water content of less than 5 ppm. It has excellent thermal properties, and a low, flat index of refraction near 1.95 with virtually no absorption of THz radiation. The dielectric spectra of the fused silica plates were independently measured in the THz spectrometer and used in the calculation for the D_2O spectrum. A typical fused silica index of refraction spectrum is shown in figure 3.6. Unlike silicon, another transparent material in the THz range, fused silica has the advantage of being optically transparent as well. The plates are 3 mm thick.

The cell spacers are made from Teflon skived sheets in increments of 25 μm increments of thickness. The antifreeze cooled brass frame connected to a Neslab RTE-7 chiller holds the cell together.

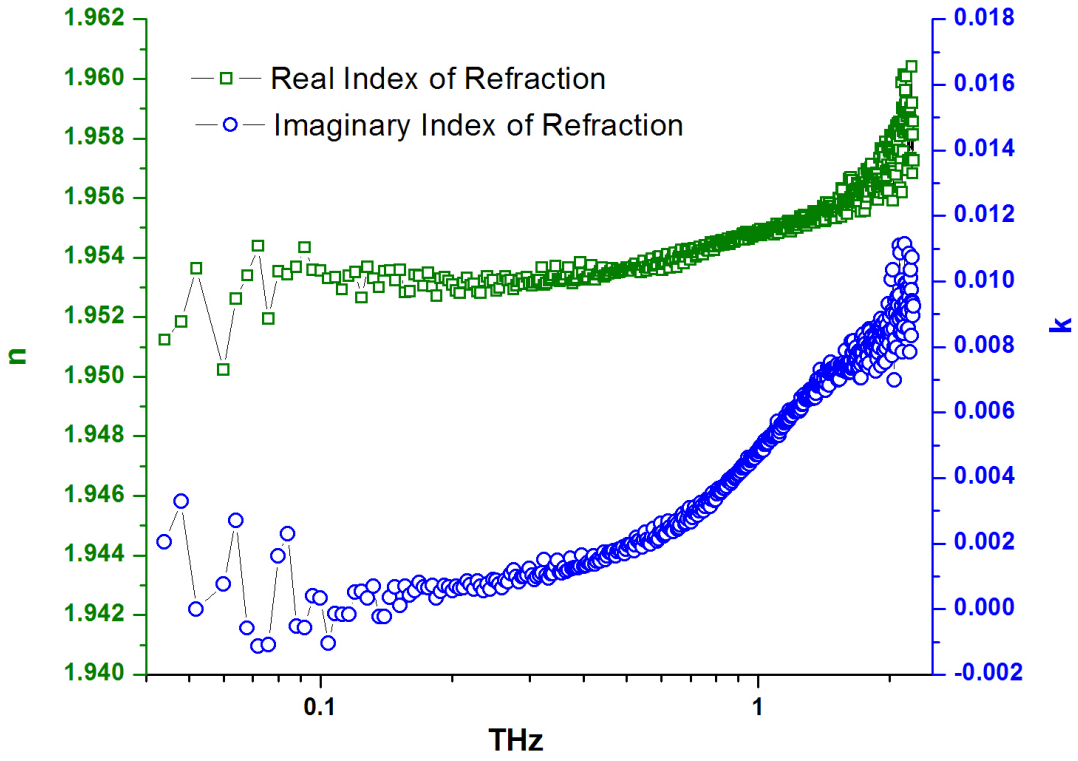

Figure 3.6 Typical measurement of the complex index of refraction for fused silica.

3.5 Data Collection

At each measured temperature, data was collected for two different cell thicknesses and three different delay times. To measure the high frequency portion of the D_2O THz spectra, a thin 100 μm Teflon cell spacer was used, due to the high absorption coefficient of D_2O. For this cell, scans of 133 ps long in steps of 33 fs were taken, corresponding to a resolution of 7.5 GHz above 1 THz. Measurements with a thicker cell of 300 μm were then taken to aid the in the recovery of the low frequency THz response

of D_2O. Scans with a total delay of 250 ps in steps of 67 fs, giving 4 GHz resolution were taken to measure frequencies between 0.1 and 1 THz. Next, scans with 1.25 ns of total delay in 200 fs steps, corresponding to a 0.8 GHz resolution, were taken to recover frequencies below 0.1 THz. Time scans of these magnitudes are necessary to achieve a low frequency resolution measurement below 100 GHz. Although the time signal is not actually zero until more than 1.5 ns have passed, scans longer than this are impractical due to the multiple reflections between the sample cell and emitter preventing the recovery of sample signal at longer time scales.

Many other THz experiments in the past have considered the collection of multiple reflections caused by the emitter, the detector, and the sample [14, 18] undesirable. In an effort to remove emitter and detector reflections, a non-responsive substrate is attached to the emitter and detector. In the detector, an index matched glue is used to join a ZnTe <110> detector crystal to a non-responsive thick slab of ZnTe <100>. This effectively increases the thickness of the detector crystal without changing the signal since ZnTe <100> does not have an EO response to the same THz field that induces one in a ZnTe <110> crystal. By the same token, a silicon lens is glued to the back of a photoconductive emitter that not only filters out the emitter reflections, but also aids in the collection of THz. However, for a measurement of low frequency signals, these techniques are to be avoided.

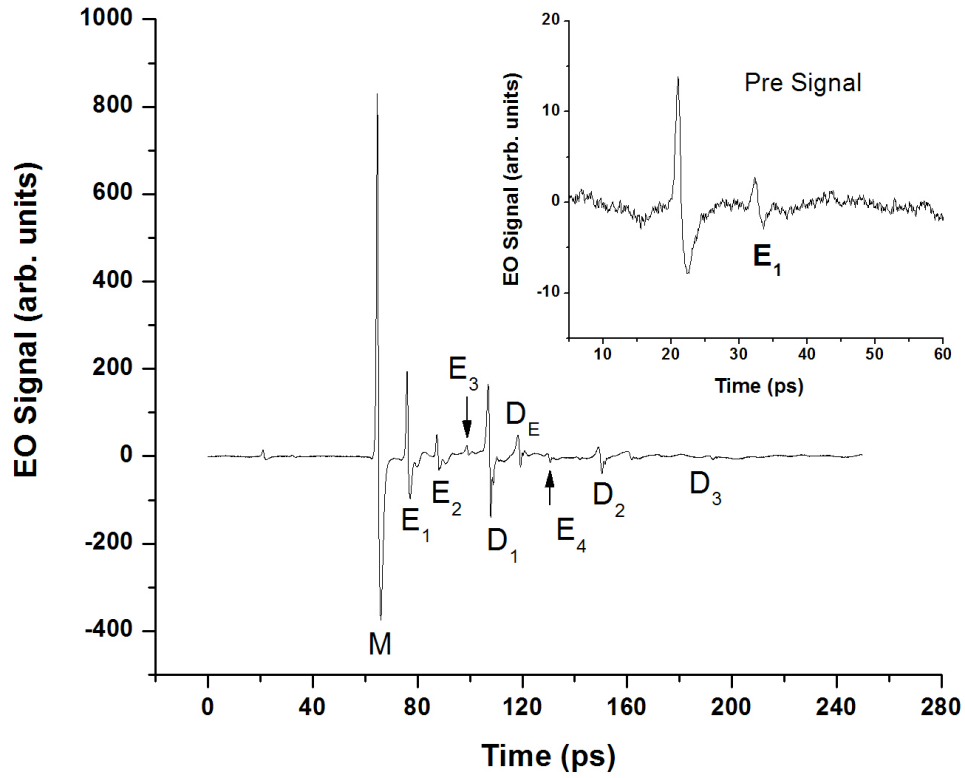

Figure 3.7 Identification of multiple reflections in a 250 ps time scan. M denotes the main THz pulse. Pulses E_1 through E_4 are reflections originating from emitter and D_1 through D_3 are from the ZnTe detector. D_E is the replication of E_1 within the detector. The inset displays the pre signal caused by the probe beam arriving early and reflecting one round trip to coincide with the THz beam.

Shown in figure 3.7 is a typical time scan of the THz beam without the sample cell. The various peaks are multiple reflections due to the emitter and the detector are retained for the simple fact that they are signal and collecting them retains more of the total integrated power generated by the emitter. A second important reason is that the measurement of the pulse train of reflections over a long time delay is a natural enhancement of the low frequency spectrum. In addition to the multiple reflections from the emitter and detector, for a time scan with the sample in the beam, collection of the

multiple reflections from within the cell provide an independent measure of the sample thickness [56]. Further discussion of this is covered in section 4.2.

Chapter 4 Signal Analysis

4.1 Conversion from Time Domain to Frequency Space

The time domain data collected contains the entire complex frequency data of the THz electric field that reaches the detector. Since the THz beam is coherent, a Fourier Transform of the time data yields the amplitude and phase of the THz field at every frequency. Thus, a calculation of the real and imaginary parts of the complex index of refraction of a material can be made simultaneously. This is opposed to solely measuring the absorption then employing the Kramers-Kronig relations to determine the real part of the index. Figure 4.1 gives a typical set of reference (no D_2O) and sample (16 ^oC D_2O) time domain scans.

Preprocessing of the time domain data must be done prior to the conversion into the frequency domain. The time window must be shifted so that the same information is collected for both the reference and the sample scans. In a sample time scan, the arrival of the THz pulse is delayed and the time window of data must be shifted to compensate. This static shift in time introduced by the index of refraction must also be accounted for in the Fourier Transform.

$$\begin{aligned} \mathscr{F}\left[f(t)\right] &= F(\omega) \\ \mathscr{F}\left[f(t+t')\right] &= e^{i\omega t'}F(\omega) \end{aligned} \tag{4.1}$$

A discrete Fourier Transform is performed to convert the time domain data to frequency space. The spectral profiles in figure 4.2 originate from the time domain data

shown in figure 4.1. According to the reference spectra, the generated THz bandwidth extends past 2.25 THz, however, due to the absorption of D_2O, the bandwidth transmitted through the sample is limited to 1.25 THz. To measure the D_2O spectra at higher frequencies, a thinner 100 μm cell is used in conjunction with a smaller aperture photoconductive emitter.

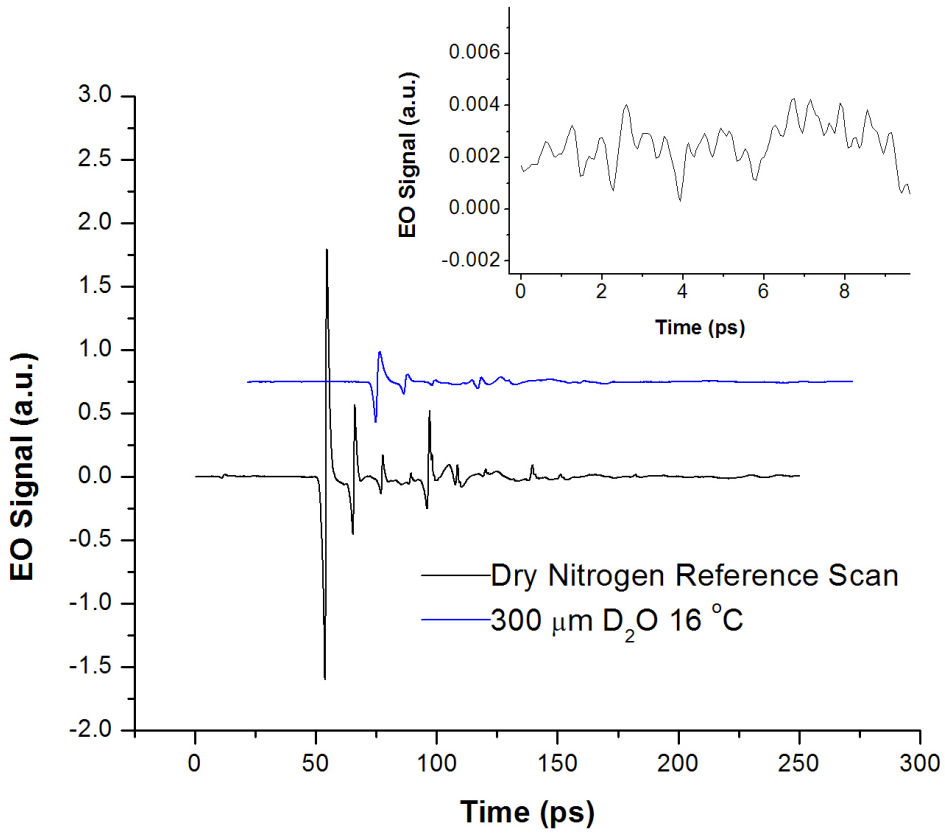

Figure 4.1 Typical reference and sample time domain data. The reference data is an average of 20 scans, and the sample data is an average of 36 scans. The sample scan has been shifted up 0.75 EO signal units from zero for clarity. The inset shows the noise level on the averaged reference data.

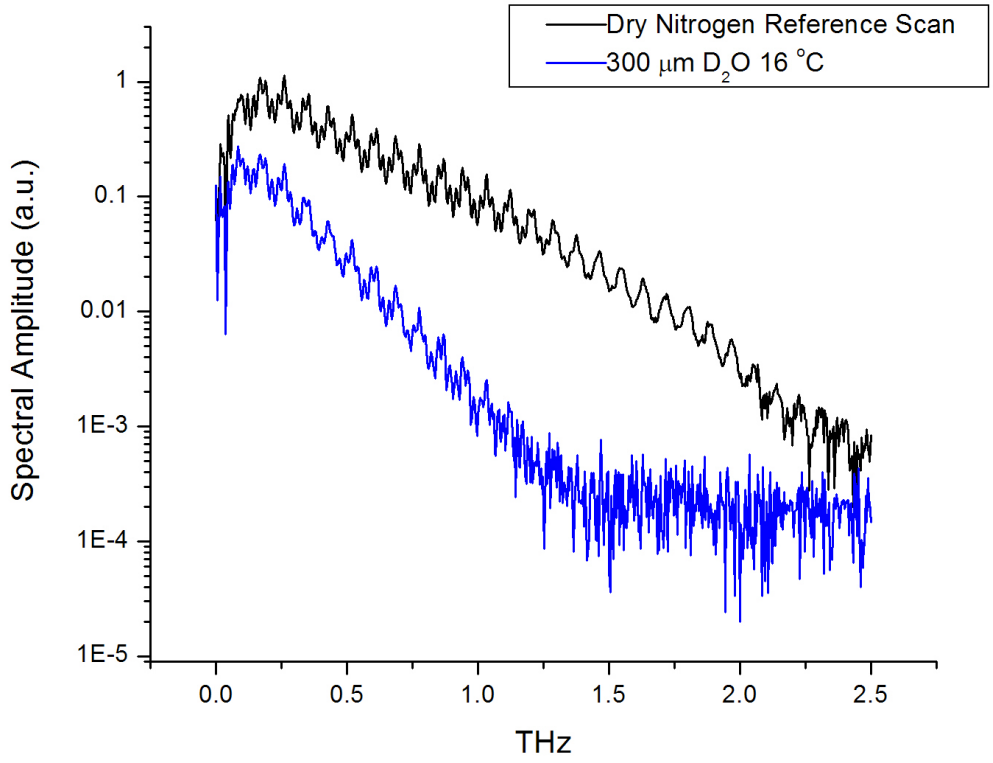

Figure 4.2 Frequency spectra profiles for the time domain data shown in figure 4.1

4.2 Calculation of the Complex Index of Refraction

If we assume the THz beam transmitted through a sample of water or D_2O is collimated, the exact solution for the index of refraction is obtained by solving Maxwell's equations for parallel waves at normal incidence on a dielectric medium.

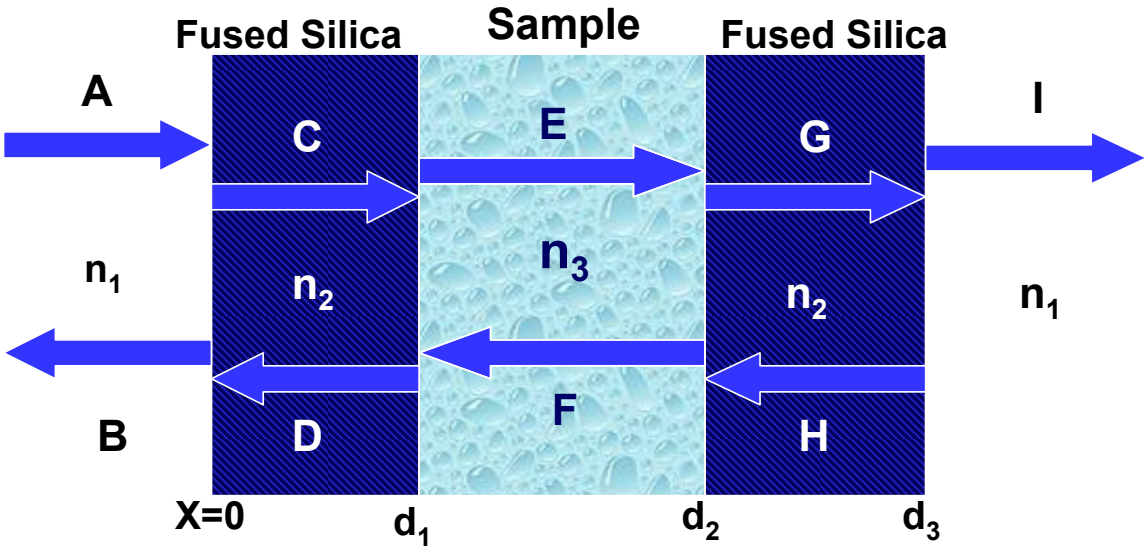

Figure 4.3 The electric field boundary value problem for the sample cell, with n_1=1 for the index of air, $\hat{n}_2$ for the fused silica index, and $\hat{n}_3$ as the sample index.

Consider the case of the sample cell shown in figure 4.3. Since E_x and $H_y = \hat{k}_z E_x$ are continuous at all boundaries, the boundary value problem at point d_1 can be expressed as

$$\begin{aligned} e^{i\hat{k}_2 d_1} C + e^{-i\hat{k}_2 d_1} D &= e^{i\hat{k}_3 d_1} E + e^{-i\hat{k}_3 d_1} F \\ \hat{n}_2 e^{i\hat{k}_2 d_1} C - \hat{n}_2 e^{-i\hat{k}_2 d_1} D &= \hat{n}_3 e^{i\hat{k}_3 d_1} E - \hat{n}_3 e^{-i\hat{k}_3 d_1} F \end{aligned} \tag{4.2}$$

Where $\hat{k} = \hat{k}_z = \omega \hat{n} / c$ and is the complex propagation vector for the THz pulse. Solving for the coefficients E and F yields the matrix equation

$$\begin{pmatrix} \dfrac{(\hat{n}_2 + \hat{n}_3) e^{i\hat{k}_2 d_1}}{2\hat{n}_3 e^{i\hat{k}_3 d_1}} & \dfrac{(-\hat{n}_2 + \hat{n}_3) e^{-i\hat{k}_2 d_1}}{2\hat{n}_3 e^{i\hat{k}_3 d_1}} \\ \dfrac{(-\hat{n}_2 + \hat{n}_3) e^{i\hat{k}_2 d_1}}{2\hat{n}_3 e^{-i\hat{k}_3 d_1}} & \dfrac{(\hat{n}_2 + \hat{n}_3) e^{-i\hat{k}_2 d_1}}{2\hat{n}_3 e^{-i\hat{k}_3 d_1}} \end{pmatrix} \begin{pmatrix} C \\ D \end{pmatrix} = \begin{pmatrix} E \\ F \end{pmatrix} \tag{4.3}$$

The boundary value problem can be solved for all the boundaries in the cell to obtain a set of matrix equations:

$$\begin{pmatrix} \frac{(\hat{n}_1+\hat{n}_2)}{2\hat{n}_2} & \frac{(-\hat{n}_1+\hat{n}_2)}{2\hat{n}_2} \\ \frac{(-\hat{n}_1+\hat{n}_2)}{2\hat{n}_2} & \frac{(\hat{n}_1+\hat{n}_2)}{2\hat{n}_2} \end{pmatrix} \begin{pmatrix} A \\ B \end{pmatrix} = \begin{pmatrix} C \\ D \end{pmatrix}$$

$$\begin{pmatrix} \frac{(\hat{n}_2+\hat{n}_3)e^{i\hat{k}_2 d_1}}{2\hat{n}_3 e^{i\hat{k}_3 d_1}} & \frac{(-\hat{n}_2+\hat{n}_3)e^{-i\hat{k}_2 d_1}}{2\hat{n}_3 e^{i\hat{k}_3 d_1}} \\ \frac{(-\hat{n}_2+\hat{n}_3)e^{i\hat{k}_2 d_1}}{2\hat{n}_3 e^{-i\hat{k}_3 d_1}} & \frac{(\hat{n}_2+\hat{n}_3)e^{-i\hat{k}_2 d_1}}{2\hat{n}_3 e^{-i\hat{k}_3 d_1}} \end{pmatrix} \begin{pmatrix} C \\ D \end{pmatrix} = \begin{pmatrix} E \\ F \end{pmatrix}$$

$$\begin{pmatrix} \frac{(\hat{n}_3+\hat{n}_2)e^{i\hat{k}_3 d_2}}{2\hat{n}_2 e^{i\hat{k}_2 d_2}} & \frac{(-\hat{n}_3+\hat{n}_2)e^{-i\hat{k}_3 d_2}}{2\hat{n}_2 e^{i\hat{k}_2 d_2}} \\ \frac{(-\hat{n}_3+\hat{n}_2)e^{i\hat{k}_3 d_2}}{2\hat{n}_2 e^{-i\hat{k}_2 d_2}} & \frac{(\hat{n}_3+\hat{n}_2)e^{-i\hat{k}_3 d_2}}{2\hat{n}_2 e^{-i\hat{k}_2 d_2}} \end{pmatrix} \begin{pmatrix} E \\ F \end{pmatrix} = \begin{pmatrix} G \\ H \end{pmatrix}$$

$$\begin{pmatrix} \frac{(\hat{n}_2+\hat{n}_1)e^{i\hat{k}_2 d_3}}{2\hat{n}_1 e^{i\hat{k}_1 d_3}} & \frac{(-\hat{n}_2+\hat{n}_1)e^{-i\hat{k}_2 d_3}}{2\hat{n}_1 e^{i\hat{k}_1 d_3}} \\ \frac{(-\hat{n}_2+\hat{n}_1)e^{i\hat{k}_2 d_3}}{2\hat{n}_1 e^{-i\hat{k}_1 d_3}} & \frac{(\hat{n}_2+\hat{n}_1)e^{-i\hat{k}_2 d_3}}{2\hat{n}_1 e^{-i\hat{k}_1 d_3}} \end{pmatrix} \begin{pmatrix} G \\ H \end{pmatrix} = \begin{pmatrix} I \\ J=0 \end{pmatrix} \tag{4.4}$$

Multiplication of the matrices yields

$$M \begin{pmatrix} A \\ B \end{pmatrix} = \begin{pmatrix} I \\ J=0 \end{pmatrix} \tag{4.5}$$

Where the full expression of M is

$$M = \begin{pmatrix} \frac{(\hat{n}_2+\hat{n}_1)e^{i\hat{k}_2 d_3}}{2\hat{n}_1 e^{i\hat{k}_1 d_3}} & \frac{(-\hat{n}_2+\hat{n}_1)e^{-i\hat{k}_2 d_3}}{2\hat{n}_1 e^{i\hat{k}_1 d_3}} \\ \frac{(-\hat{n}_2+\hat{n}_1)e^{i\hat{k}_2 d_3}}{2\hat{n}_1 e^{-i\hat{k}_1 d_3}} & \frac{(\hat{n}_2+\hat{n}_1)e^{-i\hat{k}_2 d_3}}{2\hat{n}_1 e^{-i\hat{k}_1 d_3}} \end{pmatrix} \begin{pmatrix} \frac{(\hat{n}_3+\hat{n}_2)e^{i\hat{k}_3 d_2}}{2\hat{n}_2 e^{i\hat{k}_2 d_2}} & \frac{(-\hat{n}_3+\hat{n}_2)e^{-i\hat{k}_3 d_2}}{2\hat{n}_2 e^{i\hat{k}_2 d_2}} \\ \frac{(-\hat{n}_3+\hat{n}_2)e^{i\hat{k}_3 d_2}}{2\hat{n}_2 e^{-i\hat{k}_2 d_2}} & \frac{(\hat{n}_3+\hat{n}_2)e^{-i\hat{k}_3 d_2}}{2\hat{n}_2 e^{-i\hat{k}_2 d_2}} \end{pmatrix} \times$$
$$\begin{pmatrix} \frac{(\hat{n}_2+\hat{n}_3)e^{i\hat{k}_2 d_1}}{2\hat{n}_3 e^{i\hat{k}_3 d_1}} & \frac{(-\hat{n}_2+\hat{n}_3)e^{-i\hat{k}_2 d_1}}{2\hat{n}_3 e^{i\hat{k}_3 d_1}} \\ \frac{(-\hat{n}_2+\hat{n}_3)e^{i\hat{k}_2 d_1}}{2\hat{n}_3 e^{-i\hat{k}_3 d_1}} & \frac{(\hat{n}_2+\hat{n}_3)e^{-i\hat{k}_2 d_1}}{2\hat{n}_3 e^{-i\hat{k}_3 d_1}} \end{pmatrix} \begin{pmatrix} \frac{(\hat{n}_1+\hat{n}_2)}{2\hat{n}_2} & \frac{(-\hat{n}_1+\hat{n}_2)}{2\hat{n}_2} \\ \frac{(-\hat{n}_1+\hat{n}_2)}{2\hat{n}_2} & \frac{(\hat{n}_1+\hat{n}_2)}{2\hat{n}_2} \end{pmatrix} \tag{4.6}$$

Therefore, the transmitted field **I** is related to the incident field **A** by

$$I = \left(M_{11} - \frac{M_{12}M_{21}}{M_{22}} \right) A \tag{4.7}$$

By experimentally determining the transmitted THz field (I) from sample scans and the incident field (A) from reference scans, one can solve for the matrix elements and hence the complex index $\hat{n}$ in the above expression. The ratio of the absolute values of the spectral profiles shown in figure 4.2 is exhibited in figure 4.4. This ratio corresponds directly to the matrix values in equation 4.7.

The ratio of reference to sample scans is not solely a measurement of the index of refraction, but is actually the index multiplied by the sample cell thickness. An independent measurement of the cell thickness is difficult in this case since the accuracy of the length must be within a percent of the THz beam wavelength to in turn obtain an accurate measurement of the index. However, in collecting the multiple reflections from inside the sample, the frequency spectrum develops resonance peaks that depend on the product of the real index times the cell thickness. Incorrect values of the cell thickness,

which include the thicknesses of the two fused silica windows and the sample, result in oscillatory behavior in the index of refraction. By minimizing these false effects, the index of refraction can be correctly determined [56].

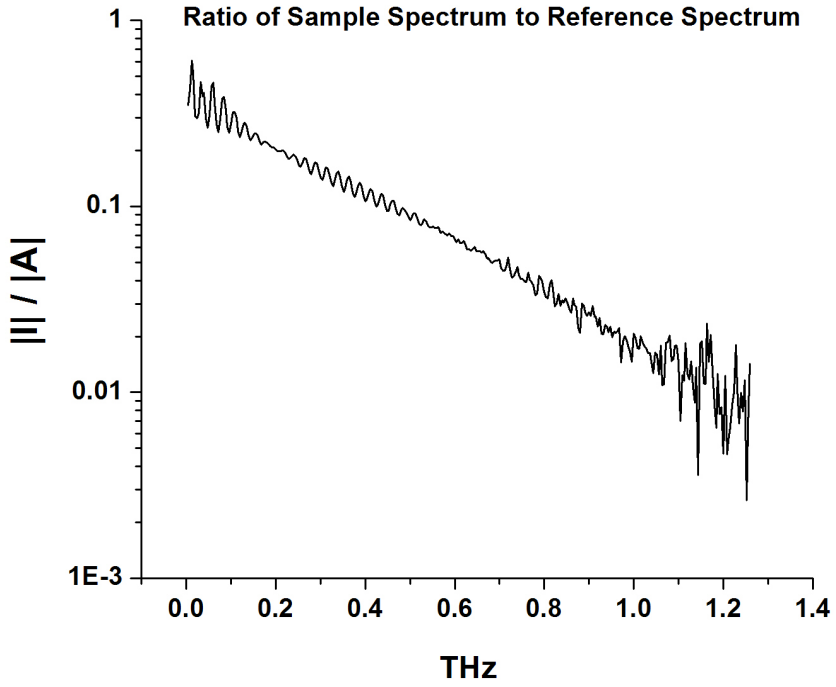

Figure 4.4 The ratio of incident (A) to transmitted (I) THz spectral profiles shown in figure 4.2. The sample is D_2O at 16 ^oC, 300 μm thick.

4.3 Analysis of Error

All experiments, no matter how diligently executed, are subject to measurement and systematic errors. Measurement errors are reduced by repeating the same measurement many times to minimize the standard error. Systematic errors, on the other hand, are intrinsic to the experiment and can be controlled.

In the case of this experiment, the laser system is the main source of noise. The $Y:VO_4$ laser is highly susceptible to changes in the environment that cause fluctuations in power and variations in beam direction. Changes in lab environment conditions have the additional effects on the mode-locked Ti:Sapphire laser, such as deviation in center frequency, change of bandwidth or loss of mode-lock.

A small portion of the 780 nm Ti:Sapphire beam is picked off and directed to a Jarrell Ash monochrometer where its spectrum is read out by a linear diode array. A Tektronics TDS 210 Digital Real-Time oscilloscope then digitizes and displays the spectrum. This information is captured and saved to the computer after a scan has been completed so it can be inspected and compared with other scans.

The directional drift in the beam is monitored by imaging the small portion of the probe beam that is transmitted through the pellicle. This beam is passed through several filters then focused on a USB CCD camera that has had its camera lens removed. Pictures are taken at regular intervals so that the progression of the laser drift can be measured.

The sample cell is moved in and out of the beam to measure reference and sample scan in an alternating fashion. This is done to further reduce the error associated to slow laser drifts that occur over an entire set of scans. As such, the position of the sample cell must be in the same orientation each time it is moved into the beam. The orientation is monitored by a HeNe laser that is reflected off the glass cell and is imaged on a USB CCD camera. As long as the beam does not stray from the camera, the cell orientation is

the same. However, if the cell does deviate, this monitoring allows for the sample cell to be adjusted in the same orientation that is accurate to within 0.1 degrees.

Chapter 5 Results and Modeling of Data

5.1 Data and Errorbars

The dielectric spectra for D_2O at five different temperatures span a frequency range of 15 GHz to 2 THz. The real (ε') and imaginary (ε") parts of spectra are given in figures 5.1 and 5.2, respectively. The data shown has undergone a 5 point adjacent average smoothing.

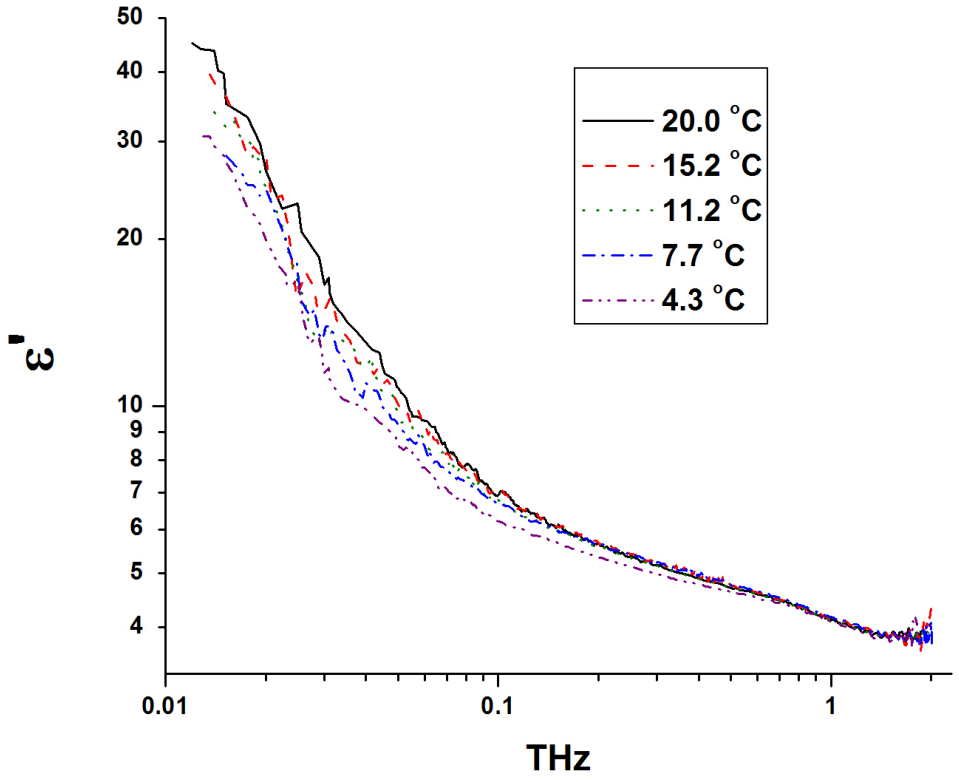

Figure 5.1 Real part of the complex permittivity for D_2O at all five temperatures.

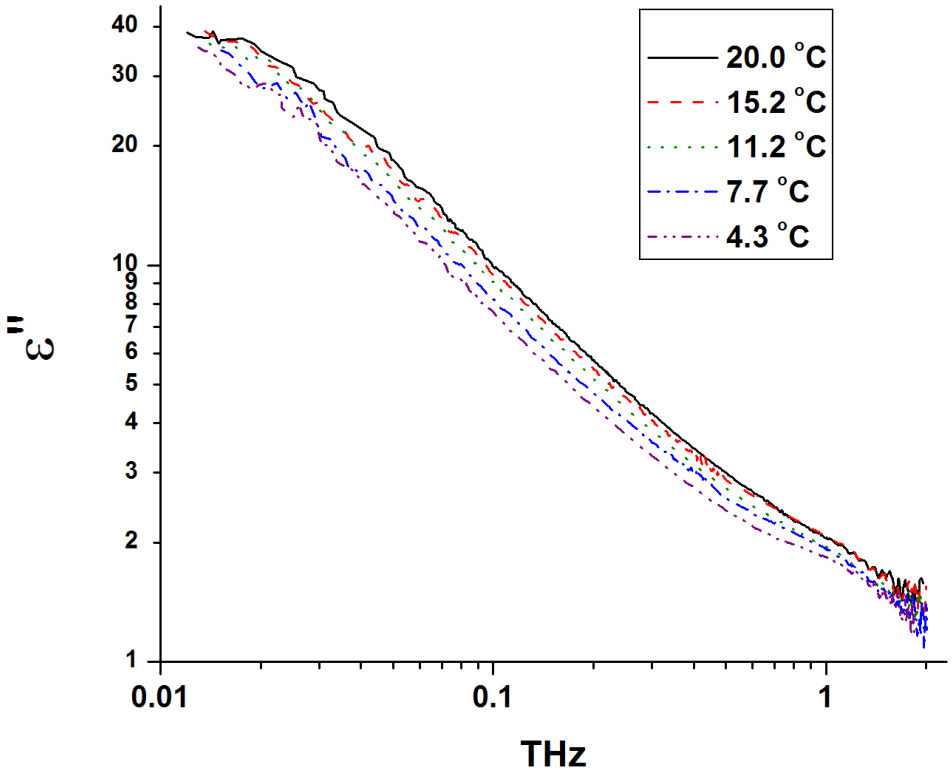

Figure 5.2 Negative imaginary part of the complex permittivity for D_2O at all five temperatures.

The percent error for the real and imaginary parts of the permittivity spectra is given in figure 5.3 for each temperature. In the range of 50 GHz to past 1 THz, the typical error in the real and imaginary parts is on the order of 1% or less. The larger error percentage at the low end of the spectra is due to the difficulty in collecting these low signals diffracting from the emitter at large angles. The increase of error percentage at the higher frequencies is due to the relatively low values of the permittivity. The error was calculated by propagating the error in the ratio of reference to sample Fourier transforms through the root finding routine used to solve for the index in equations 4.6

and 4.7. This is necessary due to the fact that the equation to solve for the index of D_2O is non-separable.

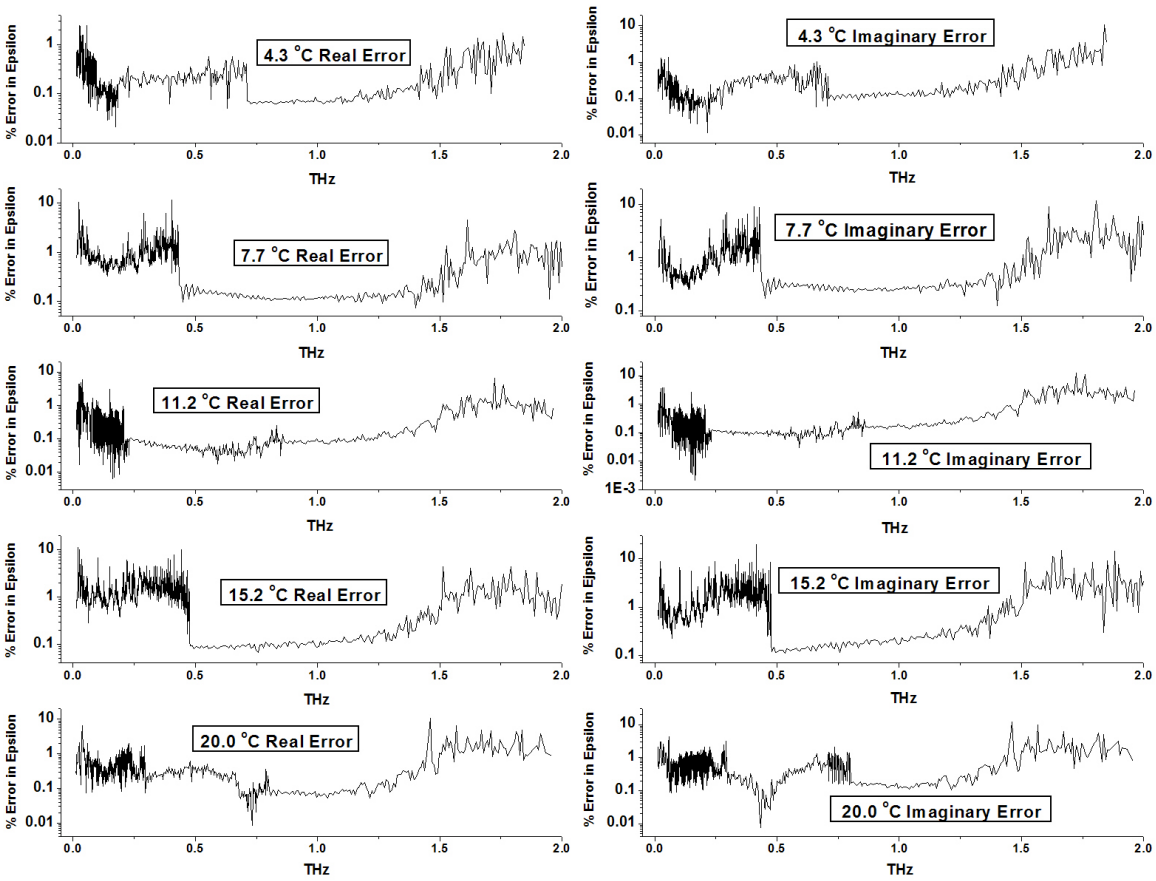

Figure 5.3 Error percentages in the measured permittivity spectra for the five D_2O temperatures.

5.2 Complete Data Fits

5.2.1 Fitting Procedure

The D_2O permittivity spectra shown are composed of three different time domain scans giving three different frequency resolutions, as discussed in section 3.5. The measurement in the region below 100 GHz has a resolution of 0.8 GHz. Data in the

range between 100 and 750 GHz has a 4 GHz resolution. The data across these two ranges were measurements of a 300 μm cell with a 2 mm aperture emitter. A 1 mm emitter and a 100 μm cell were used to measure the spectra between 750 GHz to 2 THz with a 7.5 GHz resolution. The exceptions are the 7.7 ^{o}C and 15.2 ^{o}C spectra, where from 15 to 450 GHz, they have a 0.8 GHz resolution, and from 450 GHz to 2 THz the data is spaced at 7.5 GHz. These different ranges of frequency resolution overlapped and the average mismatch in epsilon was less than 0.01 in absolute magnitude.

Microwave data from Yastremskii [41] and FIR data from Zelsmann [42] were interpolated to the five D_2O temperatures measured in the present work. The interpolated data were then joined to the ends of THz spectra to generate a broad range of data spanning 0.8 GHz to 18 THz. This is done to ensure the fit parameters near the ends of the THz spectra, where the noise level is higher, are plausible and accurate, i.e. noise fluctuations are not mistaken for actual spectral features. The fit functions and the interpolated data are discussed in Appendix C.

In the case of the THz spectrum for H_2O, the addition of the FIR data has shown to be extremely important for accurate fits [49]. Although a host of measurements for the dielectric spectra of water, and a few for heavy water, below 2 THz have been made [14-18, 23, 25-27, 30, 32, 42, 57-58], the reported literature values of the permittivity in the high frequency limit, ε_∞, are inconsistent. This is due to the value of ε_∞ being strongly determined by the highest frequency measured [26]. In addition, the contributions of the 1.5 and 5 THz oscillations seen in IR and Raman spectra are substantial down to below 800 GHz, as shown in figures 2.2 and 2.3. Since many of the

literature data in this range use a two Debye relaxation model, these features are neglected in their data, thus leading to values of ε_∞ that differ from the theoretical limit of $\varepsilon_\infty = n^2 \approx 1.8$.

The reduced microscopic polarization expressed in equation 1.6 was used to generate a complete fit to the D_2O spectra. It has been found that the reduced polarization can be modeled as a sum of two Debye relaxations and ten Lorentzian oscillators given as

$$\frac{(\hat{\varepsilon}(\omega)-\varepsilon_\infty)(2\hat{\varepsilon}(\omega)-\varepsilon_\infty)\varepsilon_0}{(\varepsilon_0-\varepsilon_\infty)(2\varepsilon_0-\varepsilon_\infty)\hat{\varepsilon}(\omega)} = \sum_{i=1}^{2}\frac{a_i}{1+i\omega\tau_i} + \sum_{j=1}^{10}\frac{b_j{\omega_j}^2}{{\omega_j}^2-\omega^2+i\omega\Gamma_j} \tag{5.1}$$

Some past experiments on H_2O report the main relaxation exhibits a Cole-type behavior of the form given in equation 1.12 [26-27, 38, 59-60]. However, these reported values of α ranged between 0.004 and 0.014 [38, 59-60], signifying an insignificant Cole-type behavior. Hence, the data was sufficiently fit using standard Debye relaxations.

In equation 5.1, ε_0 is the only parameter to be fixed, and is calculated from the formula

$$\varepsilon_0(T_*) = 78.25\left[1-4.617\times10^{-3}T_* + 1.22\times10^{-5}T_*^2 - 2.7\times10^{-8}T_*^3\right] \tag{5.2}$$

where $T_* = (T-25)$ and the temperature, T, is in units of degrees Celsius [16].

5.2.2 High Frequency Lorentzian Fits

The first important heavy water resonance to consider fitting is the one found near 50 cm^{-1}. FIR measurements from Zelsmann, and DFTS techniques by Afsar and Hasted report the tiny absorption band in both the D_2O and H_2O absorption spectra around 50 cm^{-1} (1.5 THz) on the side of a much larger 200 cm^{-1} (6 THz) feature [61]. The existence of the tiny feature is confirmed by molecular dynamics (MD) simulations of H_2O and is described as a hindered translational motion [62]. Although neither of them provide a fit for the feature in D_2O, Hasted does fit the H_2O analog to this feature to a Gaussian oscillator with an amplitude of 37.5 cm^{-1} and a center frequency of 49 cm^{-1} [27].

However, these results should not be taken at face value since the identification and assignment of absorption bands based on the absorption spectra, α, can be problematic. The relationship between the absorption and the permittivity is given as

$$\alpha(\nu) = \frac{4\pi\nu \,\mathrm{Im}\left[\sqrt{\hat{\varepsilon}}\right]}{c} \tag{5.3}$$

This expression reveals that the resonances that should be properly fit in the permittivity spectrum, $\hat{\varepsilon}$, are actually weighted by the frequency ν. This results in blueshifting all resonances and in addition, suppresses lower frequency features that may be near or overlap with higher frequency bands.

When fit in the reduced $\hat{\varepsilon}$ spectrum for D_2O, it has been found that for the feature near 50 cm^{-1}, its amplitude is actually comparable, and at some temperatures larger, than its 200 cm^{-1} neighbor. Additionally, we see that its amplitude is even larger

than the resonances centered between 450 and 550 cm^{-1}. The fit parameters obtained are shown in table 5.1, where ν is the center frequency in THz, Γ is the damping term in ps^{-1}, and *b* is the amplitude. Zelsmann's FIR data was used for the 5, 13, and 16 THz oscillators and were determined by the interpolation described in Appendix C. The Lorentzian parameters listed below are numbered from lowest to highest frequency in accordance with the rest of the ten fit oscillators in equation 5.1.

Temperature (^oC)	b_7	ν_7 (THz)	Γ_7 (ps^{-1})	b_8	ν_8	Γ_8
4.3	0.020786 (6E-6)	1.3159 (0.0003)	25.783 (0.014)	0.0195	5.356	34.968
7.7	0.02376 (2E-5)	1.3169 (0.0005)	26.387 (0.023)	0.0198	5.351	35.189
11.2	0.025167 (4E-6)	1.3415 (0.0001)	31.728 (0.007)	0.0200	5.345	35.416
15.2	0.01916 (1E-5)	1.2599 (0.0004)	19.899 (0.015)	0.0203	5.339	35.675
20.0	0.01852 (1E-5)	1.2170 (0.0004)	19.498 (0.015)	0.0207	5.331	35.986
	b_9	ν_9	Γ_9	b_{10}	ν_{10}	Γ_{10}
4.3	0.0075	13.484	58.749	0.0037	16.087	36.627
7.7	0.0080	13.376	59.130	0.0037	16.063	36.563
11.2	0.0085	13.265	59.522	0.0037	16.039	36.497
15.2	0.0092	13.138	59.970	0.0036	16.011	36.422
20.0	0.0099	12.986	60.508	0.0036	15.977	36.332

Table 5.1 Fit parameters for the highest frequency Lorentzian oscillators in D_2O. The variances of the parameters are in parentheses. Lorentzians 8-10 were fit using the interpolated values from Zelsmann data [42].

5.2.3 Debye Relaxation Fits

It is without doubt that a primary Debye relaxation is the dominant feature in the D_2O permittivity spectra. A less obvious, and much faster, second relaxation is included to provide a better fit of the data. These Debye relaxation fit parameters are shown in table 5.2, along with the calculated value of ε_0 and the fitted value of ε_∞. In figure 5.4, the fit constituents of the imaginary part of the reduced polarization 20.0 ^oC data are revealed to show the contributions of the two relaxations, the 1.2 THz Lorentzian, and 5.3 THz Lorentzian. The two highest frequency oscillators are not shown because their contributions are an order of magnitude lower than the 5.3 THz oscillator in the measured frequency range. These contributions are representative for all the D_2O temperatures.

Temperature (^oC)	ε_0	ε_∞	a_1	τ_1 (ps)	a_2	τ_2 (ps)
4.3	86.156	1.8940 (0.0004)	0.8411 (0.0001)	21.822 (0.003)	0.10744 (4E-5)	6.887 (0.003)
7.7	84.797	1.9171 (0.0008)	0.8724 (0.0005)	18.764 (0.010)	0.0724 (0.0001)	5.390 (0.010)
11.2	83.423	1.8829 (0.0003)	0.86052 (6E-5)	16.181 (0.001)	0.08208 (2E-5)	6.411 (0.002)
15.2	81.884	1.8644 (0.0007)	0.9108 (0.0004)	14.511 (0.006)	0.03696 (7E-5)	2.399 (0.005)
20.0	80.081	1.8652 (0.0006)	0.9369 (0.0002)	12.162 (0.003)	0.01042 (2E-5)	1.079 (0.003)

Table 5.2 Fit parameters for the two Debye relaxations, ε_0, and ε_∞.

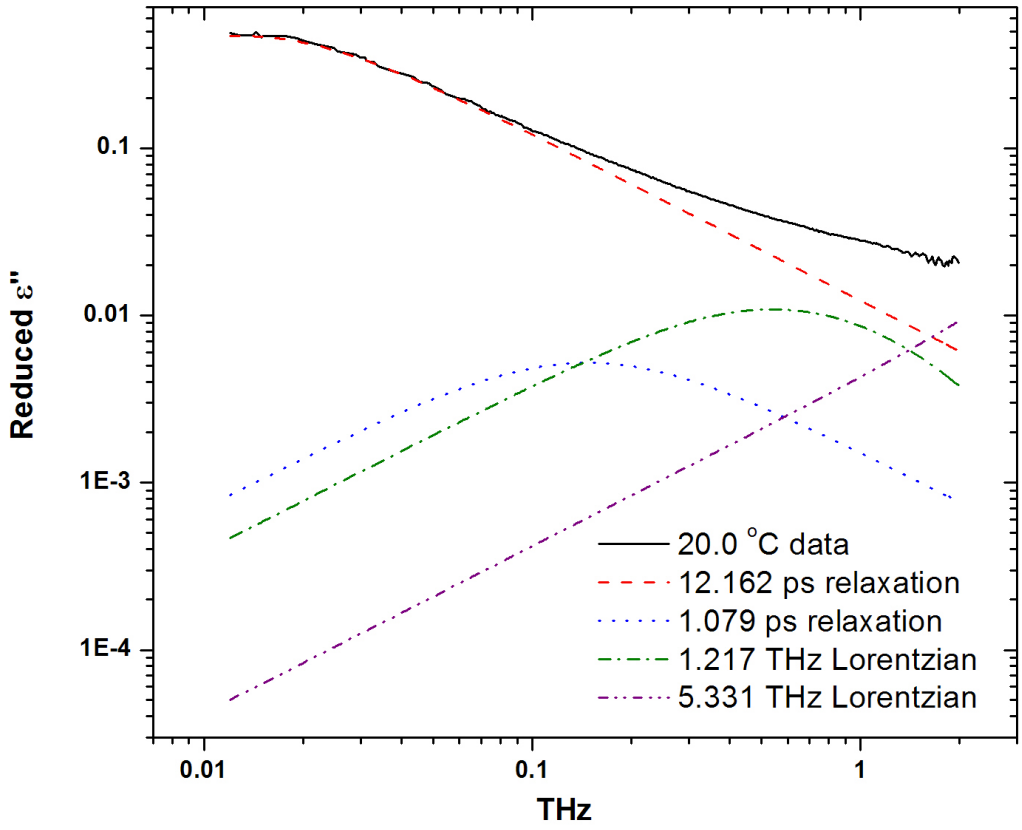

Figure 5.4 Contributions of the two Debye relaxations and the first two known Lorentzians to the imaginary part of the 20 °C reduced polarization data.

Of course, the justification for fitting two Debye relaxations does not rest solely on the fact that it provides a better fit of the data. In the H_2O literature, there are only a few results that utilize a bimodal relaxation fit, most of them coming from data taken with a THz spectrometer [14-18, 49, 57, 63-64]. The only exception is Buchner's microwave data [23-24]. Even fewer still are biexponential fitting results for D_2O [17, 49, 65]. A comparison of the Debye relaxation times for D_2O between the literature and the current THz work is illustrated in figure 5.5.

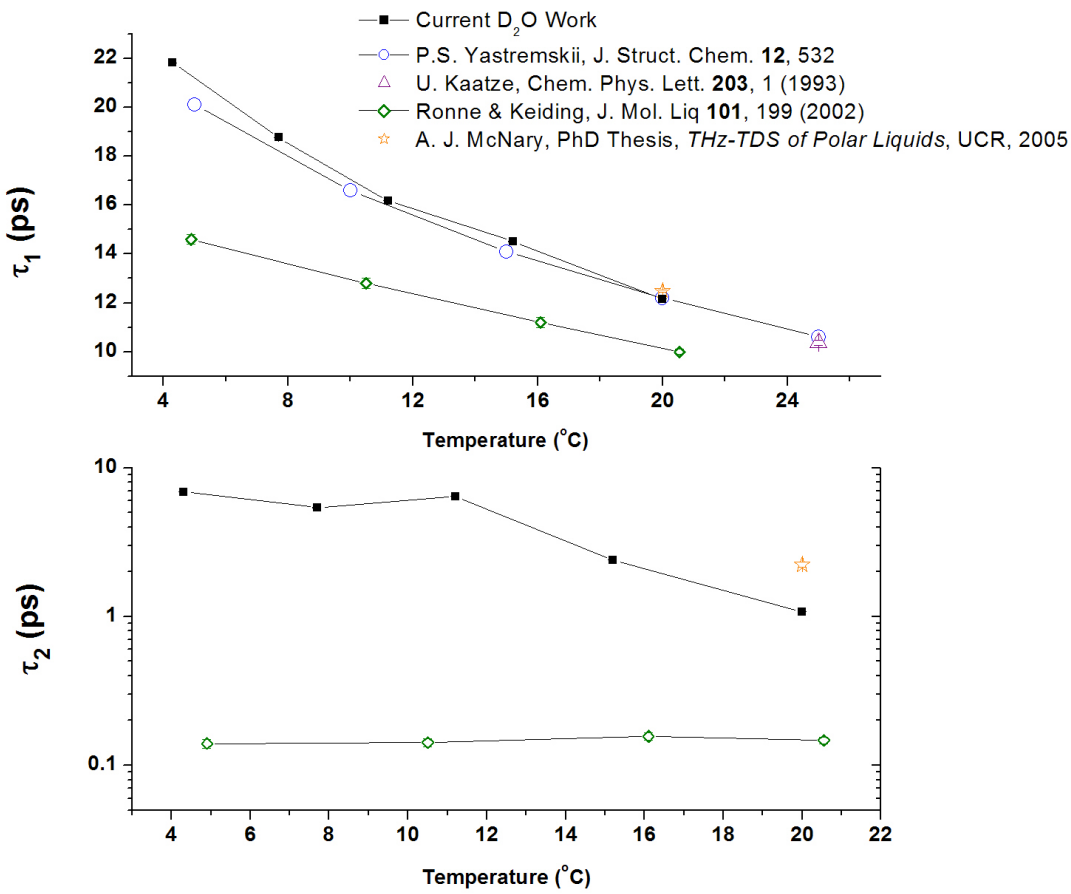

Figure 5.5 The D_2O primary and secondary relaxation times versus temperature shown with literature values.

From the figure above, the microwave values by Yastremskii and Kaatze are comparable to the current work's primary relaxation values. However, Rønne's values obtained from THz spectroscopy are lower than the current and McNary's previous study in our lab. In the secondary relaxation, this discrepancy arises from other groups actually fitting the 50 cm^{-1} resonance and the tail of the 200 cm^{-1} resonance at frequencies above 1 THz. Moreover, the Raman spectrum for heavy water, collected by Mizoguchi for temperatures between 268 K and 368 K, shows a feature near 10 cm^{-1} and is fit with a Curie-Weiss law. This fit gives a relaxation value of 7.3 ps at 278 K (5 ^{o}C)

and 5.25 ps at 293 K (20 ^{o}C), thus placing his values for a picosecond time scale relaxation somewhat closer to our measured values.

What is most interesting is the disagreement in the primary relaxation values between our THz measurements and Rønne's, but yet the apparent agreement with the trend from the microwave literature. This curious result stems from the secondary relaxation times reported in other THz groups being influenced by higher frequency spectral features that are not being fit. This inaccuracy is propagated to the fit of the slower primary relaxation, and thus it becomes a mixture of the two relaxations that exist. One may think of this as a "domino effect", where the exclusion of the high frequency features in the fit can throw all the other parameters off. However, this is not the case for the microwave measurements. The data obtained by Yastremskii measures the primary relaxation at a single frequency of 9.370 GHz [41], and because of this, he cannot measure any other processes or features that can skew the data.

Despite the low values, the other THz groups [16-17, 31] do report that the primary relaxation obeys the Stoke-Einstein-Debye (SED) model for both H_2O and D_2O. In addition, the previous THz work on H_2O in our group [49] agrees with the SED model given as

$$\tau_1 = \frac{4\pi\eta R^3}{k_B T} \tag{5.4}$$

here, R is the hydrodynamic radius of a rotating molecule, η is the shear viscosity [66], and the temperature T is in units of Kelvin [67].

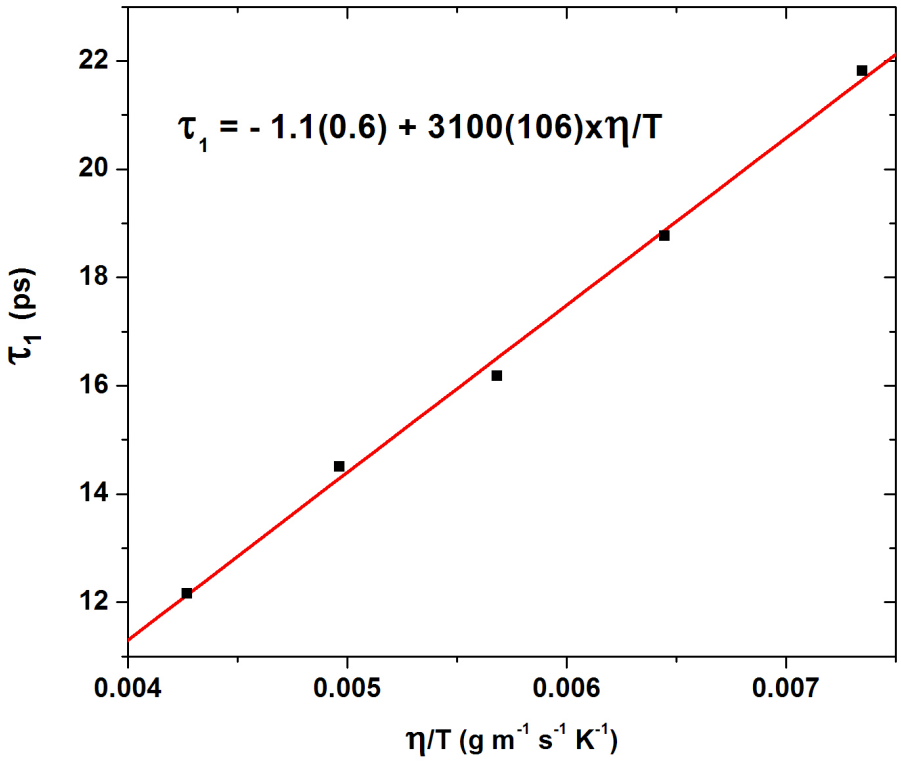

Figure 5.6 Linear fit of the primary Debye relaxation versus shear viscosity divided by temperature.

Figure 5.6 shows that the D_2O primary Debye relaxation time scales linearly with viscosity divided by temperature. The previous results on D_2O and H_2O have come to the same conclusion [15-16, 31, 49]. This linear dependence indicates that the mechanisms that preside over ordinary transport are also responsible for the primary relaxation of D_2O.

While there is a general consensus within the community that both the primary and secondary relaxations exist due to a two component liquid, the jury seems to still be out on their exact roles. Since previous THz measurements outside our group have fit extremely low values to the secondary relaxation, they adopted the notion that the second

relaxation is a single molecule reorientation effect that is borne out of a two component liquid, consisting of a low density liquid (LDL) and a high density liquid (HDL) [68-70]. The faster relaxation is associated with the HDL part of the liquid, composed of weak hydrogen bond interactions. A qualitative description of this model begins with water molecules locked in a tetrahedral structure, or cage. If this water cage were to break, it breaks in a time of the primary relaxation. These free water molecules now reorient and move to a new site in a time of the secondary relaxation [16, 31, 71].

However, if the 100 fs relaxation times are considered to be a result of improper fitting of high frequency data, then the secondary relaxation increases roughly by an order of magnitude. This does not rule out the idea of a two component liquid, but it does however eliminate the single molecule reorientation as a possible mechanism to explain the secondary relaxations. In addition, MD simulations agree with 1 ps decay times for a tetrahedrally coordinated water molecule [72]. Simulations by Starr calculate hydrogen bond lifetimes on the order of 1 ps with an Arrhenius type behavior [73]. Furthermore, depolarized light scattering experiments also find a similar lifetime [74].

5.2.4 Residual Fits

Once the background subtraction is done by fitting the reduced polarization to the known two Debye relaxations and four high frequency Lorentzians, the residuals are obtained. All five temperatures reveal oscillatory features not previously seen in the literature for D_2O. These residuals with their fits are shown in figure 5.7.

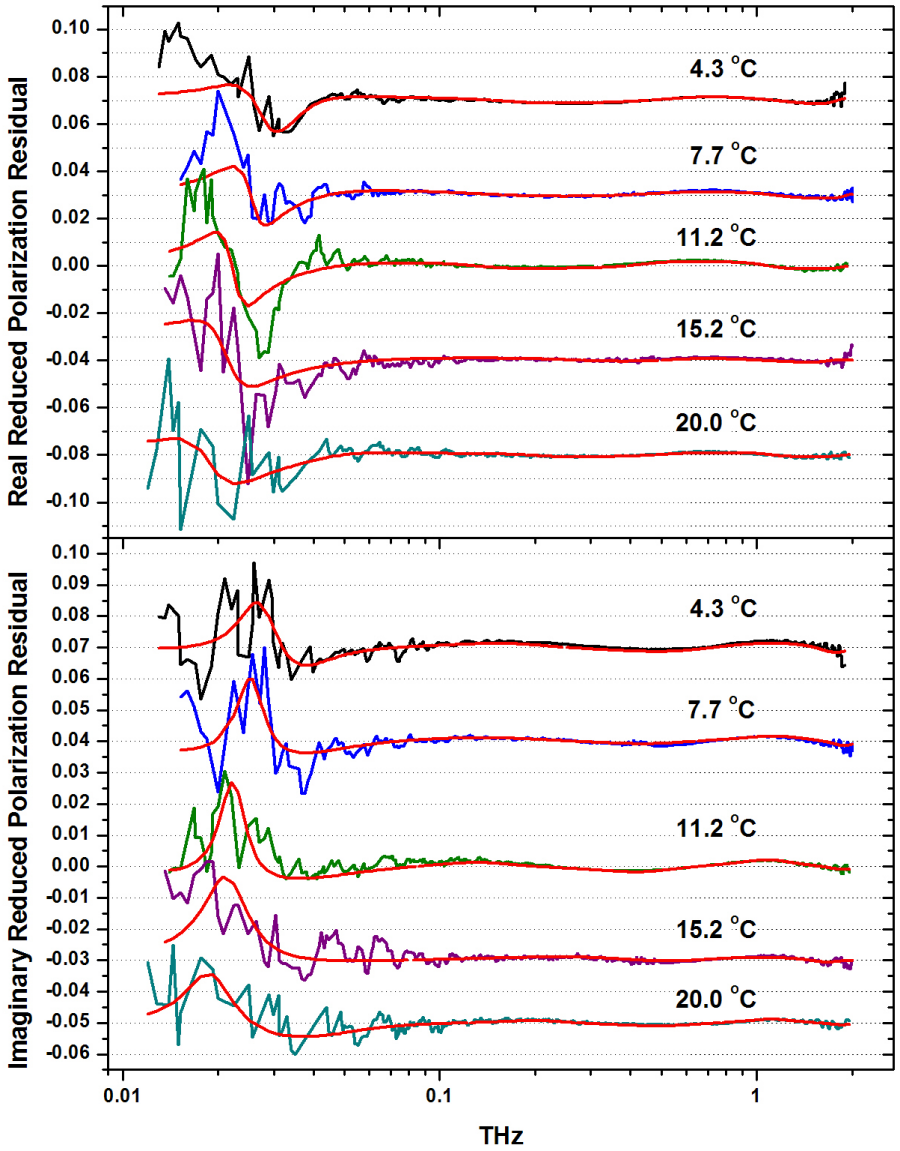

Figure 5.7 The D_2O reduced polarization residuals after the two Debye and four known Lorentzian background has been subtracted. 4.3 °C and 7.7 °C are shifted up, and 15.2 °C and 20.0 °C are shifted down from zero for clarity.

These residual features can only be fit by a sum of positive and negative Lorentzians. Their locations in the in the 20.0 ^{o}C residual spectrum are pointed out in figure 5.8. All of the temperatures exhibit six Lorentzians that are similar in location, amplitude and damping constant.

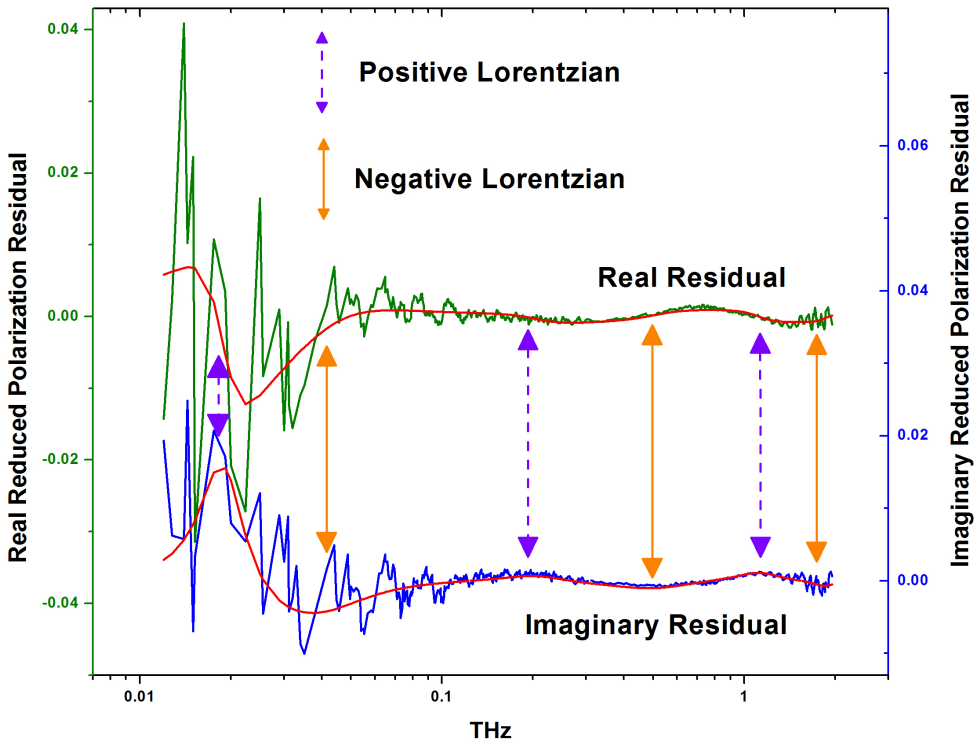

Figure 5.8 The locations of the positive and negative residual Lorentzians for 20.0 ^{o}C.

Table 5.3 lists the fit parameters for all five D_2O temperatures. They are grouped according to spectrum location and sign of the amplitude. The relative damping, explicitly expressed as $\Gamma/4\pi\nu$, is included as well. A value of 1 is a critically damped oscillator, less than one indicates an underdamped oscillator, and greater than one indicates an overdamped oscillator. It is important to note that since all of the Lorentzians are underdamped, they cannot be considered as relaxations.

Temp (^oC)	b_1	ν_1 (THz)	Γ_1 (ps^{-1})	Damping	b_2	ν_2	Γ_2	Damping
4.3	0.01047 (7E-5)	0.0275 (4E-5)	0.0684 (0.0007)	0.198 (0.002)	-0.01002 (6E-5)	0.0336 (7E-5)	0.149 (0.001)	0.354 (0.002)
7.7	0.0070 (0.0004)	0.0255 (0.0002)	0.041 (0.003)	0.127 (0.009)	-0.0088 (0.0004)	0.0335 (0.0005)	0.270 (0.011)	0.643 (0.028)
11.2	0.00745 (5E-5)	0.0223 (1E-5)	0.0323 (0.0002)	0.1150 (0.0007)	-0.00750 (6E-5)	0.0364 (0.0001)	0.341 (0.002)	0.746 (0.005)
15.2	0.0110 (0.0006)	0.0215 (0.0002)	0.054 (0.003)	0.200 (0.011)	-0.0016 (0.0003)	0.052 (0.002)	0.565 (0.034)	0.857 (0.062)
20.0	0.0081 (0.0005)	0.0191 (0.0003)	0.051 (0.004)	0.212 (0.017)	-0.0057 (0.0002)	0.0399 (0.0005)	0.286 (0.010)	0.571 (0.021)
	b_3	ν_3	Γ_3	Damping	b_4	ν_4	Γ_4	Damping
4.3	0.00149 (6E-6)	0.1754 (0.0004)	1.045 (0.006)	0.474 (0.003)	-0.00275 (5E-6)	0.6021 (0.0006)	4.090 (0.012)	0.541 (0.002)
7.7	0.00175 (4E-5)	0.169 (0.002)	1.395 (0.037)	0.669 (0.019)	-0.00100 (2E-5)	0.481 (0.003)	2.637 (0.045)	0.436 (0.008)
11.2	0.00127 (4E-6)	0.1392 (0.0001)	0.662 (0.002)	0.379 (0.001)	-0.00145 (3E-6)	0.4502 (0.0003)	2.056 (0.005)	0.363 (0.001)
15.2	0.00130 (3E-5)	0.304 (0.002)	2.205 (0.041)	0.578 (0.011)	-8.49E-4 (9E-6)	0.554 (0.002)	2.696 (0.030)	0.387 (0.005)
20.0	5.9E-4 (1E-5)	0.210 (0.001)	0.796 (0.021)	0.301 (0.008)	-8.9E-4 (1E-5)	0.531 (0.002)	2.622 (0.036)	0.393 (0.006)
	b_5	ν_5	Γ_5	Damping	b_6	ν_6	Γ_6	Damping
4.3	0.00285 (4E-6)	1.430 (0.002)	13.168 (0.040)	0.733 (0.002)	-9.04E-4 (3E-6)	1.783 (0.002)	3.434 (0.022)	0.153 (0.001)
7.7	0.00105 (5E-6)	1.188 (0.002)	4.514 (0.026)	0.302 (0.002)	-3.37E-4 (5E-6)	1.886 (0.004)	2.345 (0.051)	0.099 (0.002)
11.2	0.00113 (2E-6)	1.115 (0.001)	3.582 (0.012)	0.256 (0.001)	-2.80E-4 (2E-6)	1.869 (0.008)	2.759 (0.095)	0.117 (0.004)
15.2	0.00103 (6E-6)	1.156 (0.003)	7.183 (0.054)	0.494 (0.004)	-2.82E-4 (5E-6)	1.665 (0.006)	2.782 (0.072)	0.133 (0.003)
20.0	5.39E-4 (3E-6)	1.134 (0.002)	3.065 (0.020)	0.215 (0.001)	-1.74E-4 (4E-6)	1.853 (0.013)	2.634 (0.165)	0.113 (0.007)

Table 5.3 Residual Lorentzian fit parameters. Variances in the fit parameters and the uncertainty in the relative damping are given in parentheses.

The epsilon residuals are shown with errorbars for the five temperatures in figures 5.9 – 5.11. Their respective six Lorentzian fits are displayed as well to exhibit their accuracy in relation to the measurement error.

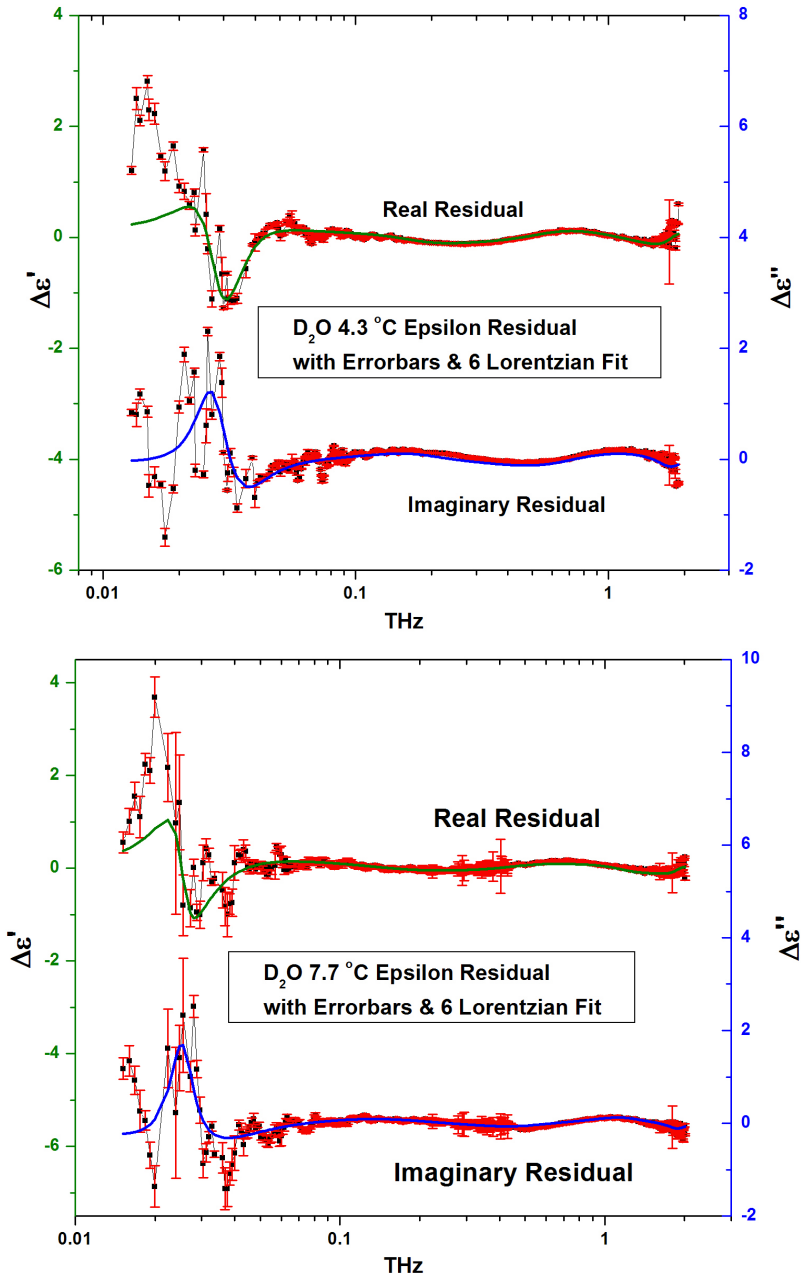

Figure 5.9 Epsilon residuals with errorbars and Lorentzian fits for 4.3 °C and 7.7 °C.

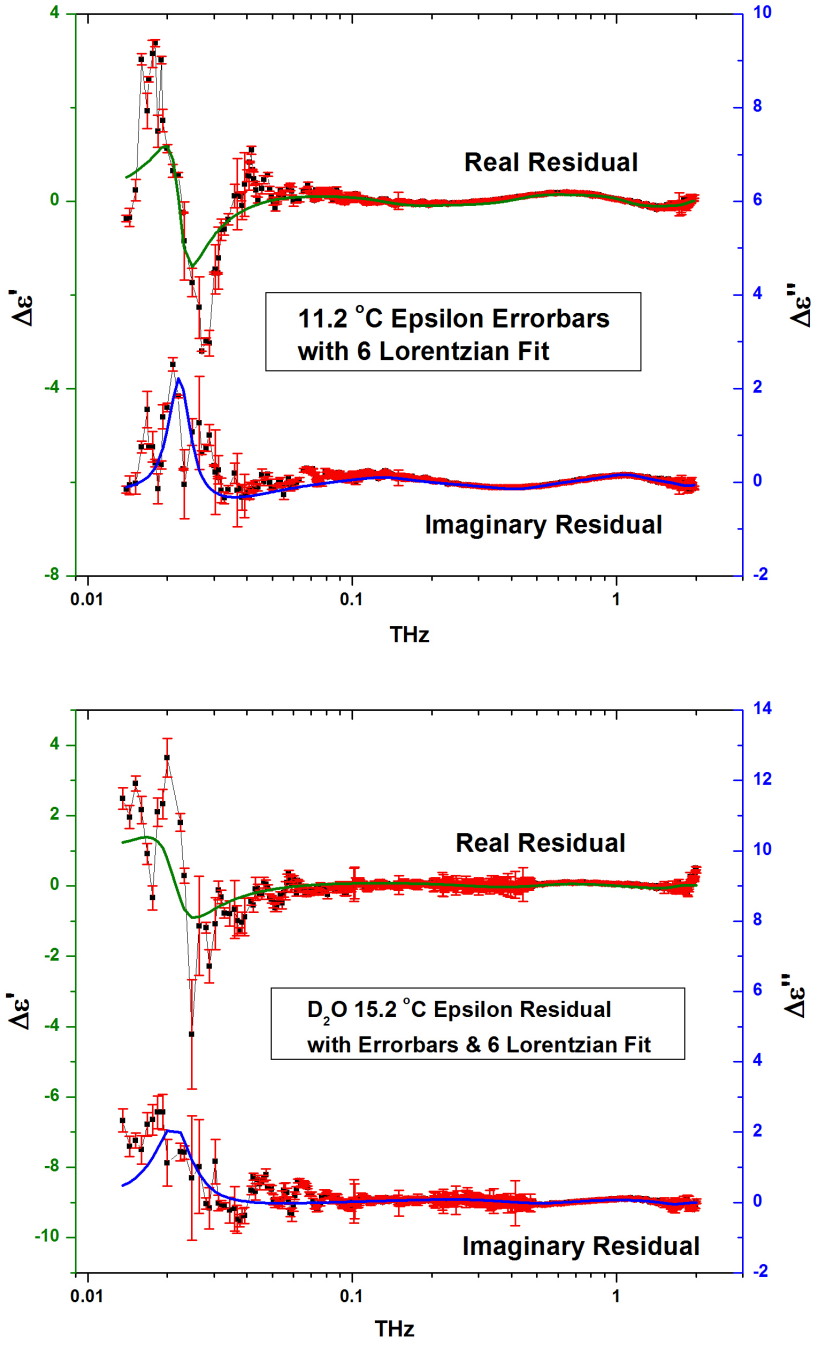

Figure 5.10 Epsilon residuals with errorbars and Lorentzian fits for 11.2 °C and 15.2 °C.

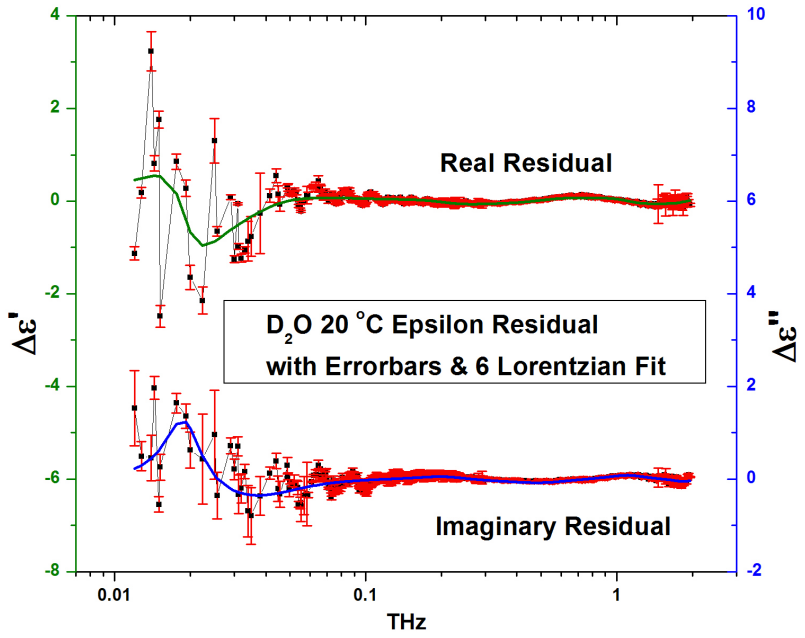

Figure 5.11 Epsilon residuals with errorbars and Lorentzian fits for 20.0 °C.

The orientational effects that lead to negative Lorentzians have been measured in the vibrational sum frequency spectra of water molecules at the air-water and CCl_4-water interfaces. Brown, et al., attribute these negative oscillation amplitudes to the water molecule pointing its hydrogen atoms either towards or away from the interface [75]. However, the current work provides the first observation of anti-correlated effects in bulk D_2O, and confirms previously obtained results from our group that discovered this same phenomenon in bulk H_2O [49].

Negative Lorentzians in bulk water are a possible signature of dipole-dipole interactions amongst counter-aligned molecules. Mathias and Tavan performed MD simulations that calculated the dipole-dipole correlation function with respect to the azimuthal angle of a central dipole [76]. Their results, shown in figure 5.12, find that

there are two regions of correlation, namely an axial and an equatorial region, divided along the angle $\varphi = \pm 55^{o}$. The dipoles in the axial regions are aligned with the central dipole and their correlation strengths are shown by the varying shades of red. Dipoles located in the equatorial region are on average counter-aligned, and the strength of their anti-correlation is depicted by shades of blue. The correlations persist over 60 Å from the central dipole in the axial direction and nearly 50 Å in the equatorial direction. The oscillatory features we observe in the residuals could be related to these weak long distance correlations.

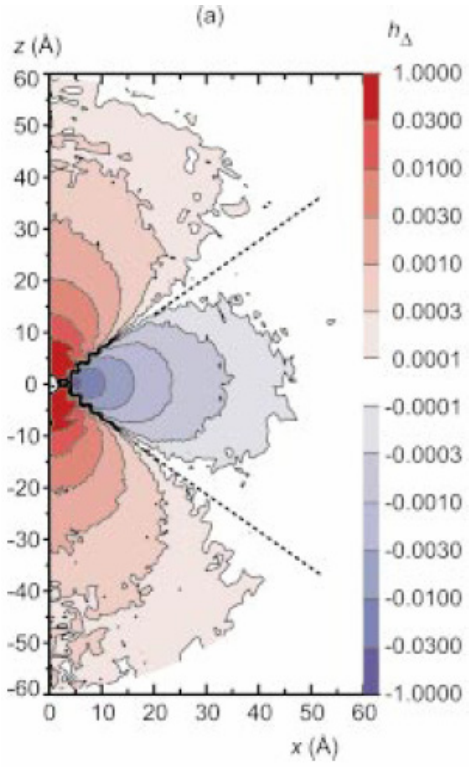

Figure 5.12 Mathais & Tavan MD simulation of the dipole-dipole correlation function h_Δ as a function of the azimuth angle and distance from central dipole [76].

5.3 The Low Frequency Oscillator

It is easily apparent from figure 5.7 that the D_2O residuals for all the temperatures exhibit a prominent low frequency feature. This oscillation stands out from the other Lorentzians in that it is highly underdamped and possesses an amplitude that is rather large in comparison. Inspection of the fit parameters in table 5.3 reveals the general trend towards higher damping as the oscillator center frequency decreases, with the obvious exception being that of the lowest frequency oscillator. In fact, when compared to the next two features, it is four times less damped than the 50 GHz oscillator and three times less damped than the 200 GHz oscillator.

Another interesting fact is that the relative damping of this feature is a minimum at 11.2 ^{o}C, the temperature of maximum density, and then is increasingly damped as the temperature deviates farther away from this point. However, this behavior is atypical since nearly all other spectral features in water that exhibit a temperature dependence scale monotonically. To help illustrate the peculiar nature of this oscillation, figure 5.13 compares the temperature dependence of the D_2O density [77] to the temperature dependence of the quality factor of the oscillator (inverse of the relative damping). The errorbars for the quality factor indicate a 95% confidence level. In addition, figure 5.14 plots the relative damping as a function of D_2O density to further support the notion that this most interesting feature of the residual spectra could be intimately related to the density anomaly in D_2O. The errorbars in figure 5.14 indicate a 95% confidence level as well.

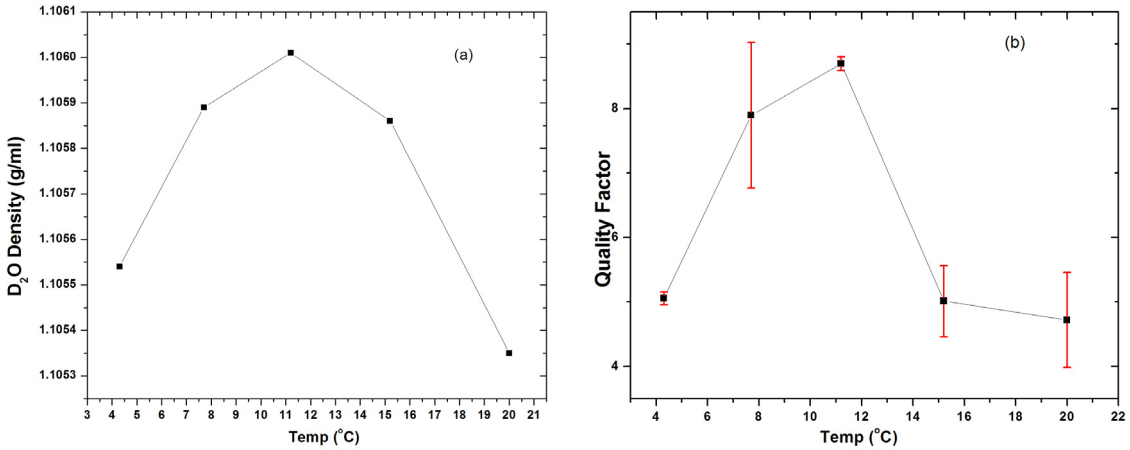

Figure 5.13 (a) D_2O density vs. temperature [77] and (b) the quality factor for the lowest frequency Lorentzian vs. temperature. Errorbars show a 95% confidence limit.

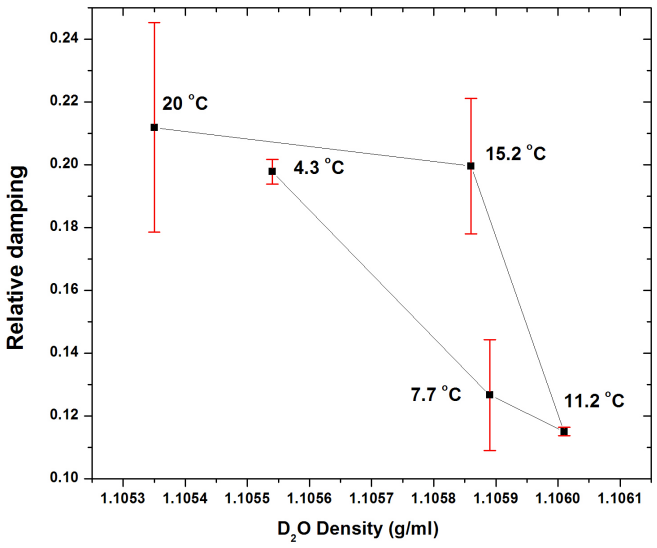

Figure 5.14 Relative damping as a function of D_2O density. Errorbars indicate a 95% confidence limit.

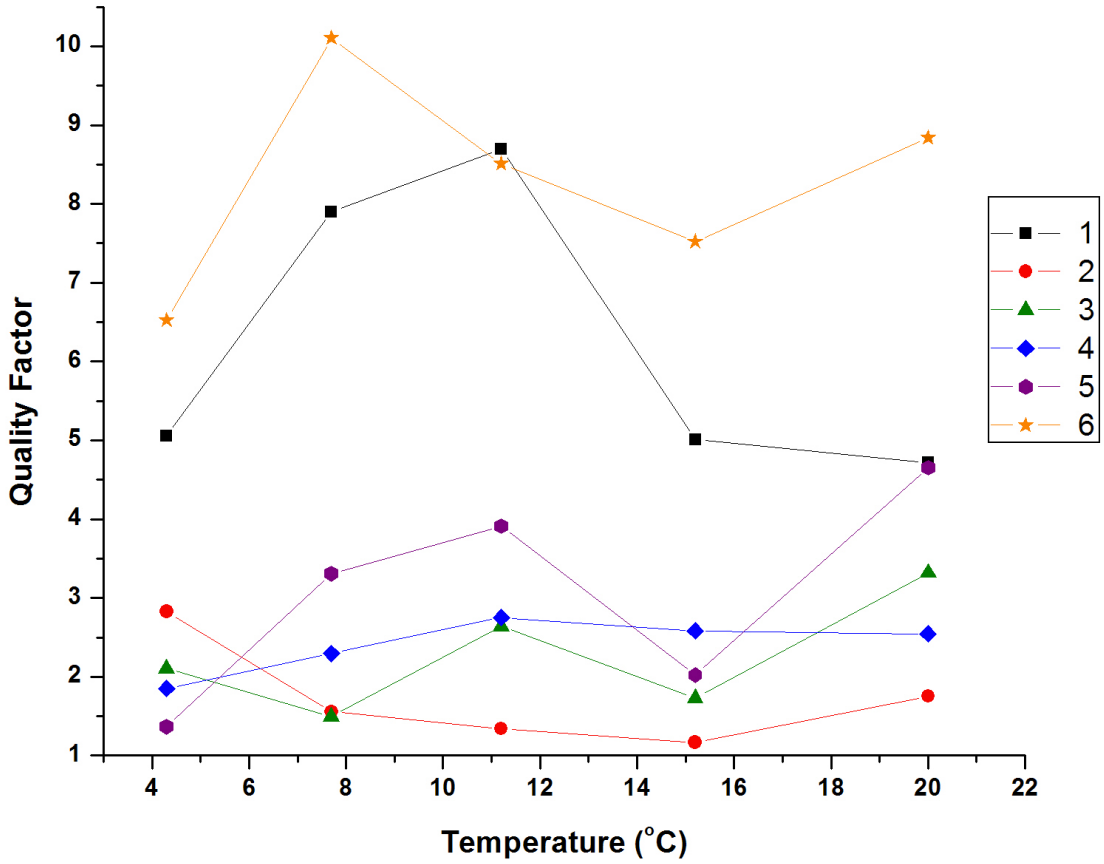

Figure 5.15 Quality factors as a function of temperature for all six residual Lorentzians. Lorentzians are index according to center frequency.

Finally, the quality factors of all the residual oscillators as a function of temperature are compared in figure 5.15. Here, the points are labeled according to the way they are indexed in table 5.3, with "1" being the lowest frequency Lorentzian and "6" being highest in frequency. This plot illustrates the overall trend of the Lorentzians becoming increasingly damped as the center frequency decreases, then a sudden jump in quality factor for Lorentzian 1. One can also see from this plot that Lorentzian 1 is the only feature to have a quality factor significantly peak at the maximum density, whereas all the other residual oscillators do not show this behavior.

5.4 Molecular Dynamics Simulations of Water

The MD simulations performed within our research group by Koji Yokoyama utilized the rigid and non-polarizable TIP5P model [78-79] to calculate the dynamics of H_2O molecules at 294.4 K and 1 atm. The TINKER program package was used to calculate the trajectories [80]. His simulations tracked 3456 water molecules in a 47 Å cubic cell with periodic boundary conditions to examine their collective motions on the time scale of tens of picoseconds. Electrostatic interactions were calculated with a particle-mesh Ewald summation and a simple truncation was used for Lennard-Jones type van der Waals interactions. Both of these forces had a real space cutoff of 15.0 Å. The system was integrated with a time step of 0.5 fs but was allowed to equilibrate for 50 ps before 150 ps trajectory data was recorded in 50 fs intervals [49, 81].

From the information generated by this simulation, the microscopic correlation was numerically calculated from the following approximation

$$\gamma_N(t) = \frac{<\mu_i(0)\cdot\sum_{j=i}^{N}\mu_i(t)>}{<\mu_i(0)\cdot\sum_{j=i}^{N}\mu_i(0)>} \cong \frac{\sum_{\tau=0}^{N_t\Delta\tau}\sum_{i=1}^{N_M}\left[\mu_i(\tau)\cdot\sum_{j=i}^{N}\mu_j(\tau+t)\right]}{\sum_{\tau=0}^{N_t\Delta\tau}\sum_{i=1}^{N_M}\left[\mu_i(\tau)\cdot\sum_{j=i}^{N}\mu_j(\tau)\right]} \tag{5.5}$$

The correlation function was for all N_M molecules in the ensemble from initial time τ to t = 50 ps. The initial time τ is shifted in steps of $\Delta\tau$ = 0.2 ps out to a final time $N_t\Delta\tau$ that satisfies $N_t\Delta\tau$ + t = 150 ps. At every time step, the correlation function is calculated to obtain over 1.7 million ensembles in the determination of $\gamma_N(t)$. Here, N is the number of molecules within the sphere that defines the microscopic correlation function.

Due to the periodic boundary conditions imposed on the finite size of the MD simulation, distances greater than half the 47 Å cube length were found to cause artifacts in the calculation of $\gamma_N(t)$. Thus, calculations were limited to a correlation function of $\gamma_{500}(t)$ despite the results from figure 5.12 that show dipole correlations persisting past 50 Å.

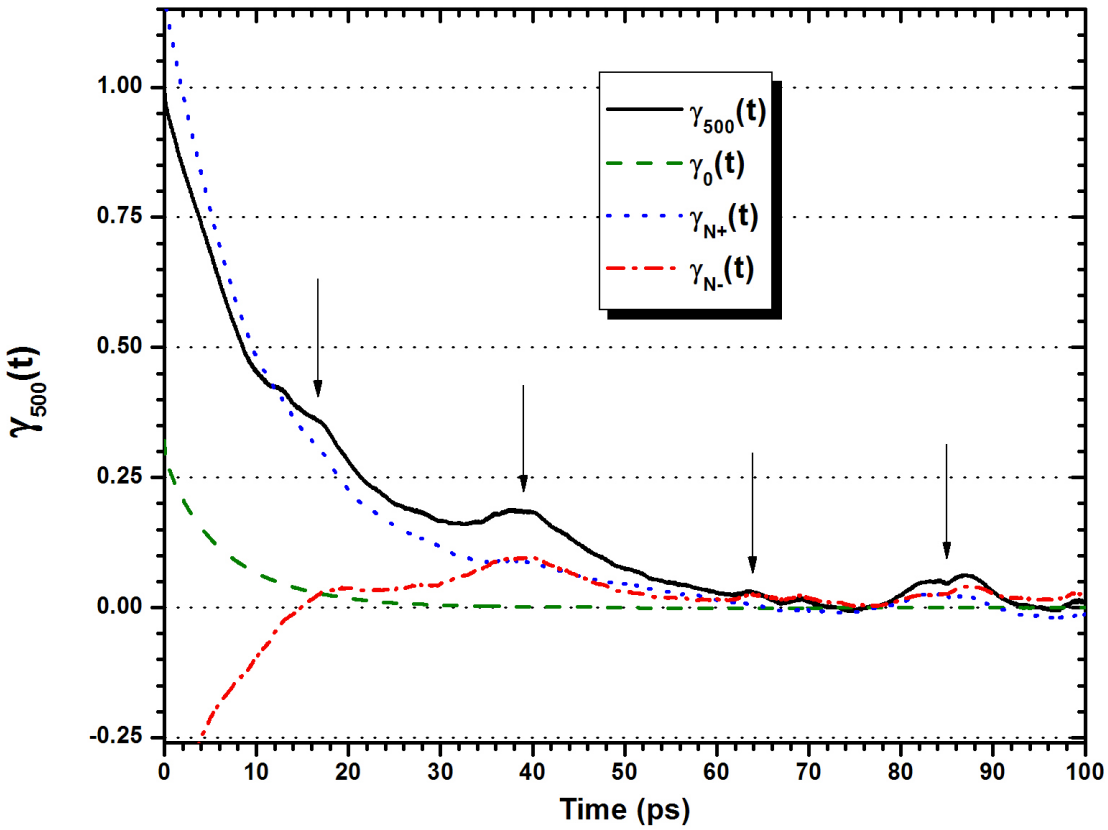

Figure 5.16 Dipole-dipole correlation function calculated for 500 molecules. The total function is broken down into the autocorrelation, and the correlation functions for regions of net positive and negative correlation. The arrows point to times of correlation reemergence.

However, the calculation of $\gamma_{500}(t)$ out to 100 ps yields some notable results and is illustrated in figure 5.15. From this graph, it is evident that correlation restores in approximately 20 ps intervals. For further analysis, the correlation function was broken

up into three parts: the autocorrelation function, the correlation associated with regions of net positive correlation, and the correlation of regions with net negative correlations. The regions of net negative and net positive correlations are denoted by $\gamma_{N-}(t)$ and $\gamma_{N+}(t)$, respectively. Figure 5.15 reveals that the autocorrelation function $\gamma_0(t)$ exhibits a simple relaxation, and the restoration of correlation in $\gamma_{500}(t)$ stems from $\gamma_{N-}(t)$ and $\gamma_{N+}(t)$. These regions are synchronized and have similar amplitudes. Strangely enough, $\gamma_{N-}(t)$ starts off anti-correlated, but after 15 ps, the molecules cross over to be positively correlated and for the most part remain positive.

The behaviors of $\gamma_{N-}(t)$ and $\gamma_{N+}(t)$ can be further interrogated by decomposing them into the time correlation functions of the individual solvation shells. By counting all the molecules inside the minima of the O-O pair distribution function from x-ray diffraction [6, 82], the number of molecules in each solvation shell can be determined. From the literature, the first shell includes all molecules within 3.4 Å, the second shell between the first and second minima is centered at 5.6 Å, and the third shell is at 7.9 Å.

The correlation functions of the solvation shells are shown in figure 5.16. It is revealed that the 4th and farther shells make a markedly higher contribution to both the $\gamma_{N-}(t)$ and the $\gamma_{N+}(t)$ than the first three. This can probably be attributed to the higher number of molecules residing in the outer shells. Also important to take notice of is the positively correlated first shell in the region of negative correlation. This indicates that the dominant interaction in the first shell may not be dipole-dipole, but is most likely the

hydrogen bond, where dipoles prefer to be co-aligned with their nearest neighbors. The abrupt crossing over of the second shell may also be due to this effect.

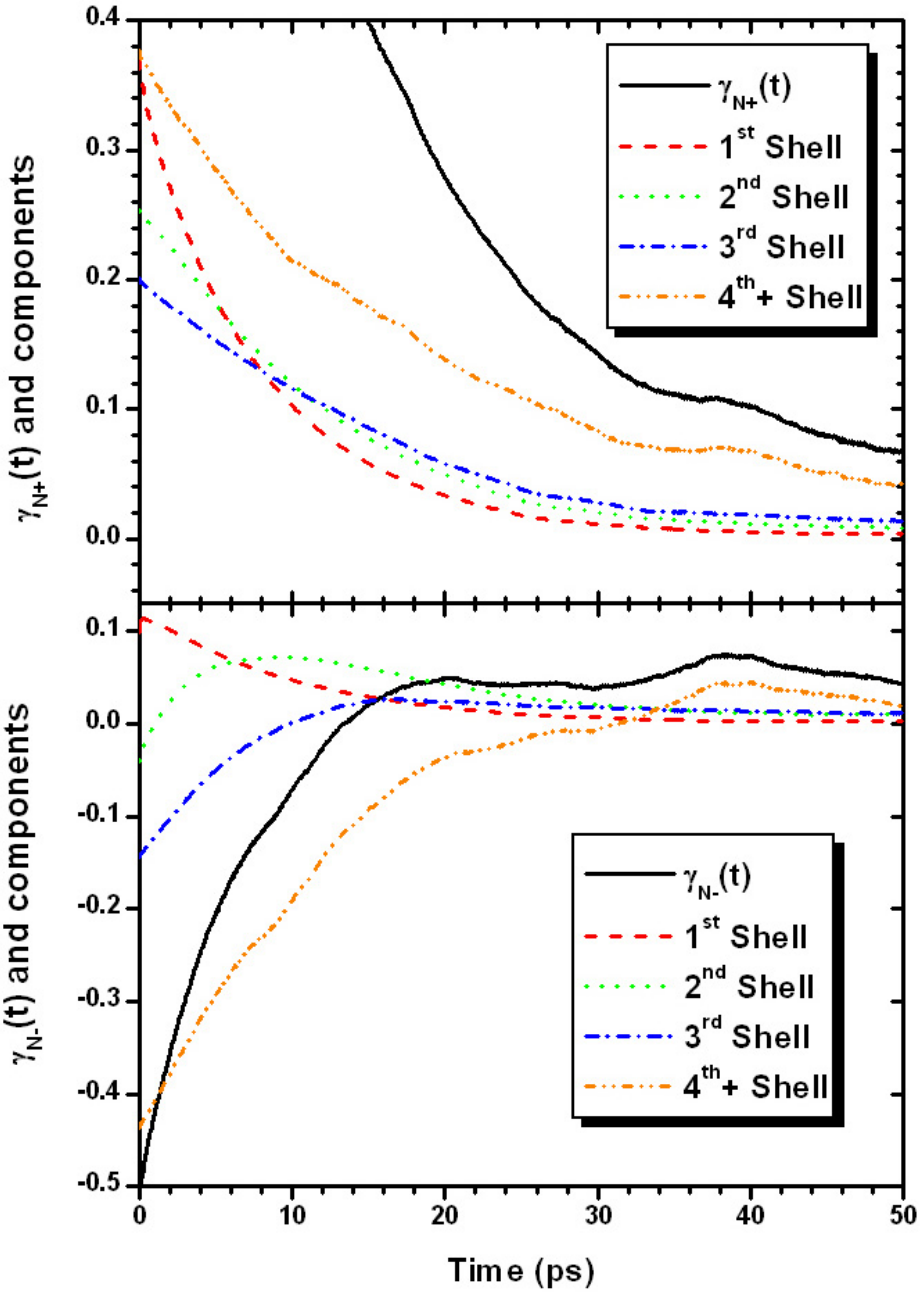

Figure 5.17 The correlation functions $\gamma_{N+}(t)$ and $\gamma_{N-}(t)$ decomposed into solvation shell constituents.

5.6 Comparison of D_2O to H_2O

The necessary comparison between H_2O and D_2O in order to gain greater insight into the nature of water on a molecular level is the major motivation of this work. The substitution of hydrogen with deuterium not only increases the mass by 11%, but also increases the temperature of maximum density from 4 ^oC to 11.2 ^oC and shifts the freezing point from 0 ^oC to 3.8 ^oC [77]. However, some properties of liquid water, such as the static dielectric constant, do not distinguish between molecular species.

Despite the fact that the static dielectric constant is the same between the two isotopes, the complex permittivity at every frequency is lower for D_2O when compared to H_2O at the same temperature. This difference arises due to the isotope shift of the primary relaxation time: 12.162 ps for heavy water versus 9.453 ps ordinary water [49]. The D_2O permittivity is compared to H_2O from McNary's THz data and is shown for 20 ^oC in figure 5.17.

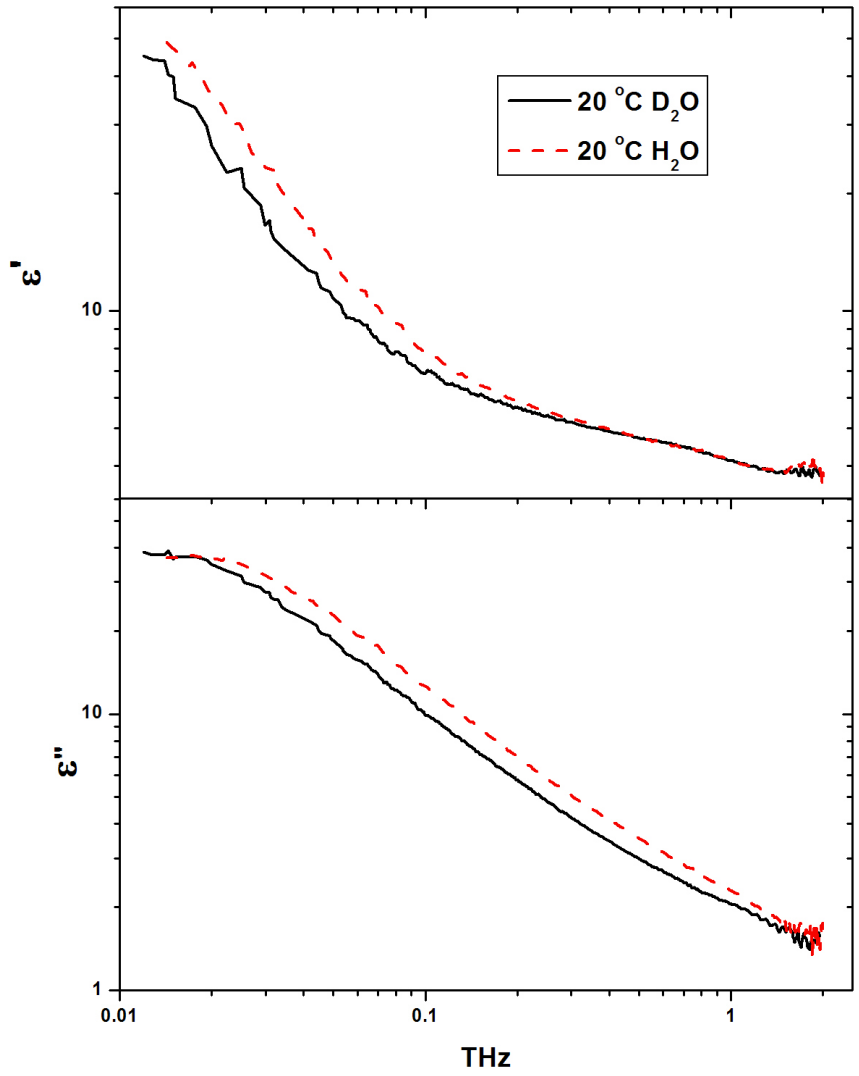

Figure 5.18 D_2O & H_2O [49] dielectric spectra at 20 °C

It is generally accepted that the primary relaxation is a relaxation of the liquid structure. This arises from the temperature dependence of the primary relaxation scaling with viscosity. Because of this, the temperature dependence of the primary relaxation should also scale with respect to other properties of the liquid structure, i.e. density. Since the temperature of maximum density is shifted by 7.2 °C between the two isotopes,

the temperature dependence for the primary relaxation in D_2O should be shifted by the same amount. Rønne, Åstrand, and Keiding [16] observed this in their THz work on water and heavy water. Figure 5.18 is a plot of the primary relaxations for D_2O measured at temperatures T shifted by $T - 7.2\,^{o}C$, and compared to McNary's H_2O data [49]. The errorbars show a 95% confidence level.

However, there is apparently no observed isotope shift for the second relaxation in D_2O. An absence of the shift in the secondary relaxation is most likely due to the idea that it is associated with the breaking of hydrogen bonds, as opposed to the relaxation of the liquid structure as a whole. Figure 5.19 compares the secondary relaxation times as a function of temperature between H_2O and D_2O. Since the deuterium bond is effectively stronger than the hydrogen bond due to the increased mass of the D_2O molecule, this can account for the longer secondary relaxation times.

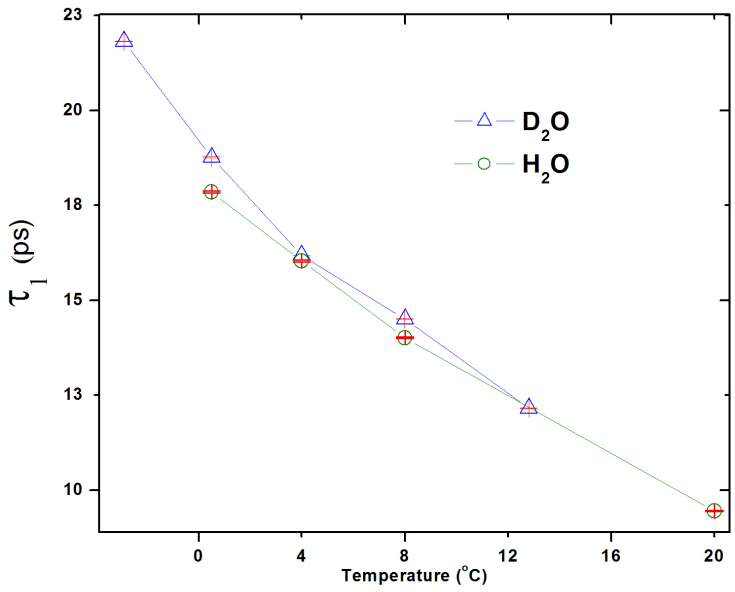

Figure 5.19 D_2O and H_2O [49] primary relaxations as a function of temperature. D_2O points are shifted down in temperature by 7.2 °C. Errorbars indicate a 95% confidence level.

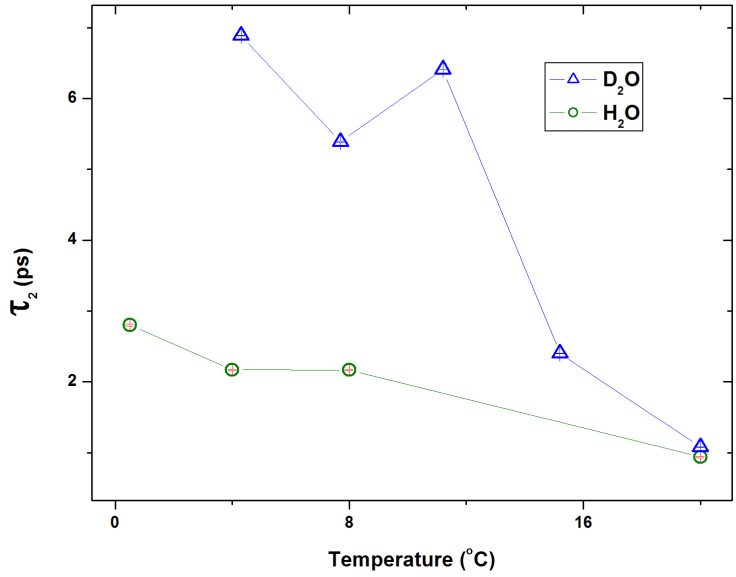

Figure 5.20 D_2O and H_2O [49] secondary relaxations as a function of temperature.

The epsilon residuals for heavy water are strikingly similar with that of McNary's water residuals. Every feature in heavy water has an isotopic analog that is comparable in amplitude and relative damping. In addition, the fact that the locations of positive and negative Lorentzians in the spectra are identical between the two species is interesting as well. Figures 5.21-5.23 illustrate the similarities of the residual Lorentzians by comparing D_2O to its structural analog in H_2O: 7.7 ^oC D_2O to 0.5 ^oC H_2O, 11.2 ^oC D_2O to 4 ^oC H_2O, and 15.2 ^oC D_2O to 8 ^oC H_2O. The yellow and purple arrows indicate the locations of negative and positive Lorentzians, respectively.

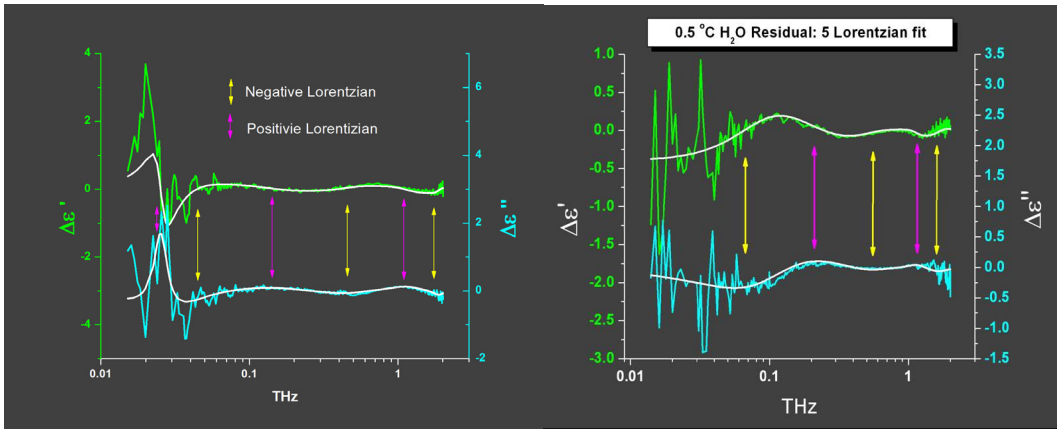

Figure 5.21 7.7 °C D_2O residual (left) compared to McNary's 0.5 °C H_2O residual (right) [49].

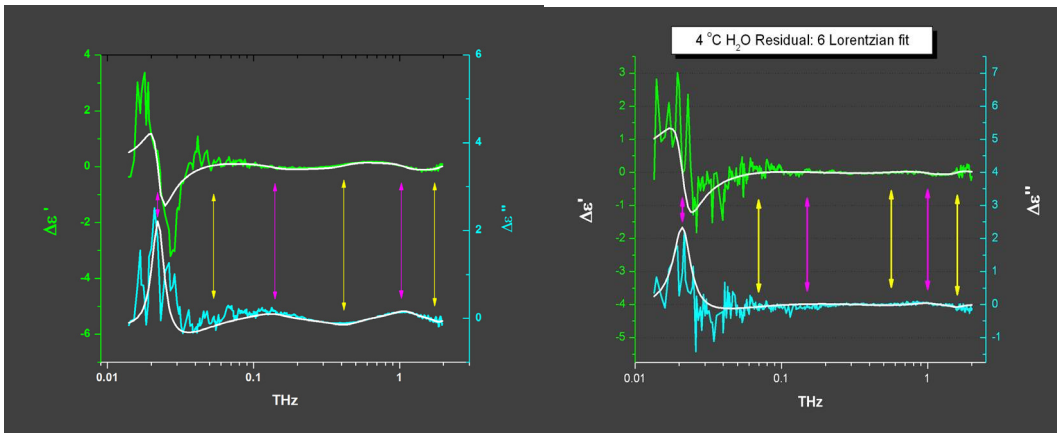

Figure 5.22 11.2 °C D_2O residual (left) compared to McNary's 4 °C H_2O residual (right) [49].

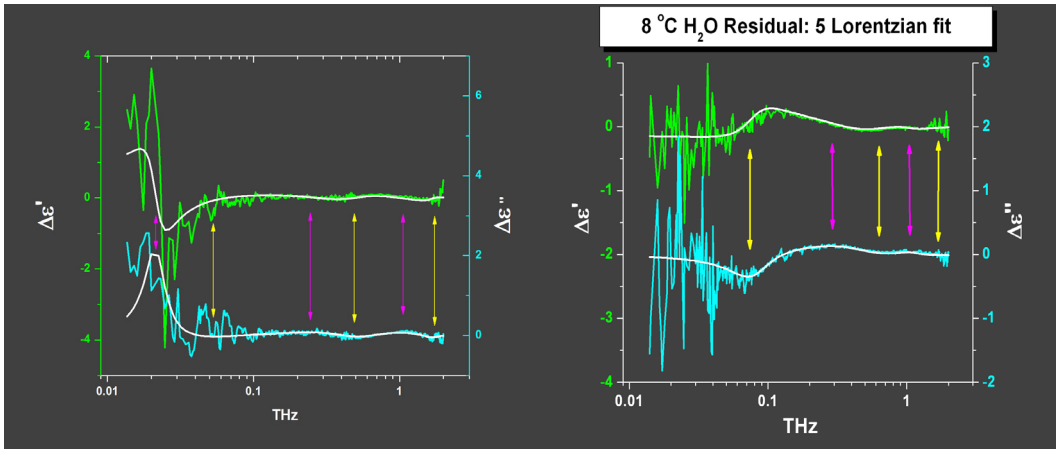

Figure 5.23 15.2 °C D_2O residual (left) compared to McNary's 8 °C H_2O residual (right) [49].

One can easily notice from figures 5.21-5.23 that a 21 GHz feature was found for 4 ^{o}C H_2O; analogous to the one at 22 GHz for 11.2 ^{o}C D_2O. However, this feature quickly disappears from the spectra at the other H_2O temperatures, where as in D_2O the oscillation persists over a broad temperature range.

Figure 5.24 displays the onset of this feature in H_2O at 3.5 ^{o}C and 4.5 ^{o}C, and table 5.5 provides the fitting parameters [49]. We see here that the damping at 3.5 ^{o}C and 4.5 ^{o}C in H_2O is comparable to the damping at 4.3 ^{o}C and 20 ^{o}C in D_2O. Additional data for H_2O at 3 ^{o}C and 5 ^{o}C were taken, but those residuals showed that the oscillation had already vanished [83].

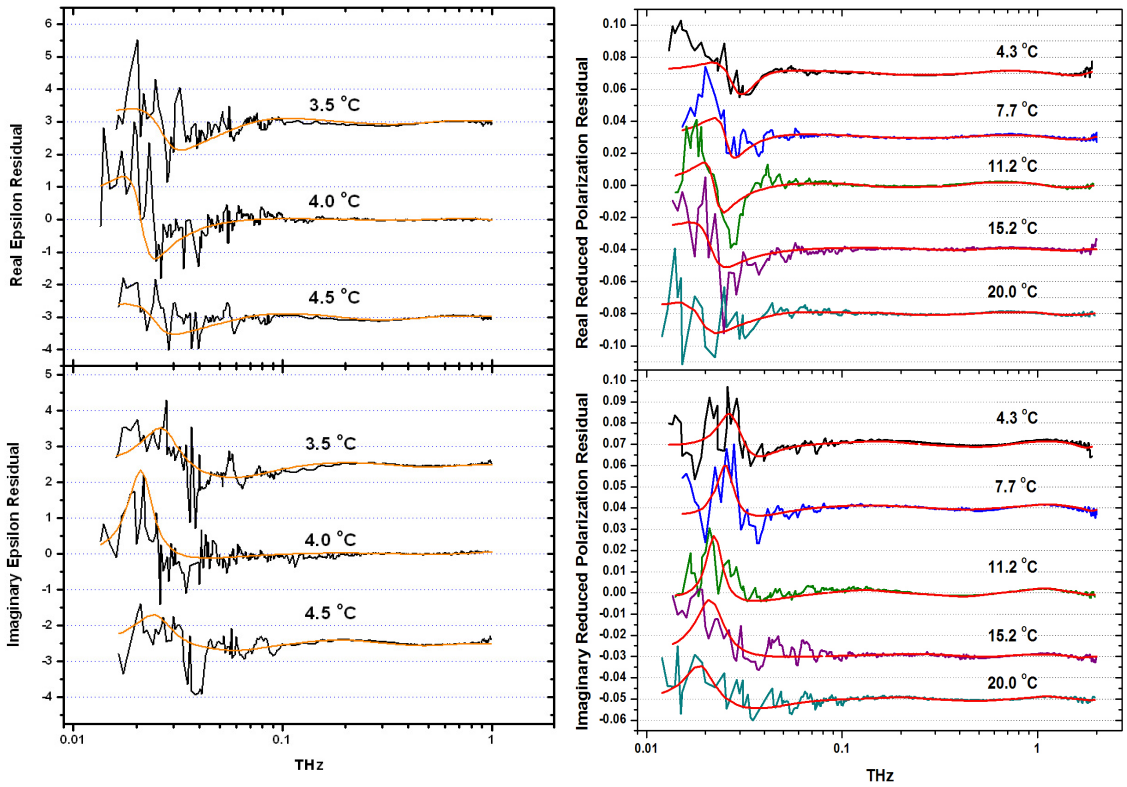

Figure 5.24 Left: Epsilon residuals for 3.5, 4.0, and 4.5 ^{o}C H_2O showing the increased damping of the 21 GHz peak [49]. Right: D_2O residuals.

Temp (^oC)	b_1	ν_1 (THz)	Γ_1 (ps^{-1})	Damping	b_2	ν_2 (THz)	Γ_2 (ps^{-1})	Damping
3.5	0.00763 (0.0004)	0.027 (4E-4)	0.088 (0.005)	0.259 (0.019)	-0.0064 (0.0004)	0.068 (0.002)	0.563 (0.035)	0.659 (0.092)
4.0	0.01015 (0.0003)	0.021 (1E-4)	0.045 (0.002)	0.171 (0.008)	-0.0077 (0.0003)	0.070 (0.001)	1.230 (0.048)	1.398 (0.075)
4.5	0.00527 (0.0006)	0.025 (5E-4)	0.079 (0.007)	0.251 (0.027)	-0.0030 (0.0003)	0.067 (0.002)	0.473 (0.034)	0.562 (0.101)
	b_3	ν_3 (THz)	Γ_3 (ps^{-1})	Damping	b_4	ν_4 (THz)	Γ_4 (ps^{-1})	Damping
3.5	0.0022 (0.0001)	0.329 (0.010)	3.814 (0.280)	0.923 (0.104)	-0.0015 (7E-5)	0.518 (0.009)	3.281 (0.166)	0.504 (0.034)
4.0	0.0036 (0.0001)	0.149 (0.003)	2.812 (0.129)	1.502 (0.099)	-3.16E-4 (2E-5)	0.549 (0.016)	2.807 (0.250)	0.407 (0.048)
4.5	0.0013 (0.0002)	0.212 (0.006)	1.248 (0.099)	0.468 (0.050)	-6.36E-4 (8E-5)	0.498 (0.017)	2.212 (0.247)	0.353 (0.051)

Table 5.4 Fit parameters for 3.5 ^oC and 4.5 ^oC in comparison with 4 ^oC H_2O [49].

As previously discussed in section 5.3, the quality factor of the 20 GHz oscillator in D_2O shows a similar temperature dependence to that of the density. This same effect was also seen in H_2O, but differs from D_2O in that the damping happens much more strongly at temperatures close to the maximum density.

The results on D_2O are consistent with the known isotopes shifts that have been observed in the literature: a lower dielectric spectrum, and the primary relaxation temperature dependence shift of $T - 7.2\,^oC$. In addition, the many similarities in the residuals that are shared between water and heavy water provide compelling evidence that the same mechanisms that govern water dynamics are also the ones that are within D_2O.

Chapter 6 Conclusions

Utilizing time domain THz spectroscopy, the permittivity spectra of D_2O have been measured between 15 GHz and 2 THz. This was done for five temperatures: 4.3, 7.7, 11.2, 15.2, and 20.0 ^oC. The accuracy in these measurements is better than 1% over most of the frequency range.

We show that the reduced polarization formula, calculated by Fattuzo and Mason, relates the microscopic correlation function to the macroscopic complex permittivity in a manner appropriate for polar liquids. With this correction, we accurately model the dynamics of water molecules as a sum of Debye relaxations and Lorentzian oscillators.

To obtain the most accurate fit values possible, we include all of the higher frequency spectral features observed in the far IR. It has been shown that the tails of the 5, 13, and 16 THz features contribute substantially to the total dielectric spectrum in our frequency range, and can greatly affect the values for ε_∞ and the secondary Debye relaxation. In addition, the microwave measurements were used to set the values for the spectral range below 15 GHz to accurately determine the primary Debye relaxation. We then fit this wide frequency range of 0.8 GHz to 18 THz to the known 2 Debye relaxations and 4 Lorentzian oscillators.

The D_2O data of the current work shows excellent agreement with the main Debye relaxation measured the microwave literature data. In addition, we observed the isotope shift in the primary relaxation when the D_2O values were compared to the H_2O

studies previously performed in our group by McNary. Heavy water also shows slower times for the secondary relaxation in relation to ordinary water. We attribute this to the more structured nature of the deuterium bond over the hydrogen bond.

The residuals for D_2O were fit to six Lorentzians previously undetected in the literature. These residuals exhibit either positive or negative amplitude, and are attributed to positive or negative dipole-dipole correlations, respectively. This is confirmed by MD simulations performed by Mathias and Tavan, and MD simulations performed within our own group. These simulations show two regions of net positive and net negative correlation with respect to a central dipole. These correlations were shown to persist for distances up to 60 Å in the axial direction and 50 Å in the equatorial direction. In addition, the residual features are very similar to the ones observed in H_2O, and provide further proof for the existence of anti-correlated dipole dynamics. This strongly suggests that the same processes governing ordinary water are the same in heavy water.

However, the most interesting of the residual feature is the 20 GHz oscillator. We have shown that it is very different from the rest of the residual features in that the temperature dependence of the oscillator damping is strikingly similar to that of the density of water. Generally, features in water scale monotonically with temperature, thus the behavior of the 20 GHz oscillator is atypical. Previous studies on H_2O show a similar result; however the feature only persists within a much smaller temperature range between 3.5 and 4.5 ^{o}C, compared to D_2O where the oscillator remains at 0.5 ^{o}C and 20 ^{o}C. Thus, this peculiar feature may be intimately related to the density anomaly of water.

From these measurements, we have attained insight into the nature and structure of water on a molecular level never before achieved. Proof for the existence of anti-correlated effects and the observation of a new oscillation linked to the density anomaly in both D_2O and H_2O will greatly affect the way water is studied in the future. Also, this work provides a solid foundation to perform spectroscopic experiments on the much more complicated problem of biological molecules in aqueous solution.

Bibliography

[1] Martin Chaplin. *Forty-one anomalies of water.* 2 July 2004. 27 Sep. 2004. <http://www.lsbu.ac.uk/water/anmlies.html >.

[2] S.Woutersen, U. Emmerichs, H-K. Nienhuys, and H.J. Bakker, Phys. Rev. Lett. **81**, 1106 (1998).

[3] J. B. Hasted, *Aqueous Dielectrics* (Chapman and Hall, 1973).

[4] J. K. Gregory, *et al.*, Science **275**, 814 (1997).

[5] F. Franks, Ed., *Water: A Comprehensive Treaty. Volume 1: The Physics and Physical Chemistry of Water* (Plenum, New York, 1972).

[6] J. M. Sorenson, G. Hura, R. M. Glaeser, T. Head-Gordon, J. Chem. Phys. **87**, 9149 (2000).

[7] Ph. Wernet, *et al.*, Science **304**, 995 (2004).

[8] Martin Chaplin. *Hydrogen bonding in water.* 15 Oct. 2004. 17 Oct. 2004. <http://www.lsbu.ac.uk/water/hbond.html>.

[9] Swain & Bader, Tetrahedron **10**, 182 (1960).

[10] Felix Franks, *Water* (Royal Society of Chemistry, 1983).

[11] C. J. F. Böttcher and P. Bordewijk, *Theory of Electric Polarization* (Elsevier Scientific, 1978).

[12] D. D. Klug, D. E. Kranbuehl, and W. E. Vaughan, J. Chem. Phys. **50**, 3904 (1969).

[13] P. Debye, *Polar Molecules* (Dover 1929).

[14] J. T. Kindt and C. A. Schmuttenmaer, J. Phys. Chem. **100**, 10373 (1996).

[15] C. Rønne, *et al.*, J. Chem. Phys. **107**, 5319 (1997).

[16] C. Rønne, P.-O. Åstrand, and S. R. Keiding, Phys. Rev. Lett. **82**, 2888 (1999).

[17] C. Rønne and S. R. Keiding, J. Mol. Liq. **101**, 199 (2002).

[18] M. L. T. Asaki, A. Redondo, T. A. Zawodzinski, and A. J. Taylor, J. Chem. Phys. **116**, 8469 (2002).

[19] F. Kremer, J. Non-Crystalline Solids **305**, 1 (2002).

[20] M. Walther, PhD Thesis, *Modern Spectroscopy on Biological Molecules: Structure and Bonding investigated by THz time-domain and transient phase-grating spectroscopy*, Albert-Ludwigs-Universität Freiburg im Breisgau, 2003.

[21] J. D. Jackson, *Classical Electrodynamics 2nd Edition* (John Wiley & Sons, 1975).

[22] J. R. Reitz, F. J. Milford, R. W. Christy, *Foundations of Electromagnetic Theory 3rd Edition* (Addison-Wesley Publishing Company, 1979).

[23] R. Buchner, J. Barthel, and J. Stauber, Chem. Phys. Lett. **306**, 57 (1999).

[24] J. Barthel, K. Bachhuber, R. Buchner, H. Hetzenauer, Chem. Phys. Lett. **165**, 369 (1990).

[25] M. N. Asfar and J. B. Hasted, Infrared Physics **18**, 835 (1978).

[26] J. B. Hasted, S. K. Husain, F. A. M. Frescura, and J. R. Birch, Infrared Phys. **27**, 11 (1987).

[27] J. B. Hasted, S. K. Husain, F. A. M. Frescura, and J. R. Birch, Chem. Phys. Lett. **118**, 622 (1985).

[28] D. H. Auston and P. R. Smith, Appl. Phys. Lett. **43**, 631 (1983).

[29] D. H. Auston, K. P. Cheung, and P. R. Smith, Appl. Phys. Lett. **45**, 284 (1984).

[30] U. Kaatze, R. Behrends, R. Pottel, J. Non-Crystalline Solids **305**, 19 (2002).

[31] C. Rønne, PhD Thesis, *Intermolecular Liquid Dynamics Studied by THz-Spectroscopy*, Aarhus University, 2000.

[32] U. Kaatze, Chem. Phys. Lett. **132**, 291 (1986).

[33] K. E. Mattar and H. A. Buckmaster, J. Phys. D: Appl. Phys. **23**, 1464 (1990).

[34] J. M. Allison and R. J. Sheppard, Meas. Sci. Technol. **2**, 975 (1990).

[35] J. M. Allison and R. J. Sheppard, Meas. Sci. Technol. **1**, 1093 (1990).

[36] U. Kaatze, Chem. Phys. Lett. **203**, 1 (1993).

[37] A. A. Asheko and K. E. Nemchenko, Jour. Mol. Liquids **105**, 295 (2003).

[38] J. G. McAvoy and H. A. Buckmaster, J. Phys. D: Appl. Phys. **16**, 2519 (1983).

[39] H. Zaghloul and H. A. Buckmaster, J. Phys. D: Appl. Phys. **18**, 2109 (1985).

[40] U. Kaatze, J. Chem. Eng. Data **34**, 371 (1989).

[41] P. S. Yastremskii, J. Struct. Chem. **12**, 532 (1971).

[42] H. R. Zelsmann, J. Mol. Structure **350**, 95 (1995).

[43] K. Sakai, *Terahertz Optoelectronics* (Springer, 2005).

[44] Y. Cai *et al.,* Appl. Phys. Lett. **71**, 2076 (1997).

[45] C. Ludwig and J. Kuhl, Appl. Phys. Lett. **69**, 1194 (1996).

[46] A. G. Markelz and E. G. Heilweil, Appl. Phys. Lett. **72**, 2229 (1998).

[47] G. Zhao *et al*., Phys. Med. Biol. **47**, 3699 (2002).

[48] Y. C. Shen, *et al*., Appl. Phys. Lett. **83**, 3117 (2003).

[49] A.J. McNary, PhD Thesis, *Terahertz Time Domain Spectroscopy of Polar Liquids*, University of California, Riverside, 2005.

[50] Q. Wu and X.-C. Zhang, Appl. Phys. Lett. **67**, 3523 (1995).

[51] Q. Wu and X.-C. Zhang, Appl. Phys. Lett. **68**, 1604 (1996).

[52] Q. Lu, M. Litz, and X.-C. Zhang, Appl. Phys. Lett. **68**, 2924 (1996).

[53] Y. Cai *et al*., Appl. Phys. Lett. **73**, 444 (1998).

[54] S. G. Park, M. R. Melloch, and A. M. Weiner, Appl. Phys. Lett. **73**, 3184 (1998).

[55] A. Yariv, *Quantum Electronics, 3rd Ed*. (Wiley Text Books, 1989).

[56] L. Duvillaret, F. Garet, and J.-L. Coutaz, Applied Optics **38**, 409 (1999).

[57] D. S. Venables and C. A. Schmuttenmaer, J. Chem. Phys. **108**, 4935 (1998).

[58] K. N. Woods and H. Wiedemann, Chem. Phys. Lett. **393**, 159 (2004).

[59] P. R. Mason, J. B. Hasted, and L. Moore, Adv. Mol. Relaxation Processes **6**, 217 (1974).

[60] N. R. V. Nightingale, S. Szwarnowski, R. J. Sheppard, and E. H. Grant, J. Phys. E: Sci. Instrum. **14**, 156 (1981).

[61] M.N. Afsar and J.B. Hasted, J Opt Soc Am **67**, 902 (1977).

[62] I. Ohmine and S. Saito, Acc. Chem. Res. **32**, 741 (1999).

[63] L. Thrane, R. H. Jacobsen, P. Uhd Jepsen, and S. R. Keiding, Chem. Phys. Lett. **240**, 330 (1995).

[64] M. Koch, *et al.*, **"THz spectroscopy on polar liquids"**, Proceedings of the International Conference on LASERS'98. Soc. Opt. & Quantum Electron. 1999, pp.225-31. McLean, VA, USA.

[65] Yada, Nagai, Tanaka, Chem. Phys. Lett. **473**, 279 (2009).

[66] Cho, Urquidi, Singh, & Robinson, J. Phys. Chem. B **103** (1991).

[67] N. Agmon, J. Phys. Chem. **100**, 1072 (1996).

[68] P. H. Poole, F. Sciortino, U. Essmann, and H. E. Stanley, Nature **360**, 324 (1992).

[69] P. H. Poole, *et al*., Phys. Rev. Lett. **73**, 1632 (1994).

[70] F. Sciortino, P. H. Poole, U. Essmann, and H. E. Stanley, Phys. Rev. E **55**, 727 (1997).

[71] S. Woutersen, U. Emmerichs, and H. J. Bakker, Science **278**, 658 (1997).

[72] I. M. Svishchev and A. Yu. Zassetsky, J. Chem. Phys. **112**, 1367 (2000).

[73] F. W. Starr, J. K. Nielsen, and H. E. Stanley, Phys. Rev. Lett. **82**, 2294 (1999).

[74] S.-H. Chen and J. Teixeira, Adv. Chem. Phys. **90**, 2786 (1985).

[75] M. G. Brown, *et al*., J. Phys. Chem A **104**, 10220 (2000).

[76] J. W. Ponder, TINKER, Version 3.9 (Washington University School of Medicine, St. Louis, Missouri, 2001).

[77] G. S. Kell, J. Chem. Eng. Data **12**, 66 (1967).

[78] M. W. Mahoney and W. L. Jorgensen, J. Chem. Phys. **112**, 8910 (2000).

[79] M. W. Mahoney and W .L. Jorgensen, J. Chem. Phys. **114**, 363 (2001).

[80] J. W. Ponder, TINKER, Version 3.9 (Washington University School of Medicine, St. Louis, Missouri, 2001).

[81] K. Yokoyama (unpublished).

[82] G. Corongiu and E. Clemente, J. Chem. Phys. **97**, 2030 (1992).

[83] A.J. McNary (unpublished).

[84] S. Namba, J. Opt. Soc. Am. **51**, 76 (1961).

[85] G. Gallot, *et al.*, Appl. Phys. Lett. **74**, 3450 (1999).

[86] M. Schall, H. Helm, and S. R. Keiding **"THz time-domain spectroscopy of electro-optic crystals"**, Catalog No. 98EX171, pp. 194-195, IEEE 6th International Conference on Terahertz Electronics (THz'98), September 2-3 1998, Leeds, United Kingdom.

[87] W. C. Martin and W. L. Wiese. *Atomic Spectroscopy. A Compendium of Basic Ideas, Notation, Data, and Formulas.* June 2003. 26 Jan. 2005. <http://physics.nist.gov/Pubs/AtSpec/index.html>.

[88] P. R. Bevington and D. K. Robinson, *Data Reduction and Error Analysis for the Physical Sciences Second Edition* (WCB/McGraw-Hill, 1992).

Appendix A

Calculation of THz power from the Transverse Electro-Optic effect and the Electro-Optic Properties of ZnTe.

Zincblende crystals, such as ZnTe, are $\bar{4}3m$ crystals, and their electro-optic tensor is expressed as

$$\begin{pmatrix} 0 & 0 & 0 \\ 0 & 0 & 0 \\ 0 & 0 & 0 \\ r_{41} & 0 & 0 \\ 0 & r_{41} & 0 \\ 0 & 0 & r_{41} \end{pmatrix} \tag{A.1}$$

In general, the birefringence of a crystal can be expressed by its index ellipsoid as

$$\frac{x^2}{n_x^2} + \frac{y^2}{n_y^2} + \frac{z^2}{n_z^2} = 1 \tag{A.2}$$

where n_x, n_y, and n_z are refractive indexes that correspond to the principal crystallographic axes [55]. Under normal circumstances $n_x = n_y = n_{z,} = n_0$, but under the influence of an external electric field, the index ellipsoid then becomes

$$\frac{x^2 + y^2 + z^2}{n_0^2} + 2r_{41}(E_x yz + E_y zx + E_z xy) = 1 \tag{A.3}$$

with E_x, E_y, and E_z being the components of the external field along the directions of the crystallographic axes [84].

Considering the situation of a ZnTe crystal that is cut along the (110) direction, a transformation from the lab to crystal frame yields $x' = \frac{1}{\sqrt{2}}(x+y)$, $y' = \frac{1}{\sqrt{2}}(x-y)$, and $z' = z$. If the direction of external electric field propagation is perpendicular to the (110) plane, then $E_{x'} = 0$ along the $x' =$ (110) direction. Plugging all of this into equation A.3 gives

$$\left(\frac{1}{n_0^2} + r_{41}E_{z'}\right)x'^2 + \left(\frac{1}{n_0^2} - r_{41}E_{z'}\right)y'^2 + \frac{z'^2}{n_0^2} - 2r_{41}E_{y'}y'z' = 1 \tag{A.4}$$

Thus, the index ellipsoid in the new frame yields the equations

$$\begin{aligned}
\frac{1}{n_{x'}^2} &= \frac{1}{n_0^2} + r_{41}E_{z'} \\
\frac{1}{n_{y'}^2} &= \frac{1}{n_0^2} - \frac{1}{2}\left(r_{41}E_{z'} + r_{41}\sqrt{E_{z'}^2 + 4E_{y'}^2}\right) \\
\frac{1}{n_{z'}^2} &= \frac{1}{n_0^2} - \frac{1}{2}\left(r_{41}E_{z'} - r_{41}\sqrt{E_{z'}^2 + 4E_{y'}^2}\right)
\end{aligned} \tag{A.5}$$

and using the approximation that $r_{41}E << n_0^{-2}$ along with the differential relationship

$$dn = -\left(\frac{n^3}{2}\right)d\left(\frac{1}{n}\right) \tag{A.6}$$

allows us to solve

$$\begin{aligned}
n_{x'} &= n_0 - \frac{n_0^3}{2}r_{41}E_{z'} \\
n_{y'} &= n_0 + \frac{n_0^3}{4}r_{41}\left(E_{z'} + \sqrt{E_{z'}^2 + 4E_{y'}^2}\right) \\
n_{z'} &= n_0 + \frac{n_0^3}{4}r_{41}\left(E_{z'} - \sqrt{E_{z'}^2 + 4E_{y'}^2}\right)
\end{aligned} \tag{A.7}$$

The retardation due to the field is given by

$$\Gamma = \phi_{y'} - \phi_{z'} = \frac{2\pi l}{\lambda}\left(n_{y'} - n_{z'}\right) \tag{A.8}$$

For a field where $E_{z'} = 0$, this term can be written as

$$\Gamma = \frac{2\pi l}{\lambda} n_0^3 r_{41} E_{y'} \tag{A.9}$$

Here the maximum rotation is felt by light coming in parallel to the applied field. The fractional energy rotated out of the initial polarization angle is given by

$$\frac{I}{I_0} = \sin^2 \frac{\Gamma}{2} \tag{A.10}$$

The picosecond field of the THz beam can be considered a static electric field in relation to the much shorter femtosecond probe beam just as long as the two pulses overlap in the crystal. ZnTe is an especially desirable material since it has a relatively With a fairly large electro-optic coefficient (r_{41} = 4.04 pm/V at 0.633 μm), and a low group velocity mismatch (GVM) of 1.1 ps/mm between the THz radiation and the probe beam, ZnTe is the ideal candidate for phase sensitive THz measurements [51]. However, crystal thicknesses in excess of several millimeters are usually avoided due to the GVM appreciating in significance [85-86]. In addition, the weak absorption band at 1.65 THz that ZnTe exhibits increases in strength for crystals of such thickness.

Appendix B

The relationship between frequency and wavenumber.

The photon energy to excite an electronic transition or a molecular vibrational or librational mode is written as

$$\Delta E = E_f - E_i = h\nu = hc\sigma = hc/\lambda \tag{B.1}$$

Here ν is the unit of frequency given in Hertz, σ is the wavenumber with SI units of m^{-1}, and λ is the wavelength of the photon emitted or absorbed. Since all these values are related by c, the speed of light, all are equally accurate in reporting the transition frequency [87]. Infrared spectroscopy generally measures absorption spectra and report data in units of cm^{-1}, where 1 cm^{-1} = 100 m^{-1}. The convention for experiments in the optical or microwave and below ranges, is to report their measurements in Hertz. This is the case in terahertz spectroscopies as well. Since ν and σ are merely related by the speed of light, c, one can easily convert between the two and find that 1 cm^{-1} = 2.99792458 x 10^{-2} THz.

Appendix C

Interpolated fit functions for frequencies outside of the measurement range.

In order to fully subtract the background and obtain accurate residuals, data from the literature was joined with the D_2O dielectric spectra measurements. For low frequencies outside our bandwidth, namely 15 GHz, epsilon was set with Yastremskii's microwave data [41]. On the high frequency end, Zelsmann's FIR data [42] was appended for frequencies higher than 2 THz. These data sets were chosen for their agreement with other published data, their comprehensive temperature dependence study, and range of frequencies.

C.1 Interpolation of microwave data

Employing a waveguide at 9.37 GHz, the microwave data collected by Yastremskii measured the permittivity for both water and heavy water at five degree intervals between 5 ^{o}C and 40 ^{o}C as well as at 50 and 60 ^{o}C [41]. Also reported are the relaxation times for both H_2O and D_2O at these temperatures.

These relaxation times for D_2O, denoted by τ_D, are displayed in figure C.1(a). They were found to have a temperature dependence and, following the procedure outlined by Ronne, Astrand, and Keiding [16], are shown in the Angell plot of $\ln \tau_D$ versus $-\ln\left(T/T_S - 1\right)$ where $T_S = 235.2\,K$. This is illustrated in figure C.1(b). The linear

fit of the Angell plot produces the equation by which the relaxation times are interpolated, and is expressed as

$$\tau_D = Exp\left[0.07805 + 1.7237\left(-\ln\left(\frac{T}{T_S} - 1\right)\right)\right] \tag{C.1}$$

where T in this case is temperature in Kelvin.

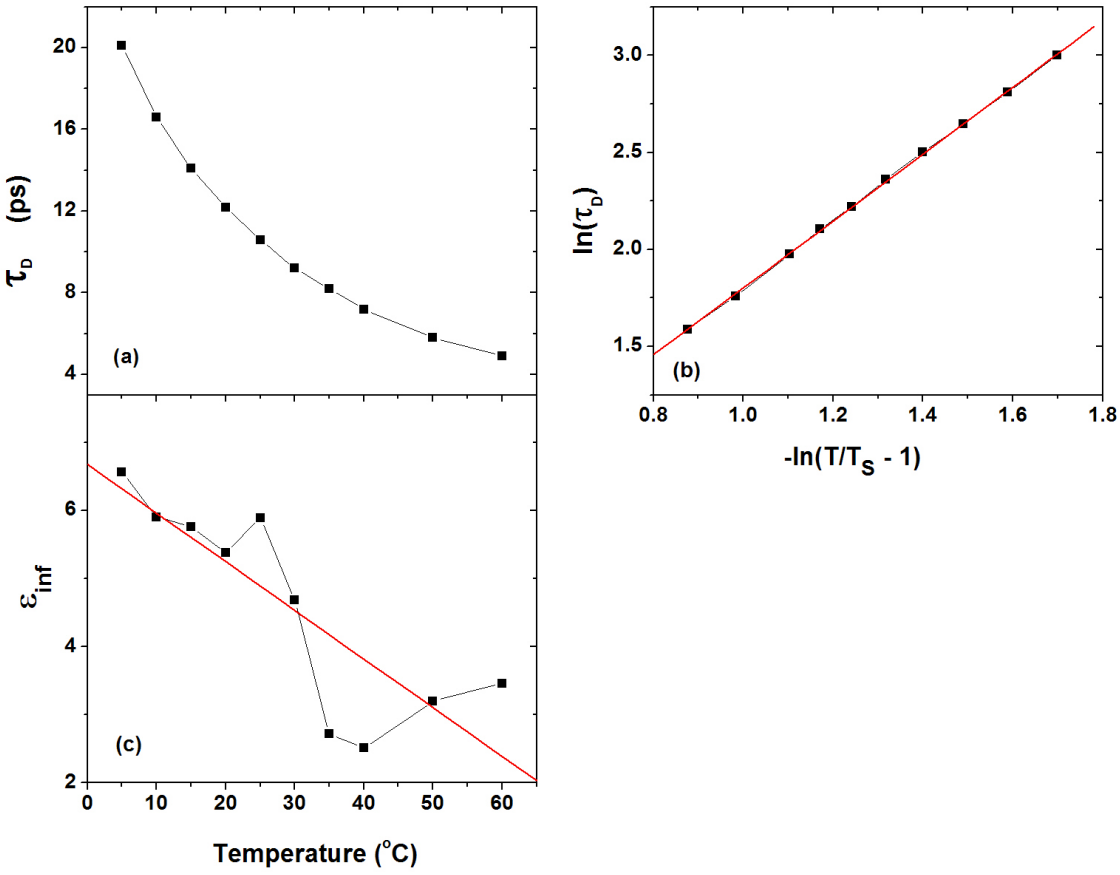

Figure C.1 (a) Yastremskii relaxation times. (b) ε_∞ versus temperature with linear fit shown in equation C.4. (c) Angell plot of Yastremskii's relaxation times. Result of linear fit is shown in equation C.1.

In order to generate data from 0.8 GHz to 14.4 GHz, we model Yastremskii's permittivity data as a single Debye of the form

$$\hat{\varepsilon}(\omega) = \varepsilon_\infty + \frac{\varepsilon_0 - \varepsilon_\infty}{1 + i\omega\tau_D} \qquad \text{(C.2).}$$

with the static dielectric constant ε_0 given by

$$78.25[1 - 4.617\times10^{-3}(T-25) + 1.22\times10^{-5}(T-25)^2 - 2.7\times10^{-8}(T-25)^3] \qquad \text{(C.3)}$$

Here, the temperature T is given in Celsius [16]. Using his measurements of the complex permittivity and relaxation time, the ε_∞ values are obtained and plotted as a function of his measured temperatures, and is shown in figure C.2(c). A linear fit of this graph provides the temperature dependence used for interpolation of ε_∞, and is

$$\varepsilon_\infty(T) = 6.68 - (0.07145)T \qquad \text{(C.4)}$$

where T is in units of Celsius.

C.2 Interpolation of Far IR Data

The high frequency response of D_2O was set using data by H. R. Zelsmann [42]. Zelsmann measured the complex index of refraction for heavy water between 0.586 THz to 18.03 THz at five temperatures: 4.0, 20.2, 38.7, 57.2, and 81.2 ^oC. The n and k measurements of 4.0 ^oC and 20.2 ^oC were converted to $\hat{\varepsilon}(\omega)$, and the reduced polarization was fit using 1 Debye relaxation and four Lorentzians.

$$\frac{(\hat{\varepsilon}(\omega) - \varepsilon_\infty)(2\hat{\varepsilon}(\omega) - \varepsilon_\infty)\varepsilon_0}{(\varepsilon_0 - \varepsilon_\infty)(2\varepsilon_0 - \varepsilon_\infty)\hat{\varepsilon}(\omega)} = \frac{a_1}{1 + i\omega\tau_1} + \sum_{i=1}^{4} \frac{\omega_i^2 b_i}{\omega_i^2 - \omega^2 + i\omega\Gamma_i} \qquad \text{(C.5)}$$

The features of the permittivity spectra at temperatures above 20.2 ^oC were too broadened to be fit satisfactorily. The fit parameters were then linearly interpolated as a function of temperature and applied to the current D_2O measurements between 4.3 and 20.0 ^oC.

Temperature (^oC)	ε_0	ε_∞	a_1	τ_1 (ps)	b_1	ν_1 (THz)	Γ_1 (ps^{-1})	b_2
4.0 ^oC D_2O	86.277	1.907	0.9576	13.462	0.0118	1.0021	11.638	0.0195
20.0 ^oC D_2O	80.081	1.894	0.9316	16.005	0.0341	1.1148	21.285	0.0207
	ν_2 (THz)	Γ_2 (ps^{-1})	b_3	ν_3 (THz)	Γ_3 (ps^{-1})	b_4	ν_4 (THz)	Γ_4 (ps^{-1})
4.0 ^oC D_2O	5.356	34.949	0.0074	13.494	58.716	0.0037	16.0892	36.632
20.0 ^oC D_2O	5.331	35.986	0.0099	12.986	60.508	0.0036	15.977	36.332

Table C.1 Fit parameters for Zelsmann's D_2O FIR data at 4.0 ^oC and 20.2 ^oC for.

The fit parameters for the two D_2O temperatures are given in table C.1. Figure C.2 displays Zelsmann's D_2O data along with the two fits for 4.0 ^oC and 20.2 ^oC. The interpolated D_2O spectra for the temperatures of 4.3, 7.7, 11.2, and 20.0 ^oC are shown in figure C.3.

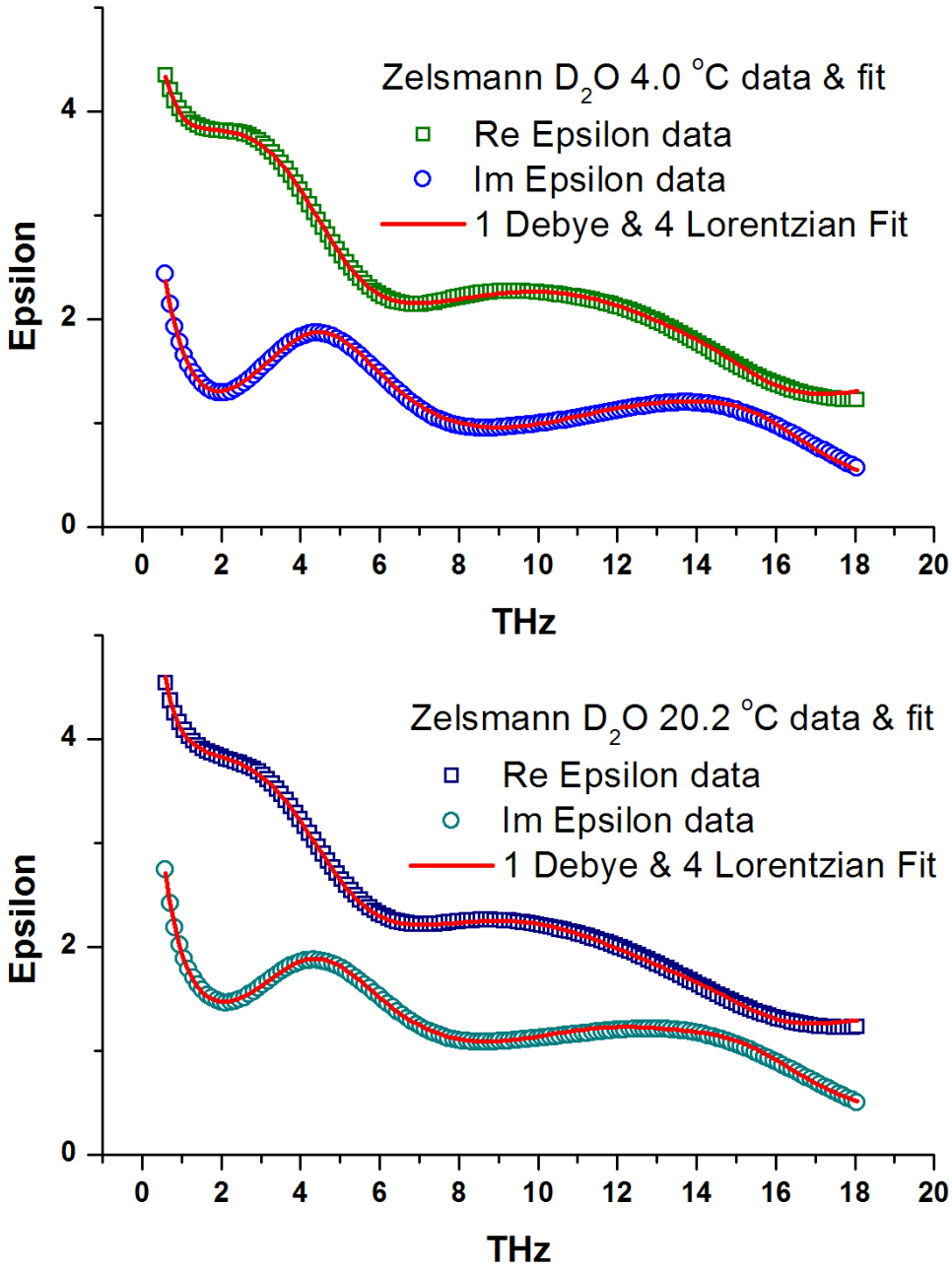

Figure C.2 Zelsmann's D_2O data and with a single Debye plus 4 Lorentzians fit for 4.0 °C and 20.2 °C. The real data is represented by squares and is the upper curve, while the imaginary data is shown by circles and is the lower curve.

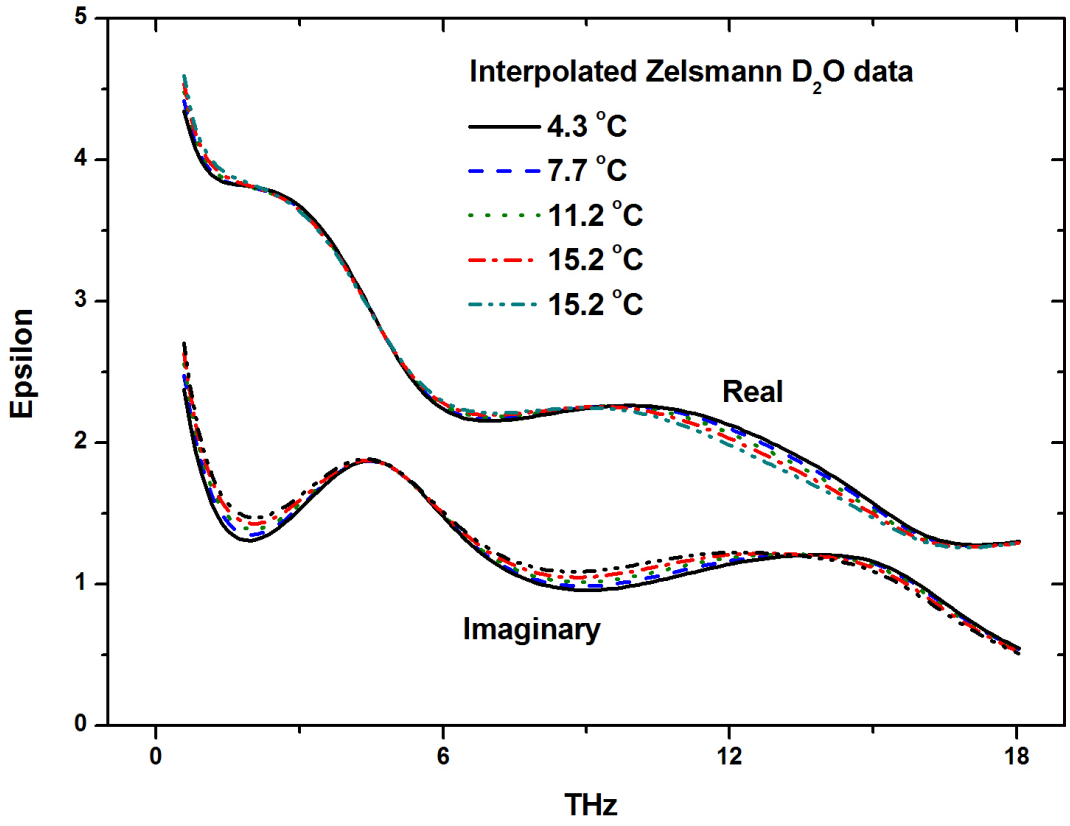

Figure C.3 Interpolated high frequency heavy water spectra at five temperatures using linear interpolation from fit values given in table C.1.

C.3 Data Stitching and Subtraction of Background

Once the interpolation has been completed for both Yastremskii's microwave data and Zelsmann's FIR data, both sets are stitched on the ends of the current D_2O spectra. This generates a large set of data that enables us to fit to the known 2 Debye relaxations and 4 Lorentzian oscillators. This is illustrated in figure C.4, where the black triangles represent the data points of the current measurement for D_2O at 7.7 ^oC. The residual from this fit is shown to exhibit oscillatory motion and is fit to 6 new Lorentzians, as discussed and shown in section 5.2.4.

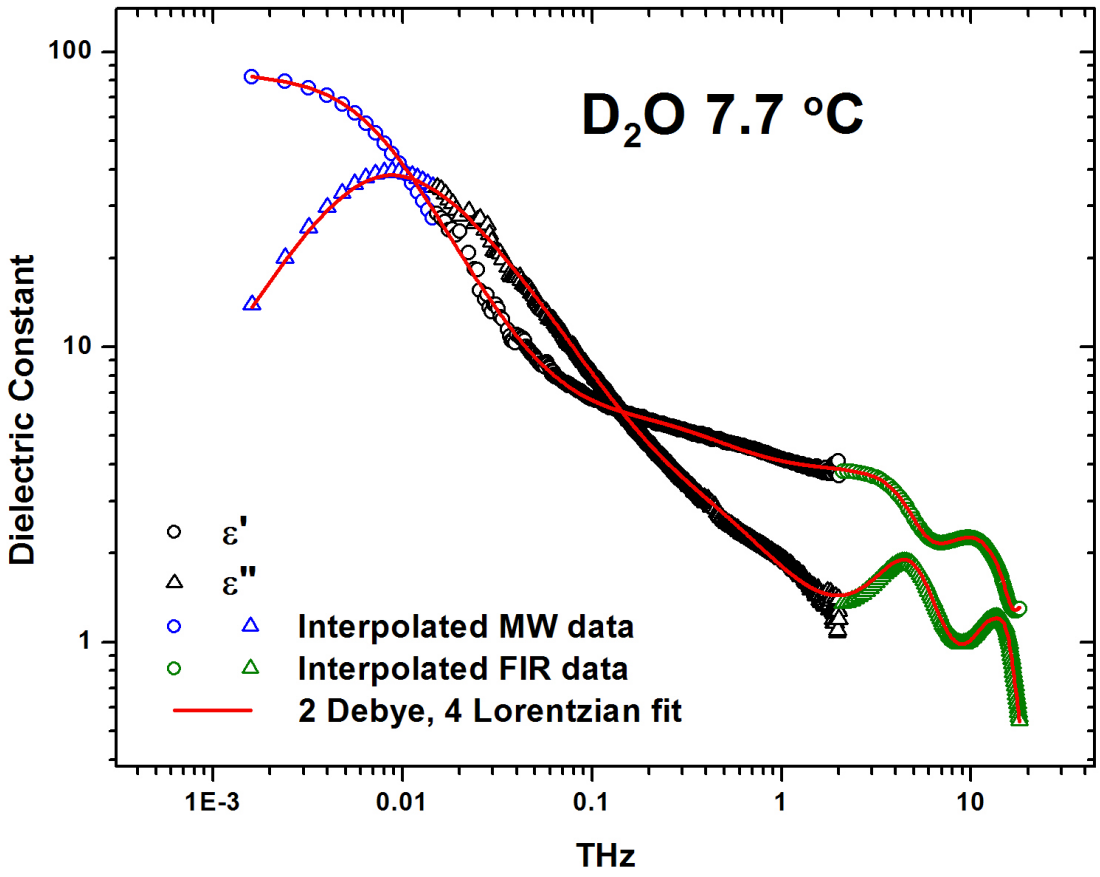

Figure C.4 Yastremskii's interpolated microwave data and Zelsmann's interpolated FIR data stitched to the current measurement for D_2O at 7.7 ^oC. The fit contains all the known spectral features in D_2O.

Appendix D

Calculation of Variance in Fit Parameters.

The method of Least-Squares is a widely used curve fitting technique involving the minimization of the function χ^2, where

$$\chi^2 = \sum_i \left[\frac{1}{\sigma_i^2} \left(y_i - y(x_i) \right)^2 \right] \tag{D.1}$$

Here σ_i is the error in the measurement y_i and the function $y(x_i)$ can be a sum of linear and nonlinear functions with one or more fit parameters [88].

If we wish to fit the data to a function defined as

$$y_i(x_i) = \sum_j^n f_j \left(\theta_k, x_i \right) \tag{D.2}$$

with θ_k as the fit parameters of the function f_j, then the χ^2 minimization is achieved by taking the first derivatives of χ^2 with respect to θ_k and solving the set of coupled equations. Additionally, the variances of the parameters θ_k are obtained by taking the derivative

$$\sigma_{\theta_k}^2 = \sum \left[\sigma_i^2 \left(\frac{\partial \theta_k}{\partial y_i} \right)^2 \right]. \tag{D.3}$$

For this experiment, the reduced polarization is fit to a sum of two Debye relaxations and ten Lorentzians:

$$\frac{(\hat{\varepsilon}(\omega)-\varepsilon_\infty)(2\hat{\varepsilon}(\omega)-\varepsilon_\infty)\varepsilon_0}{(\varepsilon_0-\varepsilon_\infty)(2\varepsilon_0-\varepsilon_\infty)\hat{\varepsilon}(\omega)} = \sum_{i=1}^{2}\frac{a_i}{1+i\omega\tau_i} + \sum_{j=1}^{10}\frac{b_j{\omega_j}^2}{{\omega_j}^2-\omega^2+i\omega\Gamma_j} \tag{D.4}$$

where the fit parameters are ε_0, a_i, b_j, τ_i, ω_j, and Γ_j. This gives two parameters for each Debye relaxation and three parameters for each Lorentzian.

For fitting dielectric spectra to one or two Debye or Cole-type relaxations, equation D.3 has been demonstrated to be an acceptable method for calculating the variances in the parameters. Due to complexities in numerically minimizing a complex function, these functions have typically been split into separate real and imaginary functions, and then fit as a sum of two real functions [59].

While this method is reasonable for a small amount of free parameters, it can easily become cumbersome for large and complicated functions, such as equation D.4. Furthermore, despite the many minimization techniques that are available to obtain values for the fit parameters, the equations for individual θ_k's may not be exactly solvable in order to obtain their variance.

For a sufficiently large sample, an alternative approach is to approximate χ^2 as a quadratic function of θ_k near the local minimum of that parameter. The uncertainty in the parameter can then be determined from the curvature of the χ^2 function and is given by

$$\sigma_{\theta_k}^2 = 2\left(\frac{\partial^2\chi^2}{\partial\theta_k^2}\right)^{-1} \tag{D.5}$$

The caveat here is that this expression does not account for any covariance between fit parameters, and is better suited for uncorrelated parameters [88]. Due to this, the reported error may be lower than the actual error.